
Contact Dynamics from the Atomic Scale to Nanostructured Surfaces

Inauguraldissertation

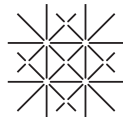
zur

Erlangung der Würde eines Doktors der Philosophie
vorgelegt der
Philosophisch-Naturwissenschaftlichen Fakultät
der Universität Basel

von

Sabine Maier

von Basel, Schweiz



UNI
BASEL

Basel, 2006

Genehmigt von der Philosophisch-Naturwissenschaftlichen Fakultät auf Antrag von:

Prof. E. Meyer

Prof. R. Bennewitz

Basel, den 19. Dezember 2006

Prof. Dr. Hans-Peter Hauri
Dekan

Table of Contents

List of Figures	iii
List of Abbreviations	v
Abstract	1
Chapter 1: Introduction to Scanning Probe Microscopy	3
1.1 Scanning Probe Microscopy	3
1.2 Friction Force Microscopy	5
1.2.1 Atomic-Scale Stick-Slip and the Tomlinson Model	6
1.2.2 Velocity Dependence	10
1.2.3 Superlubricity	10
1.3 Non-Contact Atomic Force Microscopy	11
1.3.1 Relevant Forces	12
1.3.2 Dissipation Induced by Tip-Sample Interactions	13
Chapter 2: Experimental Setup in Ultrahigh Vacuum	15
2.1 Ultrahigh Vacuum System	15
2.2 The Atomic Force Microscope	16
2.3 Calibration of Forces and Amplitudes	19
2.4 Properties and Preparation of the Cantilevers	22
2.5 Sample Preparation	23
Chapter 3: The Influence of the Tip-Sample Contact on Thermal Fluctuations of a Cantilever	27
3.1 Introduction	27
3.2 Frequency Spectrum of Thermal Fluctuations: From Non-Contact to Contact	28
3.3 Load Dependence of the Resonance	31
3.4 Calculation of the Torsional Resonance Frequency of the Cantilever in Contact	36
3.4.1 Point-Mass Model	36
3.4.2 Beam Equation	37
3.4.3 Comparison between the Two Models	38
3.5 Calculation of the Quality Factor in Contact	40
3.6 Conclusions	41

Chapter 4:	Time Resolved Atomic-Scale Stick-Slip Measurements	43
4.1	Introduction	43
4.2	Atomic-Scale Stick-Slip on KBr(100)	43
4.3	Determination of Slip Duration	45
4.4	Stick-slip Simulations with a Two-Spring Tomlinson Model	49
4.5	Local Correlation Function of the Lateral Force	54
4.6	Conclusions	57
Chapter 5:	Control of Atomic Friction by Actuation of the Contact	59
5.1	Introduction	59
5.2	Experiments on NaCl(100)	59
5.3	Dynamic Extension of the Tomlinson Model	62
5.3.1	Estimation of the Residual Friction	65
5.3.2	Estimation of the Energy Loss	71
5.3.3	Thermal Effects	72
5.4	Conclusions	75
Chapter 6:	Ultrathin Alkali Halide Films: Heteroepitaxial Growth and Atomic-Scale Friction	77
6.1	Introduction	77
6.2	Heteroepitaxial Growth of KBr/NaCl(100) and NaCl/KBr(100)	78
6.2.1	Heteroepitaxial Growth of KBr on NaCl(100)	78
6.2.2	Heteroepitaxial Growth of NaCl on KBr(100)	84
6.2.3	Discussion about the Different Growth Modes	86
6.3	Contact Atomic Force Microscopy at the Resolution Limit	88
6.4	Atomic-Scale Stick-Slip on Top of KBr Films Grown on NaCl	90
6.5	Conclusions	98
Conclusions and Outlook		101
Acknowledgments		103
Bibliography		105
List of Publications		117
	Papers	117
	Talks	118
	Posters	118
Curriculum Vitae		119

List of Figures

1.1	Basic principle of a scanning probe microscope	4
1.2	Beam deflection method for the detection of the cantilever deflection	4
1.3	Operation modes of an AFM illustrated with a force-distance curve	4
1.4	Stick-slip in the framework of the Tomlinson model	7
1.5	Energy landscape in the Tomlinson model	8
1.6	Friction loop on KBr(100)	10
2.1	Pictures of the UHV-systems	15
2.2	Picture of the home-built UHV-AFM	17
2.3	Controlling scheme for non-contact and contact AFM	18
2.4	Calibration of forces and amplitudes based on force-distance curves	20
2.5	Determination of the Q-factor performing a frequency sweep	21
2.6	Determination of the Q-factor from thermal noise measurements	21
2.7	SEM images of silicon cantilevers	23
2.8	AFM images of a prepared KBr(100), Cu(100) and Al ₂ O ₃ (0001) surface	24
3.1	Power spectral density plot of thermal fluctuations in the normal and lateral force signal of a free contact cantilever	29
3.2	Ring-down experiment for an externally excited oscillation in contact	31
3.3	Frequency spectrum of fluctuations on Al ₂ O ₃ (0001)	33
3.4	Contact stiffness versus load of a spherical tip in contact with Al ₂ O ₃ (0001)	34
3.5	Spherical tip in contact with a Cu(100) surface	35
3.6	Scheme of the presented models for the torsional resonance frequency of the cantilever in contact	36
3.7	Calculated frequency shift for the spherical tip upon contact formation	39
4.1	Atomic-scale stick-slip on KBr(100)	44
4.2	Lateral force signal showing stick-slip acquired with different temporal resolutions on KBr	46
4.3	Slips recorded with high temporal resolution	47
4.4	Distribution of the slip durations	48
4.5	Three spring configurations for different implementation of the Tomlinson model	50
4.6	Simulation of the stick-slip process in commensurate contact	52
4.7	Simulation of the stick-slip process in incommensurate contact	53

4.8	Autocorrelation of a damped oscillator and white noise	54
4.9	Calculation of a local correlation function from the lateral force	55
4.10	Local correlation of the lateral force signal	56
5.1	Reduction of friction by actuation of nanometer-sized contacts on NaCl(100)	60
5.2	Reduction of friction by actuation of nanometer-sized contacts on NaCl: power spectra and frequency sweep	61
5.3	Lateral force simulated with a dynamic Tomlinson model	64
5.4	Evolution of the tip position in the oscillating potential energy landscape	65
5.5	Spatio-temporal mismatch	66
5.6	Phase dependence of the lateral force	67
5.7	Extra oscillations leading to the residual friction	68
5.8	Velocity dependence of the residual friction force	70
5.9	Residual friction force versus v/fa	70
5.10	Energy loss per lattice spacing with and without actuation	71
5.11	Energy loss due to actuation in a underdamped and overdamped system	73
5.12	Effects of thermal activation on friction simulations with actuation.	74
5.13	Phase dependence including thermal effects	74
6.1	Submonolayer growth of NaCl on KBr(100)	79
6.2	Topography, Δf and damping of KBr islands grown on NaCl(100)	80
6.3	Detail images of the superstructure on the KBr islands grown on NaCl(100)	81
6.4	Growth of several layers of KBr on NaCl(100)	82
6.5	KBr films grown at elevated temperatures	83
6.6	Submonolayer growth of NaCl on atomically flat KBr(100)	84
6.7	Details of NaCl islands grown on KBr(100)	85
6.8	Submonolayer growth of NaCl on KBr(100) at elevated temperatures	86
6.9	Atomic resolution image showing an NaCl island and the KBr(100) substrate	87
6.10	Three monolayers of NaCl evaporated on KBr(100)	87
6.11	Contact AFM measurements on KBr films on NaCl(100)	89
6.12	Atomic-scale stick-slip on the ultrathin KBr films on NaCl(100)	91
6.13	Energy corrugation and spring constant along a unit cell of the KBr/NaCl superstructure	94
6.14	Tomlinson model with a spatially modulated energy corrugation	96
6.15	Atomic-scale friction on flat NaCl films on KBr(100)	97

List of Abbreviations

A_{exc}	excitation amplitude
AC	alternating current
AES	auger electron spectroscopy
AFM	atomic force microscope
a.u.	arbitrary unit
Cu	copper
DC	direct current
Eq.	equation
FFM	friction force microscope
FFT	Fast Fourier Transformation
Fig.	figure
HOPG	highly ordered pyrolytic graphite
KBr	potassium bromide
LEED	low-energy electron diffraction
MEMS	micro-electro-mechanical system
NaCl	sodium chloride
nc-AFM	non-contact atomic force microscope
NEMS	nano-electro-mechanical system
PLL	phase locked loop
PSD	power spectral density
RHEED	reflection high-energy electron diffraction
RMS	root mean square
SEM	scanning electron microscope
SPM	scanning probe microscopy
STM	scanning tunneling microscope
UHV	ultrahigh vacuum
XPS	X-Ray photoelectron spectroscopy

Abstract

The collective mechanical behavior of a multitude of small contacts affects the friction between sliding bodies on the macroscopic scale. The contacts are complicated systems involving many atoms, which are constantly deformed, ruptured and reformed. In atomic force microscopy the situation is simplified by studying a single asperity contact between a sharp tip and atomically flat surfaces on the microscopic scale. In this thesis several aspects of contact dynamics have been analyzed using atomic force microscopy in ultrahigh vacuum.

First, the influence of the tip-sample contact on the thermal fluctuations of the force sensor and on the dynamics of the stick-slip process were characterized. A power spectrum analysis showed that the fluctuations are strongly damped through the tip-sample contact. The frequency shift of the resonance in contact was used as a measure of the contact stiffness. Depending on the contact size different dependencies on the load were observed. Atomic-scale stick-slip measurements studying the jump dynamics with high spatial and temporal resolution suggested a wide variation of slip durations up to several milliseconds. These results are compared with a multiple-tip simulation based on a Tomlinson model including thermal activation. Thus, a correlation between the duration of atomic slip events and the atomic structure of the contact is established.

Second, the actuation of nanometer-size contacts was studied by simulations based on an extended Tomlinson model. In this way the control and reduction of friction to negligible values was described. Such simulations allowed us to approximate the residual friction forces and compare them to an analytical approximation. Moreover, not only a reduction of friction but also a reduction in energy loss was found in sufficiently underdamped systems.

Third, the influence of nanostructured surfaces on atomic friction has been studied. For this purpose, ultrathin epitaxial films of KBr on NaCl(100) and NaCl on KBr(100) have been grown. The structure of such films was studied by high resolution non-contact atomic force microscopy. In the case of sub-monolayer coverage of KBr on NaCl(100), a superstructure was found on islands of two and three layer height caused by the lattice mismatch. The friction on such a structure changes from atomic-scale stick-slip to smooth sliding within a unit cell of the superstructure because of a variation of the energy corrugation. Moreover, scans across atomic scale defects confirm the high resolution capabilities of friction force microscopy close to the ultralow friction state. In the complementary system, NaCl on KBr(100), flat islands without any superstructure or rumpling were observed. Atomically resolved non-contact images of the sub-monolayer coverage prove that the lattice constant of the NaCl islands is elongated to match the one of KBr(100).

In summary, several different aspects of friction and contact dynamics from the atomic scale to nanostructured surfaces were discussed and explained.

Introduction to Scanning Probe Microscopy

1.1. Scanning Probe Microscopy

The field of scanning probe microscopy (SPM) started in 1982 with the invention of the scanning tunneling microscope (STM) by G. Binnig and H. Rohrer [1]. By applying a bias voltage between a sharp tip and a sample, a tunneling current flows from the foremost atoms of the tip through the vacuum gap into the surface. Because the tunneling current decays exponentially with the distance between tip and surface, it is possible to image surfaces on the atomic scale by scanning over a sample and keeping the tunneling current constant. The inventors were awarded the Nobel prize in physics in 1986. The first and most important extension of the STM was the atomic force microscope (AFM), invented in 1986 by Binnig, Quate and Gerber [2]. With an AFM, one measures interaction forces down to the piconewton range. A microfabricated cantilever with a sharp tip at its end serves as a force sensor. Normal and lateral forces on the tip are measured as bending and twisting of the cantilever. In contrast to the STM, the atomic force microscope is not restricted to electrically conductive surfaces. The family of scanning force microscopy has several other members, based on measurements of other quantities, i.e. electric and magnetic properties of surfaces, friction forces, and chemical potentials. In addition to imaging surfaces STM and AFM give the opportunity to manipulate atoms and molecules in a controlled way and perform various types of spectroscopy. With the invention of these new types of microscopes the doors to study all kinds of phenomena on the nanometer scale have been opened, and tremendous progress has been achieved in nanoscience.

The basic principle that all scanning probe microscopes have in common is a sharp probe, which scans a sample along a raster as illustrated in Fig. 1.1. The interaction signals like tunneling current or forces between the probe and the sample are recorded for every point of the raster. Often, one of the interaction signals is used as feedback in order to keep the distance between probe and surface of the sample constant. If the interaction between the probe and the surface has a near-field component, imaging well beyond the resolution limit of far-field techniques like optical microscopy or scanning electron microscopy becomes possible. As the resolution is no longer restrained by the wavelength of light or electrons, the resolution obtainable by STM and AFM reaches down to single atoms and molecules and is in principle only limited by the geometrical shape of the probe. However, it is important to note that the measured surface topography of a homogeneous surface in SPM is a good approximation to the real topography. But in STM, what we call topography is actually a map of constant density of states. In force microscopy, the situation is even more complicated as the image results from an interplay of different forces.

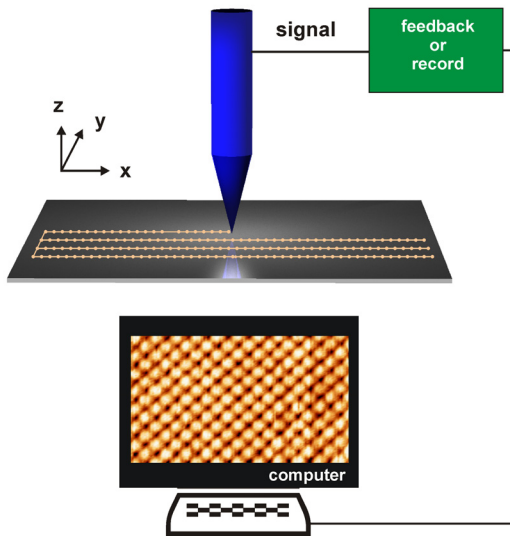


Figure 1.1: Basic principle of a scanning probe microscope: A sharp probe scans over a surface and the interaction signals (i.e. tunneling current) between probe and surface are recorded, which provides surface maps in real space.

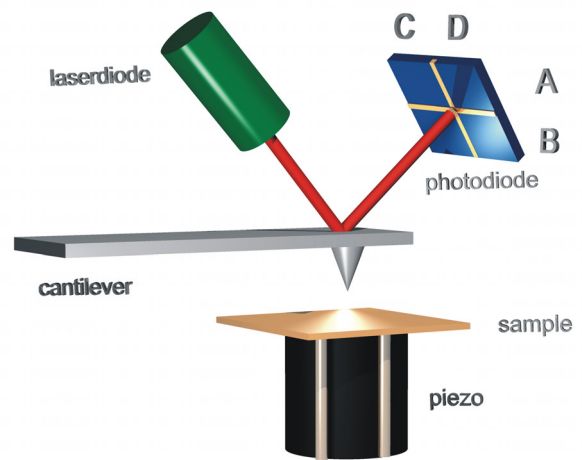


Figure 1.2: Principle of the beam deflection method: The bending and twisting of the cantilever are measured by means of the deflection of a light beam from the back side of the cantilever, which is subsequently recorded on a position sensitive four-quadrant photodiode.

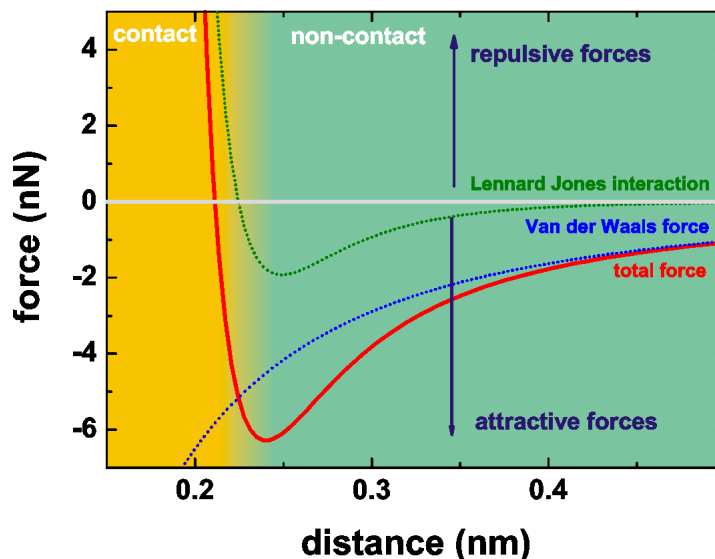


Figure 1.3: Force vs. distance curve including the long range van der Waals interaction and the short-range Lennard-Jones-like interaction. Non-contact AFM is done such that the tip-sample interaction is in the attractive regime, while contact AFM is performed by bringing the tip to a distance at which repulsive forces dominate the tip-sample interaction. (Parameters used to plot the force-distance curves according to the equations in section 1.3.1: $E_{bond}=1\text{eV}$, $\sigma = 0.2\text{nm}$, $R=1\text{nm}$ and $H_A=260\cdot 10^{-21}\text{J}$)

Since the scanning probe needs to be positioned with an accuracy of a few picometers if atomic resolution is to be achieved, the movement of the probe along the raster is often realized by means of piezoelectric translators. Piezoelectric materials like lead zirconium titanate change their shape in an electric field due their anisotropic crystal structure. In scanning force microscopy, typically, a sharp tip integrated in a micro machined cantilever serves as a force sensor. Alternatively, tuning forks with attached tips are used as force sensors. There are different techniques to detect the bending of the cantilever due to the tip sample forces. Often the optical beam deflection is used, which is illustrated in Fig. 1.2. The bending and twisting of the cantilever are usually measured by means of the deflection of a light beam from the back side of the cantilever and subsequently recorded on a position sensitive four-quadrant photodiode [3]. This detection scheme allows to measure normal and lateral forces on the cantilever simultaneously. Other methods to detect the bending of the cantilever include interferometry [4] or the use of piezo resistive cantilevers [5].

An ultrahigh vacuum (UHV) environment is required to study surfaces on the atomic level in order to keep the surface free from contaminants. In UHV, an atomic force microscope can be operated in dynamic or static, non-contact or contact mode. In dynamic non-contact measurements, the cantilever is excited at its resonance frequency. The tip is approached to the surface so that attractive forces dominate the tip-sample interactions. In contact AFM the tip is brought into repulsive contact with the sample. Friction forces can be analyzed by recording the lateral deflection of the cantilever simultaneously. Fig. 1.3 illustrates the different operating regimes on the basis of a force-distance curve. The next two sections will present further details of friction force microscopy and dynamic non-contact atomic force microscopy as well as summarize recent developments in the field.

1.2. Friction Force Microscopy

Friction is a very old phenomenon, which occurs everywhere in daily life. For example without friction between our feet and the ground we would simply not be able to walk. In this case friction is desired. On the other hand, friction and wear are the main causes of power loss, which is a problem in machinery. Therefore a lot of research has been done on the reduction of friction on the macroscopic scale. In the last years, it became possible to build smaller and smaller electro-mechanical devices on the micrometer scale (MEMS) as well as nanometer scale (NEMS). The surface-to-volume ratio becomes larger on that scale and thus surface forces such as friction forces increase and play a decisive role in such devices. Therefore, it is important to study friction and its reduction down to the atomic scale.

Leonardo Da Vinci (1452-1519) was one of the first persons to study friction systematically. He found that the size of the contact area between two macroscopic bodies has no effect on their friction and that the frictional force between two sliding surfaces is proportional to the applied load. Unfortunately, Da Vinci's manuscripts were hidden and lost for centuries. Guillaume Amontons (1663-1705) rediscovered the two basic laws of friction 150 years later. Leonard Euler (1707-1783) was the first to distinguish between static and kinetic friction: He observed that static friction is always larger than kinetic friction. The third friction law proposed by Charles-Augustin Coulomb (1736-1806) states that kinetic friction is independent of the sliding velocities. In 1950, F. Philip Bowden and David Tabor gave a physical explanation for these three laws of friction. They found out that the true area of contact is a very small percentage

of the apparent contact area (typically a factor 10^{-5}), formed by several asperities. As the normal force increases, more of these asperities come into contact and the average contact area of each asperity grows. Bowden and Tabor argued that within these asperities all the dynamics of friction takes place. In 1987, Mate et al. demonstrated the first observation of friction on the atomic scale using a friction force microscope (FFM) [6]. Friction force microscopy allows to study the tribological behavior of a single asperity contact between a sharp tip and an atomically flat surface. The force sensor in FFM is a microfabricated soft silicon cantilever with an integrated sharp tip at its end. The tip is brought into repulsive contact with the sample surface and the applied load on the contact is measured as normal bending of the cantilever. When the sample starts sliding with respect to the tip, the lateral force acting on the tip causes a twist of the cantilever. Hence, friction forces can be determined from the twisting of the cantilever. Bending and twisting are usually measured by means of the deflection of a light beam reflected from the back side of the cantilever.

1.2.1 Atomic-Scale Stick-Slip and the Tomlinson Model

One prominent experimental observation in friction studies is the so-called stick-slip movement. Stick-slip movement on the macroscopic scale is familiar from everyday life: A creaking door hinge, the excitation of a violin string, screeching tires, the squeaking of chalk on a blackboard and earthquakes. In friction force microscopy, atomic-scale stick-slip instabilities occur when the tip sticks to a certain equilibrium position at the surface until the increasing lateral force initiates a slip towards another equilibrium position. On crystalline surfaces, this process repeats itself periodically every lattice spacing.

Atomic-scale stick-slip has been experimentally observed on a variety of materials including insulators, metals and semiconductors. The first observation of atomic stick-slip by Mate et al. was reported on graphite [6]. Stick-slip was also observed on other layered materials like mica [7], MoS₂ [8] and NbSe₂ [9]. In scanning probe microscopy experiments on graphite, it is known that thin, flat flakes of graphite are frequently transferred to the probing tip thus providing a multi-atom contact. Ionic crystals are very common in atomic-scale friction studies, because of their simple structure and comparatively simple preparation. Normally, the periodicity of the stick-slip on ionic crystals corresponds to the unit-cell as found on KBr [10], NaCl [11, 12] and KF [13]. Measurements on NaF(100) by Ishikawa et al. are the exception since they could resolve both components depending on the applied load [14]. Atomic stick-slip was also observed on metals: The formation of a neck of copper atoms at the tip allows stick-slip type sliding over Cu(111) surfaces [15]. In contrast to the Cu(100) surface, which is worn, because it is not a crystallographic glide plane [11, 16]. By using passivated tips, atomic stick-slip was recently observed on Pt(111) [17]. Passivated tips allowed also to investigate the Si(111)(7x7) [18] reconstruction.

The atomic-scale stick-slip process is often understood using a simple mechanical model referred to as the Tomlinson model [19]. In this model a mass attached by a spring to a constantly moving support is pulled along a periodic surface potential with amplitude E_0 . The total potential is therefore given as a sum of the periodic surface potential and the elastic energy which is stored in the spring:

$$V = -\frac{E_0}{2} \cos\left(2\pi \frac{x_{tip}}{a}\right) + \frac{1}{2}k(x_{tip} - x)^2, \quad (1.1)$$

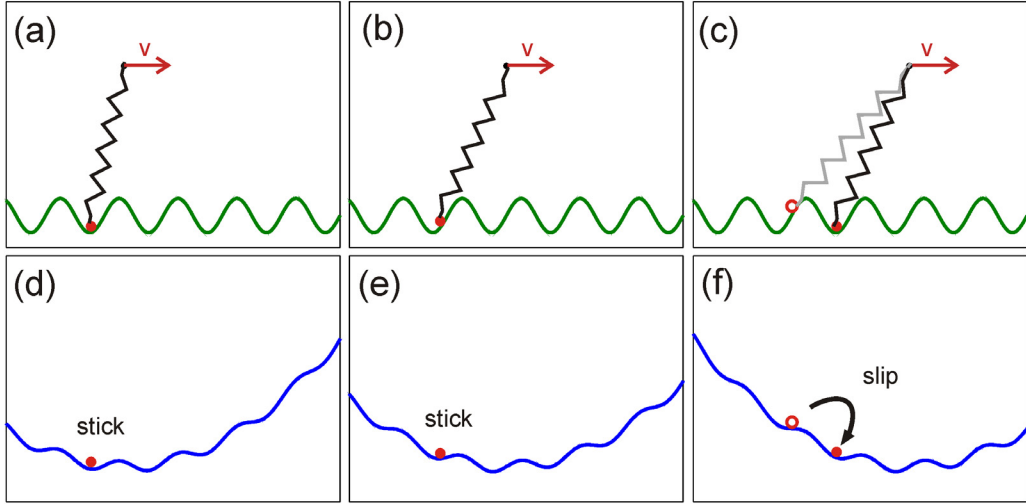


Figure 1.4: Scheme which explains the stick-slip movement in the framework of the Tomlinson model in (a)-(c) position space and (d)-(f) in the energy space. The tip represented by the red dot is stuck in one of the local minima of the total potential until the growing lateral force is strong enough to initiate a jump into the next stable position (c). This behavior is referred to as atomic-scale stick-slip. The blue curve in (d)-(f) shows the total potential of the spring and the surface corrugation (Eq. 1.1) for the different support positions in (a)-(c).

where $x = vt$ is the position of the support and a the lattice constant of the surface. The effective spring constant of the pulling spring k does not only represent the spring constant of the force sensor but also the respective compliance of tip and surface. The stiffness of tip and surface are usually summarized under the term 'contact stiffness'. Fig. 1.4 illustrates the stick-slip behavior in the framework of the Tomlinson model in the position space (a)-(c) and energy space (d)-(f) for different positions of the support. The tip is stuck in one of the local minima of the total potential (d)-(e) until the growing lateral force is strong enough to initiate a jump into the next stable position (f). The lateral force is increasing because the support of the tip is moving and extends the spring. A stable local equilibrium position means mathematically that the derivative of the potential V with respect to the position of the tip x_{tip} equals zero and that the second derivative is positive:

$$\frac{\partial V}{\partial x_{tip}} = \frac{E_0\pi}{a} \sin\left(2\pi\frac{x_{tip}}{a}\right) + k(x_{tip} - x) = 0 \quad (1.2)$$

$$\frac{\partial^2 V}{\partial x_{tip}^2} > 0 \quad \Leftrightarrow \quad \cos\left(\frac{2\pi x_{tip}}{a}\right) > -\frac{ka^2}{2E_0\pi^2} = -\frac{1}{\eta}. \quad (1.3)$$

In Fig. 1.5(a) the sinusoidal surface potential term and the spring term of Eq. (1.2) are plotted with the corresponding total potential (b). One observes that for some values of k several possible solutions exist, leading to instable regions for the tip. This causes hysteresis loops between forward and backward scan. The parameter $\eta = \frac{2\pi^2 E_0}{ka^2}$ in the second restriction (Eq. (1.3)) expresses the relation between the corrugation amplitude E_0 and the elastic energy $\frac{1}{2}ka^2$ stored in the spring [20]: If $\eta < 1$ Eq. (1.3) is always fulfilled, this means the tip is always sitting in a local minimum and its movement is therefore continuous. In the case of $\eta > 1$,

Eq. (1.3) is not always true, hence periodically instabilities occur and stick-slip behavior is found. In an overdamped system, the tip jumps from one equilibrium position to the next but recently it has been shown that in an underdamped condition also multiple slips are possible [21, 22].

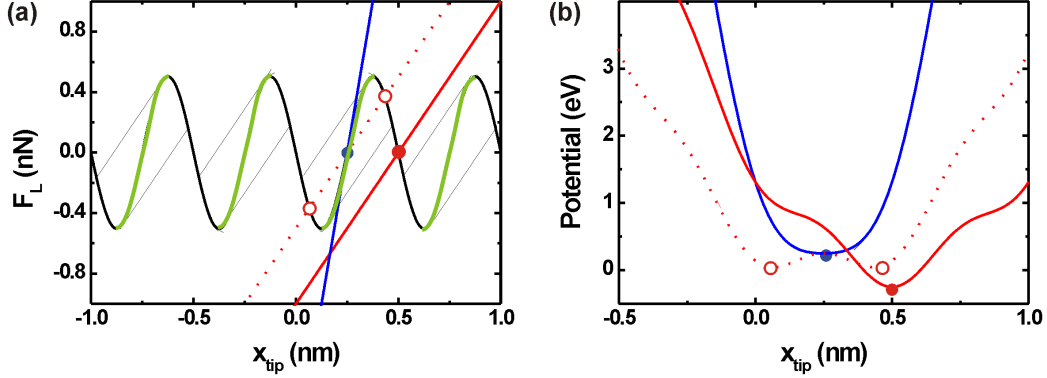


Figure 1.5: (a) Graphical solution of Eq. (1.2) to illustrate the instabilities. The straight lines show the force from the spring and the curved lines show the periodic surface potential. For $c = 8$ N/m and $\eta = 0.8$ there is a single intersection of the blue line with the surface potential for each value of x_{tip} , and thus a smooth sliding from one minimum to the next is possible. For $c = 2$ N/m and $\eta = 3.2$ illustrated by the red lines, there exist multiple intersections with the surface potential for several x_{tip} . Green portions of the potential curve indicate such unstable regions causing hysteresis loops between forward and backward scans. Due to the unstable regions stick-slip instabilities cannot be avoided. (b) The corresponding total potential energies according to Eq. (1.1) are plotted. In conclusion, this graph reveals that the stiff tip (blue) follows instantaneously the equilibrium position while for the soft tip stick-slip instabilities occur. The following additional parameters were used: $E_0 = 0.5$ eV and $a = 0.5$ nm,

If we replace the spring-term $F_L = k(x_{tip} - x)$ in Eq. (1.2), it follows that

$$F_L = -\frac{\pi E_0}{a} \sin\left(2\pi \frac{x_{tip}}{a}\right). \quad (1.4)$$

The maximum of the absolute value of the lateral force F_L^{max} is found at $x_{tip} = a/4$, and we obtain

$$E_0 = \frac{a F_L^{max}}{\pi}. \quad (1.5)$$

This equation describes a linear dependence of the surface potential amplitude E_0 on the maximum lateral force F_L^{max} . In chapter 6 measurements of E_0 on ultrathin heteroepitaxial films of KBr grown on NaCl will be shown. On top of these films a superstructure is found due to the lattice mismatch between these two materials. Variations of the energy corrugation were observed on these KBr-determined surfaces, which demonstrates that chemically homogeneous surfaces can have significant variations of their atomic-scale friction properties due to small structural inhomogeneities.

The Tomlinson model has also been extended into two dimensions. Fujisawa et al. [7, 8, 23, 24] analyzed the forces in and perpendicular to the scan-direction simultaneously on different materials as MoS₂ and NaF(100). They found that the frictional forces do not always point exactly

in the direction of scanning. They measured contributions in both directions depending on the alignment of the scan direction with the crystallographic direction of the surface, and observed that the tip jumps always to the nearest sticking point. Therefore, the tip sometimes moves along the surface in zig-zag walk (2D stick-slip) or straight (1D stick-slip). Hölscher et al. [25] performed dynamical calculations for the case of NaF(100), where they observed similar zig-zag walks and straight walks as in the experiments of Fujisawa.

Thermal activation has to be included in the Tomlinson model in order to describe stick-slip at room temperature. Thermal activation causes the tip to jump to the next equilibrium position earlier. Hence, the stick-slip jump and its height, which is related to the maximum lateral force, is of a statistical nature. Sang et al. [26] investigated theoretically these jump processes considering thermal activation and presented an analytical expression for the statistical tip jump probability at finite temperatures. This tip-jump statistic of the stick-slip was experimentally confirmed on graphite by Schirmeisen et al. [27].

Quantitative values from atomic-scale stick-slip measurements can be obtained by analyzing plots of single scan-lines in the forward and backward directions - so-called friction loops. From such friction loops (as shown in Fig. 1.6), information about the dissipated energy and stiffness among other properties can be deduced. For example the area between the forward and the backward direction in a friction loop has the dimension of work and is a measure of the energy dissipated in the sliding process. Information about the stiffness is taken from the slope of the lateral force in a friction loop. For large η the slope of the lateral force during the sticking phase corresponds to the effective spring constant, which considers the stiffness of the contact and the force sensor. For η approaching to one this relation needs to be corrected according to $k_{eff} = \frac{\eta+1}{\eta} k_{exp}$ [28]. The lateral stiffness of the force sensor is usually at least a factor 50 higher than the contact stiffness. Therefore the effective spring constant is clearly dominated by the contact. Socoliuc et al. found that the contact stiffness does not change for small contact sizes and low loads [20]. However, in a continuum mechanics approach we expect the lateral stiffness to increase with load proportional to the contact area [29]. Luan and Robbins recently discussed the breakdown of continuum mechanics at the nanometer scale and found by numerical calculations that its applicability depends on the atomic structure of the tip apex [30]. In chapter 3 a detailed study of the contact properties including the stiffness and the damping is presented based on the analysis of thermal fluctuation spectra. Tips with different apex radii are compared to elucidate the limits of the applicability of continuum mechanics.

The first two classical friction laws state that the friction force is directly proportional to the applied load (Amontons First Law) and that the friction force is independent of the apparent area of contact (Amontons Second Law). On the microscopic scale, these two laws are related since the friction of a single asperity contact is proportional to the contact area, and the contact area is a function of load. Numerous models describe the dependence of the contact area with load assuming different interaction forces [29, 31–34]. A non-linear dependence of the applied load is expected in single asperity FFM experiments. However, a linear behavior is predominantly found in systems with vanishing adhesion between tip and sample. Only in systems with strong adhesion is a non-linear dependence found. For atomic-scale friction, a transition from very low friction towards a linear increase with the load was found [20]. However, for some materials abrasive wear is observed already at very low loads, i.e. $F_N = 3$ nN for KBr [35]. Gnecco et al. found on KBr that the debris formed by the moved material due to wear is reorganized in regular terraces with the same periodicity and orientation as the unscratched surface [36]. The formation of ripples was observed after scanning the same frame

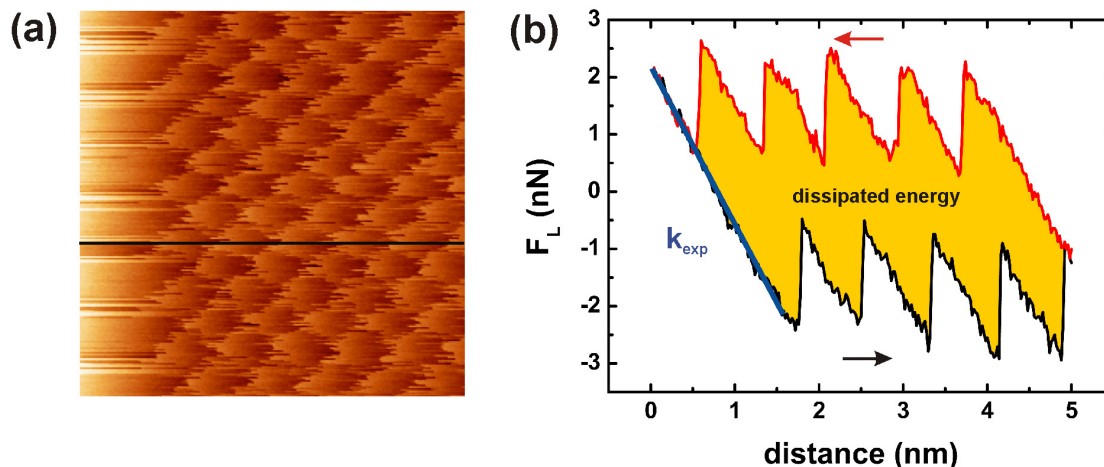


Figure 1.6: (a) Lateral force map recorded on an atomically flat KBr(100). The image has a size of $5 \text{ nm} \times 5 \text{ nm}$ and is recorded while scanning in forward direction. (b) Lateral force traces while scanning forwards and backwards over the KBr surface along the black line indicated in (a).

several times with a load above the wear threshold [37].

1.2.2 Velocity Dependence

The second macroscopic law of friction states that friction is independent of the sliding velocity. In atomic-scale friction experiments a logarithmic dependence of the mean friction force is found at low velocities [12]. The friction force increases with increasing scanning velocity. The physical origin of the velocity dependence can be understood within the Tomlinson model. The slower the tip is scanning the higher the probability of an early thermally activated jump. Assuming a linear dependence of the energy barrier with increasing lateral force gives a logarithmic dependence of the lateral force with scan speed. Sang et al. [26] proposed that barrier-hopping fluctuations occur preferentially when the tip is close to slipping at the top of the barrier. This suggests that the friction scales with the logarithm of velocity to the power $2/3$. The increase in friction with increasing sliding velocity has been studied for polymer films grafted on silica [38], NaCl [12], Cu(111) [15] and glassy polymer films [39]. At high velocities the thermal vibrations have no time to act, and a transition from increasing friction to a constant plateau has been observed [40]. Reimann et al. [41–43] proposed a theoretical model for friction force microscopy experiments with special emphasis on the realistic description of dissipation and inertia effects. This model predicts a non-monotonic dependence of the friction force upon the sliding velocity of the tip over an atomically flat surface. The velocity dependence of friction in ambient conditions depends on the hydrophilicity of the surface [44]. Higher sliding velocities allow less time for the condensation of adhesive water necks, resulting in lower friction. Therefore, capillary forces can dominate the velocity dependence in air.

1.2.3 Superlubricity

Friction is the main cause of power losses in mechanical devices. Liquid lubricants are often used to reduce friction in macroscopic devices. On the molecular scale an enhanced viscosity of liquids confined in layers of molecular thickness has been observed [45]. Therefore, traditional

liquid lubricants do not work for Micro-Electro-Mechanical systems (MEMS) and, in order to reduce friction and wear in such devices one has to consider different mechanisms. In a modified scanning tunneling microscope experiment, Hirano et al. [46] observed a state of vanishing friction between a tungsten tip and a Si(001) sample. They predicted vanishing friction when two surfaces in contact are laterally stiff and incommensurate, because the lateral force acting between neighboring atoms of the contact should point in all directions and cancel each other out on average [47, 48]. Hirano named this state superlubricity, whereas Müser et al. called the same effect structural lubricity [49]. Dienwiebel et al. [50, 51]. observed superlubricity while dragging a graphite flake out of registry over a graphite surface and confirmed Hirano's theory. Another method to achieve ultra low friction is based on the reduction of the normal force applying on the contact. The atomic-scale stick-slip movement goes over in a continuous sliding without any abrupt jumps and hence dissipation decreases below a critical threshold. This method was studied in details by Socoliuc et al. [20] on NaCl in ultrahigh vacuum. Dry friction can be decreased as well by reducing the scan velocity down to a few nm/s or less. In this case thermally activated jumps occur in the contact area, and therefore the maximum lateral forces are smaller. This type of friction reduction is called thermolubricity [52]. Several ways to control friction at the nanometer scale without the use of lubricants have been suggested. However, none of them seems to be applicable to practical nanometer sized devices. An efficient way to switch friction on and off at the atomic scale was recently discovered by exciting the mechanical resonances of the sliding system perpendicular to the contact plane [53]. The resulting variations of the interaction energy reduce friction down to the detection limit of the instrument in a finite range of excitation and load, without any noticeable wear. Without actuation, atomic-scale stick-slip motion is observed, which leads to dissipation. In chapter 5 of this thesis we will discuss an extended Tomlinson model describing these findings. These simulations allowed us to calculate the residual friction force and the energy loss due to the actuation.

In summary, the Tomlinson model comprising of a single spring pulling a mass along a sinusoidal potential surface successfully explains a number of experimental observations, i.e. the occurrence of stick-slip as a function of load [20] and the damping of a lateral tip oscillation very close to the surface [54]. By including thermal activation in the Tomlinson model [26] experiments studying the velocity dependence of atomic-scale friction [12], the temperature dependence [39], and the jump force distribution [27] are all in agreement with the Tomlinson model. However, the experimental situation is not well represented by a model of a single spring pulling a mass along a sinusoidal potential. One spring can not reproduce both the resonance of the cantilever and the lateral stiffness of the contact. Therefore a two-spring model where one represents the cantilever and the other the microscopic contact is presented in chapter 4.4. All these results discussed before indicate the key role of the stick-slip instability for the dissipation of mechanical energy into heat. In chapter 4.4 the results of experiments and simulations which address in detail the dynamics of the atomic-scale slip are described.

1.3. Non-Contact Atomic Force Microscopy

Shortly after the invention of the AFM, Binnig et al. [55] reported on atomic resolution in contact mode on the graphite surface. Mate et al. [6] suggested that a flake of material could be responsible for the contrast formation. The fact that most of the so called atomic resolution images in contact mode showed always a perfect symmetry and did not show defects

let suggest that the atomic contrast in contact mode is a convolution of the tip and surface structure. This is reasonable considering that the size of contact presumably exceeds atomic dimensions. Howald et al. estimated a contact size of less than 1 nm^2 from AFM data at a cleavage step of NaF(100) [56]. However, there are only a few contact measurements showing point defects, i.e. on NaCl [57] and on LiF [58] suggesting true atomic resolution. Schimmel et al. [59] were also able to resolve kinks on a 2H-NbSe₂ surface and concluded that the tip structure plays a major role in contact mode atomic resolution images. The advantage of non-contact AFM compared to contact mode is the capability of true atomic resolution. True atomic resolution was achieved the first time on Si(111)-(7x7) by Giessibl [60] and InP(110) by Sugawara et al. [61] in 1995. In this thesis high-resolution non-contact AFM is used as a tool to study surface patterns due to strain relief of the lattice mismatch in the initial growth of heteroepitaxial thin films on insulators. Ultrathin films of KBr on NaCl(100) and of NaCl on KBr(100) were grown and the underlying atomic structure analyzed in real space. Moreover, the high resolution capabilities of contact mode AFM will be discussed by means of scans across atomic scale defects on such KBr-terminated surfaces.

In non-contact AFM, the forces acting on the tip close to the surface are dynamically measured. The free oscillation frequency of the cantilever is influenced by the tip-surface interaction resulting in a frequency shift. There are two ways to measure this frequency shift. One is based on amplitude detection where the cantilever is excited at a frequency close to the resonance frequency (AM-mode or tapping mode) [62]. If the eigenfrequency is shifted due to the force gradient the amplitude is changing and can be used as a feedback parameter to scan over the surface. This method is not convenient in ultrahigh vacuum because the high Q-factor of the cantilever would require an extremely slow feedback response. In the frequency modulation mode (FM-mode) [63], the cantilever is excited at its eigenfrequency and a feedback loop keeps the amplitude constant. In the first FM-detection setup, the AC-signal coming from the cantilever motion was amplified, phase shifted and then used as the excitation signal (self-excitation). The frequency shift, which arises due to the tip-sample interaction, is mainly used as a feedback parameter to control the tip-sample distance while scanning. The phase locked loop (PLL) has been successfully employed for that purpose because the oscillation is driven by the sinusoidal output of a voltage controlled oscillator, which is more stable in phase than in the self-oscillation scheme. A direct comparison between the self oscillation loop and the PLL setup is given by Kim [64]. The nc-AFM measurements presented in this thesis were measured with a PLL [65]. The detail of the used controlling scheme will be explained in chapter 2.2.

1.3.1 Relevant Forces

The interaction forces between tip and surface can be separated into chemical short-range forces with an interaction length of a fraction of nm and long range forces, which extend up to 100 nm. The long range capillary forces can be neglected in UHV. The long range Van der Waals forces act between the mesoscopic tip end and the surface, while the long range electrostatic forces interact with the whole cantilever. Therefore, the long range forces can be described as an interaction between macroscopic bodies. In contrast, the short-range forces take place between very few atoms of the tip apex. These forces provide information on the sample down to the atomic scale. The fact that in AFM different parts of the tip and cantilever contribute differently to the total force and feedback signal, respectively is in strong contrast to the STM, where only the foremost atoms contribute to the tunneling current. The

contribution of the outermost tip atoms dominates the tunneling current due to the strong exponential decay with the distance. The interplay of the different forces in AFM complicates the interpretation of the topographic measurements.

Short-range forces

Short-range chemical forces arise from the repulsion of the ion cores and the overlap of electron wave functions, which can be both, attractive and repulsive. The model potentials like the empirical Lennard-Jones potential or the Morse potential are essentially limited to the pairwise interaction of atoms. For example, the Lennard-Jones potential is an empirical model consisting of two terms which combine the attractive Van der Waals and repulsive atomic potential

$$V_{\text{Lennard-Jones}} = -E_{\text{bond}} \left(2 \frac{\sigma^6}{z^6} - \frac{\sigma^{12}}{z^{12}} \right), \quad (1.6)$$

where E_{bond} describes the binding energy and σ the equilibrium separation. Due to the variation of short-range forces on the atomic scale, atomic resolution becomes possible in atomic force microscopy.

Electrostatic forces

The contact potential difference between the surface and the tip creates charges at the surface and tip leading to electrostatic forces. These electrostatic forces can be partially compensated for by applying an appropriate bias voltage. With the Kelvin probe technique where the bias voltage between tip and surface is modulated to detect contact potential differences, the electrostatic forces can be simultaneously measured and dynamically compensated. Without active compensation of the long range electrostatic forces height measurements in nc-AFM can be influenced especially on heterogeneous materials [66].

Van der Waals forces

Van der Waals forces are caused by fluctuations in the electric dipole moment of the atoms and their mutual polarization. A detailed description of these forces can be found in the book by Israelachvili [67]. The Van der Waals potential between a spherical tip of radius R and a surface at distance z can be described by

$$V_{\text{vdW}} = -\frac{A_H R}{6z}, \quad (1.7)$$

where A_H is a material-dependent factor, called the Hamaker constant.

1.3.2 Dissipation Induced by Tip-Sample Interactions

In our setup the amplitude of the excitation voltage A_{exc} applied to the piezoactuator is controlled so that the amplitude of the tip oscillations is fixed at a constant value. Any energy dissipation in the tip-sample interaction damps the cantilever oscillation and requires an increase of A_{exc} . Therefore, A_{exc} is often referred to as the damping signal. Under some conditions the measured damping signal does not reflect the energy transfer from the oscillating cantilever into microscopic degrees of freedom of tip and sample. It is referred as apparent damping. One reason for apparent damping is that if the tip interacts with the sample, the motion of the cantilever can be slightly non-harmonic. In this case a part of the oscillation energy is stored in overtones of the cantilever frequency and the driving amplitude A_{exc} is increased to keep

the amplitude of the first harmonic constant. For large amplitude measurements this effect becomes negligible small. Apparent damping can also occur if the phase shift between driving signal and cantilever oscillation cannot be kept at -90° . Then, a larger excitation signal A_{exc} is needed to keep the oscillation amplitude constant. If the phase error signal is not recorded this A_{exc} signal can easily be misinterpreted as true dissipation.

Damping in the tip-sample contact arises from different phenomena and can be classified into velocity-dependent mechanisms and hysteresis related mechanisms. The later arises if the tip-sample interaction energy has two local minima and is bistable [68]. Then, forces on the oscillating cantilever can be different while approaching and retracting. This can occur if atomic positions are changing like atoms jump from the tip to sample or vice versa. Furthermore the viscoelastic response of the sample also leads to additional damping [69–71]. A velocity dependent damping mechanism observed by Denk and Pohl [72] is the Joule dissipation by charge carriers, which are driven by the time-varying electric field produced by the oscillation. This type of dissipation occurs when a voltage difference is applied between the tip and the sample or because the contact potentials of the two are not equal. Then the tip-sample capacitance is charged and discharged during each oscillation cycle. If the tip and sample are resistive, transport currents are generated and dissipate energy. Furthermore, Gauthier and Tsukada have proposed that damping occurs because of coupling of atomic vibrations caused by short-range forces [73–75].

A spatially resolved image of damping of the cantilever oscillation can be measured by recording the excitation amplitude A_{exc} while scanning over the surface. The excitation amplitude A_{exc} , which is needed to compensate for the internal friction, can be used to relate the recorded signal A_{exc} to the dissipated energy. Despite recent efforts, a quantitative understanding of A_{exc} is not straightforward [75, 76]. For example on the atomic scale the spatial correspondence of the maxima in the topography and dissipation images is found to depend strongly on the tip end and on the imaging conditions [77]. It has been reported that sometimes the maxima of the two images occurred at the same position, sometimes they were slightly laterally shifted, and sometimes the position of the maxima of the topography even agreed with the position of the minima of the dissipation. One explanation for this behavior is that the local contrast depends strongly on the tip apex such that the spatial correlation between the dissipation image and the topography is affected by tip changes.

The distance control by constant frequency shift normally used in non-contact force microscopy is complicated by the fact that the frequency shift versus distance characteristic is not monotonic. Whenever a frequency shift is chosen below the minimum of the curve, the controller jumps into the wrong branch of the curve immediately resulting in a tip crash. Alternatively, it has been suggested that one could use the dissipation signal for distance control due to the usually monotonic nature of this signal [78]. The characteristics of dissipation feedback is closer to tunneling microscopy than to conventional dynamic force microscopy controlled on constant frequency shift.

In chapter 6 of this thesis we exploit the damping signal [76] to reveal surface structures with very small topographic corrugation. By recording the damping signal simultaneously with the topography signal, subtle details of the surface topography can be detected which are often lost by the feedback circuit working with the more long-range frequency shift signal.

Experimental Setup in Ultrahigh Vacuum

2.1. Ultrahigh Vacuum System

The results presented in this thesis are from experiments performed on two different ultrahigh vacuum systems. The system at the University of Basel in the group of Prof. E. Meyer (chamber I, Fig. 2.1(a)) consists of three chambers separated by valves: The analysis chamber (A-chamber), the preparation chamber (P-chamber) and a fast entry lock. The system of Prof. R. Bennewitz at McGill University in Montreal, Canada, (chamber II, Fig. 2.1(b)), which was used during a study visit of one year, comprises only an analysis chamber and a fast entry air lock.

The main part of both analysis chambers is a home-built room temperature atomic force microscope, which will be described in detail in the next section. Both analysis chambers have an electron gun and a screen to perform Low-Energy Electron Diffraction (LEED) and Auger Electron Spectroscopy (AES) measurements. LEED is used to determine the crystalline structure of a surface, while Auger electron spectroscopy provides information on the chemical composition of a sample. In the case of alkali halides, the electron gun of the LEED is also

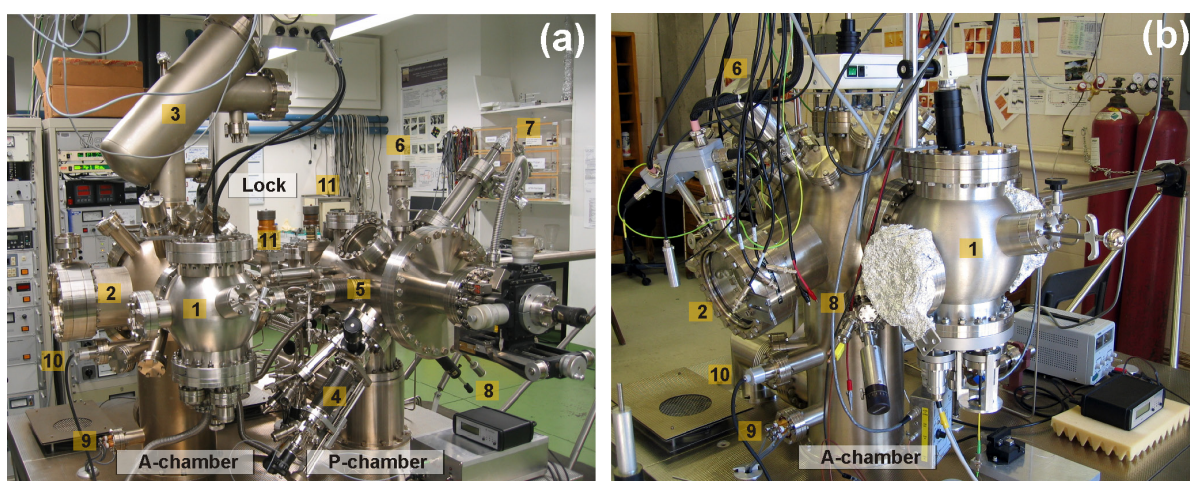


Figure 2.1: Picture of the (a) UHV-system I and (b) UHV-system II equipped with (1) AFM (2) LEED/AES (3) XPS (4) molecule evaporator with three Knudsen cells (5) quartz-balance (6) sputter-gun (7) atom source (8) home-built evaporator (9) titanium sublimation pump and (10) pressure gauge (11) valve, which separates the chambers.

used for sample preparation. On a KBr(100) crystal, rectangular straight-edged pits of one monolayer depth can be created by exposing the surface shortly to an electron beam [79–81]. Thus, molecules can be trapped in such pits for example, as shown by Nony et al. [82, 83]. In addition, vacuum chamber I has an X-ray photoelectron spectroscopy system (XPS).

Both systems are equipped with a sputter gun and an electron bombardment heater used for the preparation of metallic samples by Ar-sputtering and annealing cycles. There is a direct current heater and a resistive heater in both systems as well. A home-built evaporator with one Knudsen cell was used for the evaporation of salt films in system II. In system I a commercial evaporator with three cells was used for this purpose. A valve between the P-chamber and the evaporator has the advantage that you can exchange these cells without breaking the UHV in the preparation chamber. This evaporator is also used for the sublimation of molecules. In addition, another home-built evaporator was used for the deposition of gold. The crucible of this evaporator is mounted on a sample-plate and thus can be brought into UHV over the lock. Two different quartz-balances enable us to monitor and calibrate the evaporation rate in system I. The preparation chamber in system I is equipped with additional tools to prepare clean surfaces: A cleaving tool is used to cleave ionic crystals in UHV, which is crucial for the preparation of a clean NaCl surface. An atom source provides neutral oxygen or nitrogen. These neutral gas atoms have proven to be very effective in low damage surface treatments such as nitridation and oxidation. A direct current heating platform with a gas inlet in the lock of system I makes it possible to heat samples in a pure gaseous atmosphere.

These two systems are pumped by a combination of turbo-pumps, ion getter pumps and titanium sublimation pumps. During measurements the systems are pumped by the ion getter pumps and the turbo-pumps are switched off to avoid mechanical vibrations. The base pressure in both analysis chambers is below 10^{-10} mbar.

2.2. The Atomic Force Microscope

The two home-built atomic force microscopes used in this work, both operated at room temperature, are similar in design to the one described by L. Howald et al. [84]. The AFM is built on a platform suspended by four springs and damped by an eddy current damping system in order to decouple it from external mechanical vibrations. The deflection of the cantilever is detected by the optical beam deflection method [3], which allows us to measure the normal and lateral bending of the lever simultaneously (compare Fig. 1.2). The light of a superluminescent diode is coupled into a fiber which is introduced into the vacuum by a swagelock-feedthrough filled with teflon [85]. The light beam is then focused by a lens and guided over a first motorized mirror to the back of the cantilever and from there over another motorized mirror to the position sensitive four-quadrant diode. The mirrors can be adjusted by piezo motors. The signal of the quadrant diode is directly amplified in UHV. This guarantees a high quality signal and a unique signal bandwidth of 3 MHz. There is also a tunneling preamplifier with changeable resistor between 10^{-8} - 10^{-10} Ohm in UHV. The sample-holder sits in front of a tube piezo, which performs the scan movement while the tip remains fixed. The sample with the piezotube is attached to a walker which can be moved by three piezo stacks for the coarse approach. The tip holder is glued on a shaking piezo to excite the cantilever for non-contact measurements. A bias voltage can be applied on both the tip or the sample in order to compensate the contact potential between tip and sample, and for STM operation.

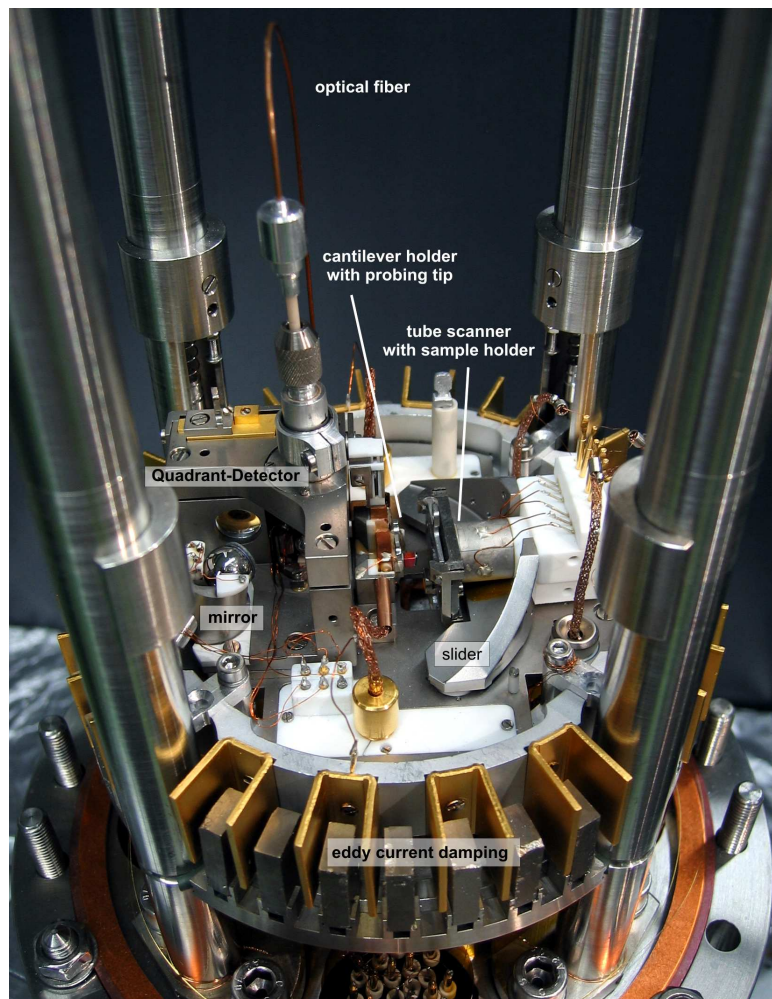


Figure 2.2: Picture of the home-built UHV-AFM in system I.

The AFM can be operated in contact as well as in non-contact mode. A scheme comprising all the controllers and filters for the non-contact and contact mode is shown in Fig. 2.3. For the non-contact mode experiments, the cantilever has been excited with a driving amplitude A_{exc} to oscillate at the first bending resonance with constant amplitude. The tip-sample distance can be controlled by maintaining constant negative shift of the resonance frequency with respect to the resonance far from the surface, by constant damping, or by constant tunnel current. Fig. 2.3 (a) shows a scheme of the constant frequency shift mode: The amplified and bandpassed filtered A-B signal of the four-quadrant diode is fed into a phase locked loop (PLL), which measures the difference Δf between a set frequency and the actual frequency of the cantilever. At the same time, the A-B signal is fed into an RMS-to-DC converter which provides the input signal of the amplitude controller to maintain a constant oscillation amplitude. Typical amplitudes used for non-contact measurements ranged from 5 nm to 20 nm.

Additionally, the microscope can be operated as a Kelvin force microscope, where an AC-voltage is applied between tip and sample for the detection of electrostatic forces. Two dif-

ferent methods can be employed for Kelvin measurements: the frequency modulation (FM) mode [86] or amplitude modulation (AM) mode [87, 88] detection. In FM-mode, the oscillation amplitude of the frequency shift at the modulation frequency is measured. The oscillation amplitude is proportional to the gradient of the electrostatic force. In AM-mode, the amplitude of the cantilever oscillation at a certain frequency is measured. The amplitude is proportional to the electrostatic force itself. By tuning the modulation frequency to a higher resonance of the cantilever, a resonant and therefore very sensitive way to detect the signal is achieved in the AM-mode [88].

In contact mode, the normal deflection signal is used as a signal for the distance control. In friction force microscopy experiments, the tip scans at a constant height over the surface while the normal and torsional deflection are measured. In this case, the gains of the distance controller are kept at very low values in order to avoid any influence by the topography.

In system I, some home-built scan electronics and scan software is used, while in system II a combination between home-built [89] and commercial scan electronics (SCALA, Omicron Nanotechnology) was used in combination with a Nanosurf easy PLL and the scan software SCALA.

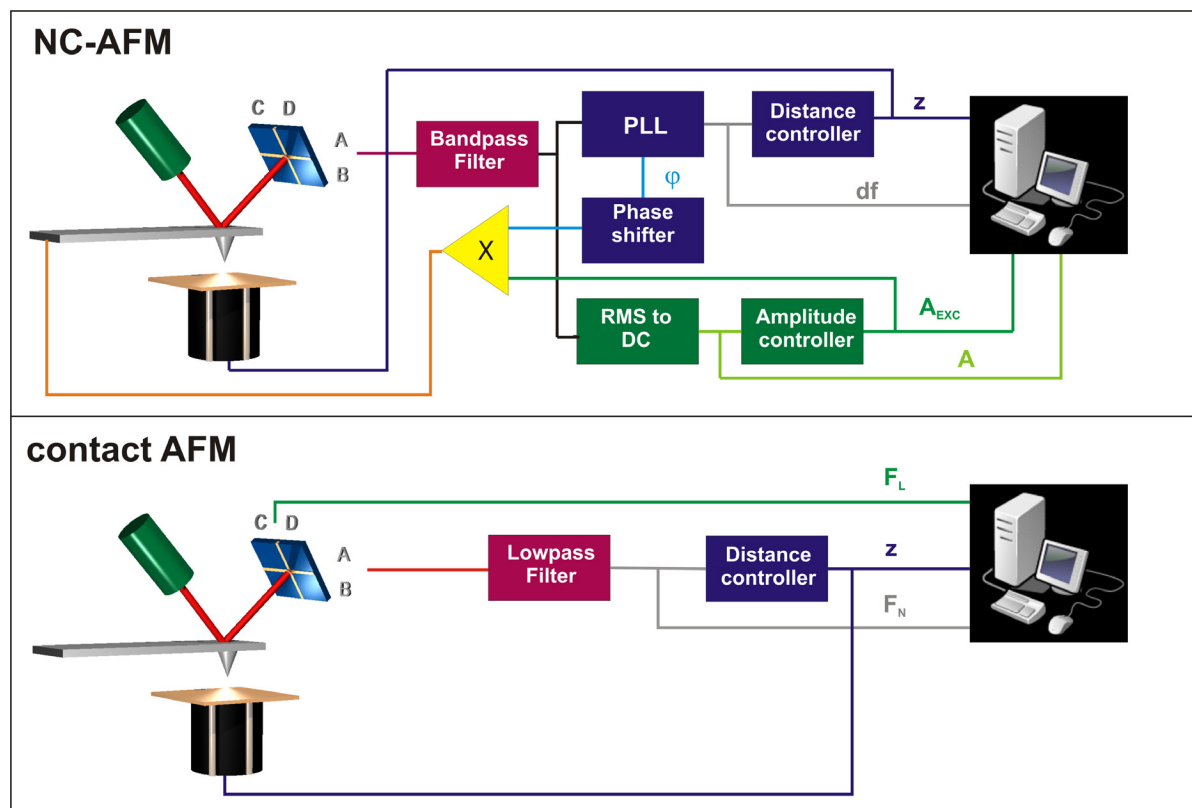


Figure 2.3: Scheme comprising all the controllers and filters for controlling AFM in the non-contact and contact mode.

2.3. Calibration of Forces and Amplitudes

In this section, methods for the calibration of forces in contact mode as well as the determination of the amplitude and Q-factor in non-contact mode are explained.

Calibration of the Stiffness and Force in Contact Measurements

If we assume that the elastic deformation of the tip and the sample in contact mode are negligible, the normal force F_N and lateral force F_L are a function of the differential signal from the photo diode U_{A-B} and U_{C-D} respectively, the sensitivity of the detector s_z in nm/V and the spring constant k of the cantilever [90]

$$F_N = k_N s_z U_{A-B} \quad \text{and} \quad F_L = \frac{3}{2} k_T \frac{h}{l} s_z U_{C-D}. \quad (2.1)$$

The sensitivity s_z can be determined from a force-distance curve as shown in Fig. 2.4. The force-distance curve should be taken on a hard surface to ensure that elastic deformation of the sample can be neglected. Several methods to measure the spring constants of a rectangular cantilever have been suggested based on additional mass attached to the cantilever [91] and on the viscous damping of the cantilever oscillation in air [92] or the so-called wedge-method [93, 94]. In this work, the spring constants k_N for normal bending and k_T for the torsional mode were calculated from its geometry [90, 95, 96]

$$k_N = \frac{Ewt^3}{4l^3} \quad \text{and} \quad k_T = \frac{Gwt^3}{3h^2l}. \quad (2.2)$$

Scanning electron microscopy can be used to determine the relevant dimensions of the cantilever: Length l , width w and height h of the tip. The thickness t can be determined from the fundamental resonance frequency f of the cantilever [97]

$$t = \frac{2\sqrt{12}\pi}{1.875^2} \sqrt{\frac{\rho}{E}} f l^2. \quad (2.3)$$

In Eq. (2.3), the cantilever is considered as a beam only, neglecting the tip. For the material constants of silicon the following values were used: $E = 1.69 \cdot 10^{11}$ N/m for the elastic modulus, $G = 6.8 \cdot 10^{10}$ N/m for the shear modulus and $\rho = 2328.3$ kg/m³ for the density [95].

Calibration of the Oscillation Amplitude in Non-Contact AFM

The oscillation amplitude of the cantilever in non-contact mode can be determined with the help of the calibrated z -piezo. The principal idea is to compare the change in z for different amplitudes with the change in the oscillation amplitude [98]. On insulating materials, the distance between the tip and sample is normally controlled by keeping the frequency shift constant. Because the frequency shift depends on the oscillation amplitude $f \propto A^{-3/2}$ [99, 100], the distance control has to be readjusted for every amplitude. For example, the amplitude controller is set to a small stable amplitude with setpoint A_0 , the tip is then approached on a flat surface and the tip-sample distance controlled on a constant frequency shift f_0 . If the amplitude is now increased by a factor c , the distance controller has to be changed to a new setpoint $f_1 = f_0 c^{-3/2}$. The difference in the measured z -positions for both amplitudes divided by the measured voltage difference of the peak-to-peak amplitude of the oscillation results in a conversion factor nm/V. With this conversion factor the peak-to-peak amplitude in volts can be calibrated in nm. In case of conductive samples, controlling on tunneling current is suggested for a more accurate calibration.

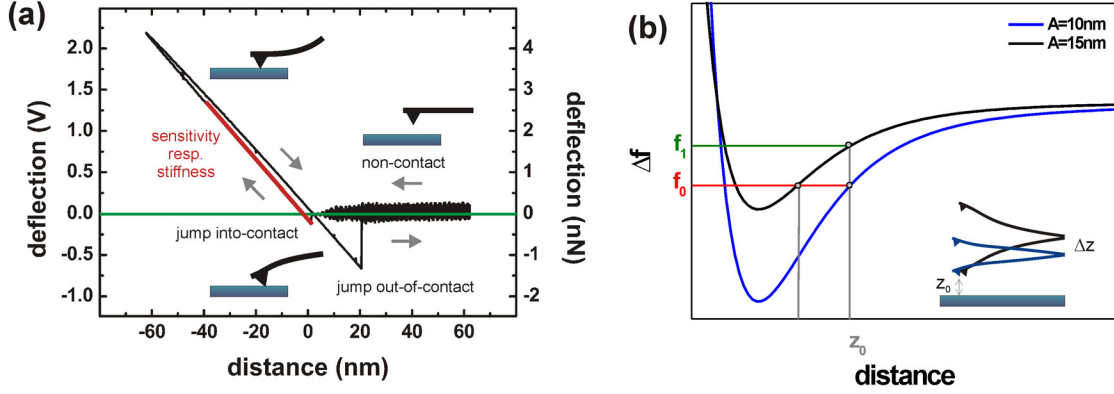


Figure 2.4: (a) Force-distance curve measured on an atomically flat KBr(100) (b) Sketch to the amplitude calibration: It shows how the Δf has to be adjusted upon an amplitude increase in order to keep the same distance to the sample.

Determination of the Q-Factor

The Q-factor of the free cantilever is a measure for the power dissipation in dynamic force microscopy. This dissipation is independent of the tip-surface interaction and cannot be avoided. Because the Q-factor is inverse proportional to the force sensitivity it is an advantage to have high Q-factors [63]. The Q-factor for a cantilever operated in air is mainly limited by viscous damping and typically amounts to a few hundred, while in vacuum, only internal and surface effects in the cantilever material are responsible for damping and Q reaches hundreds of thousands. There are different ways to determine the Q-factor far from the surface. One possibility is to sweep the frequency and simultaneously record the amplitude A or the phase ϕ of the cantilever oscillation. The amplitude respectively phase are related to the frequency by

$$A(f) = \frac{A_0}{\sqrt{(1 - (f/f_0)^2)^2 + (f/f_0 \cdot Q)^2}} \quad (2.4)$$

$$\phi(f) = \arctan\left(\frac{1 - (f/f_0)^2}{f/f_0} Q\right) + \phi_0 \quad (2.5)$$

where f_0 is the resonance of the free lever and Q the quality factor. These relations can be derived from the equation of motion of a free cantilever [95]. Fig. 2.5 shows the measured amplitude and the phase with the corresponding least-square fits while sweeping the frequency around the first normal resonance frequency. Alternatively, the phase can be varied while measuring the frequency and amplitude. In this work, both methods were used to determine the Q-factor of a non-contact lever far away from the surface.

The Q-factor of a cantilever can also be deduced without any excitation of the lever just from thermal fluctuation measurements. The analytical curve given below is fitted to the resonance peak [101, 102]

$$S(\omega) = \frac{2k_B T \omega_n^3}{D_n Q \left((\omega^2 - \omega_n^2)^2 + \frac{\omega_n^2 \omega^2}{Q^2} \right)}, \quad (2.6)$$

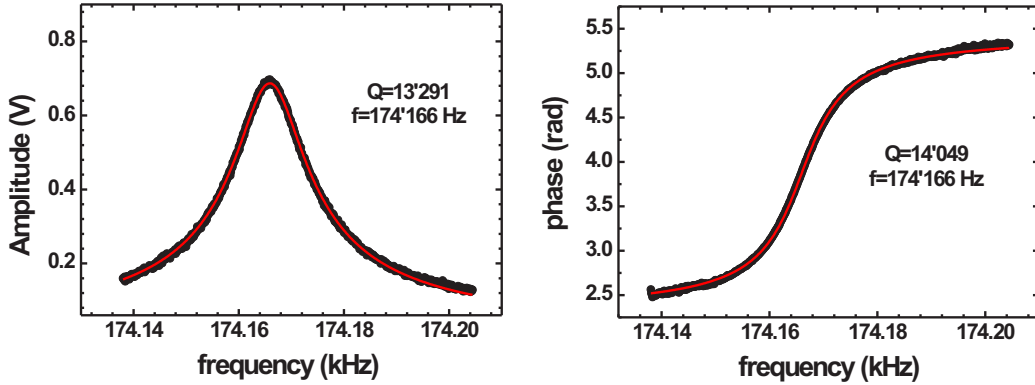


Figure 2.5: Example of a frequency sweep around the first normal resonance frequency of a silicon non-contact cantilever with a reflective aluminum coating at the backside: (a) measured amplitude and (b) measured phase versus excitation frequency.

where D_n is the spring constant of the n -th eigenmode, Q the quality factor, ω_n the eigenfrequency of the n -th eigenmode and k_B the Boltzmann constant. The temperature T was set to 300 K in this work as all the measurements were performed at room temperature. Fig. 2.6 gives an example of the torsional resonance of a free cantilever with the corresponding fit. The fit using Eq. (2.6) reveals a frequency of $f = 157.3$ kHz, $Q = 223,800$ and $k = 80.96$ N/m for the free contact cantilever. This method is mainly used in chapter 3.

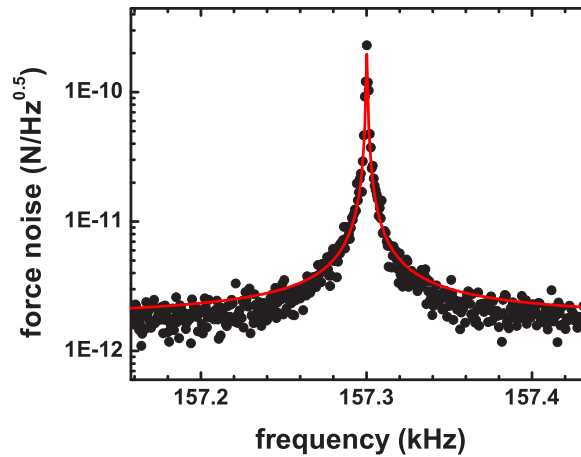


Figure 2.6: Power spectral density showing the peak corresponding to the first torsional resonance of a free rectangular contact lever. The fit according to Eq. (2.6) reveals a frequency of 157.3 kHz, $Q = 223,800$ and $k_T = 80.96$ N/m.

Another accurate method to determine the high Q-factor is the ring-down method, where the oscillation amplitude is measured as a function of time after stopping the external excitation of the cantilever resonance. The ring-down follows an exponential decay and can be fitted with the following formula [102]

$$A(t) = A_0 \exp\left(-\pi \frac{f}{Q}(t - t_0)\right), \quad (2.7)$$

where A_0 is the excitation amplitude and t_0 the switch of time of the external oscillation. This method was used to confirm the Q-factor of a contact lever in contact, see chapter 3.2 respectively Fig. 3.2.

2.4. Properties and Preparation of the Cantilevers

We used commercial, microfabricated, rectangular cantilevers made of silicon with integrated tips as a force sensor. They are fabricated from highly doped silicon to avoid charging and to allow for combined tunneling and force microscopy experiments. The tips have pyramidal shapes and are produced by etching processes. For atomic-resolution images, the front atom of the tip should ideally be the only atom that interacts strongly with the sample. In order to reduce the forces caused by the shaft of the tip, the radius of the tip apex should be as small as possible. The typical tip radius used in this work is less than 10 nm [103]. Special cantilevers are used for the different operation modes of an atomic force microscope. In contact mode the stiffness of the cantilever should be less than the interatomic spring constants of atoms in a solid, which amount to $k < 10$ N/m. For contact measurements, predominantly silicon contact cantilevers bearing sharp tips with a spring constant of the order of $k_N = 0.09$ N/m for the normal bending and $k_T = 62$ N/m were used. The stiffnesses change slightly from tip to tip, because the thickness of the cantilever and hence the first normal resonance frequency are different. In dynamic force microscopy, cantilevers with higher stiffness help to reduce noise and increase stability and prevent the tip from jumping into contact [104]. The properties of the different type of levers used in this work are summarized in Table 2.1. For non-contact measurements, cantilevers with an aluminum coating of approximately 30 nm thickness on the detector side were typically used. This enhances the reflectivity of the light beam by a factor of 2.5 and furthermore prevents light from interfering within the cantilever. For load dependence studies of the resonance in section 3.3, an alternative set of rectangular silicon contact cantilevers with a spherical tip (Nanosensors) was used for comparison. The radius of curvature of the sphere was determined using scanning electron microscopy to be 0.9 μm , (see Fig. 2.7). The spring constant for this tip was $k_N = 0.11$ N/m for normal bending and $k_T = 82$ N/m for torsion. The other cantilever dimensions are identical to normal contact cantilever. Etched tungsten or cut platinum-iridium wires can be used as tips for measuring STM in our system as an alternative to a microfabricated cantilever.

The commercial cantilevers are glued onto a tip holder which assures a good optical path in the system. After introducing the tips into vacuum, they are heated at 120° C for half an hour in order to remove water and contaminants. The silicon tips are covered with a thin layer of a few nm of silicon oxide as no special tip treatments have been applied. The native oxide layer could be removed by annealing in situ above 900° C by electron-beam bombardment [105], HF-etching before introducing into UHV [106], or sputtering.

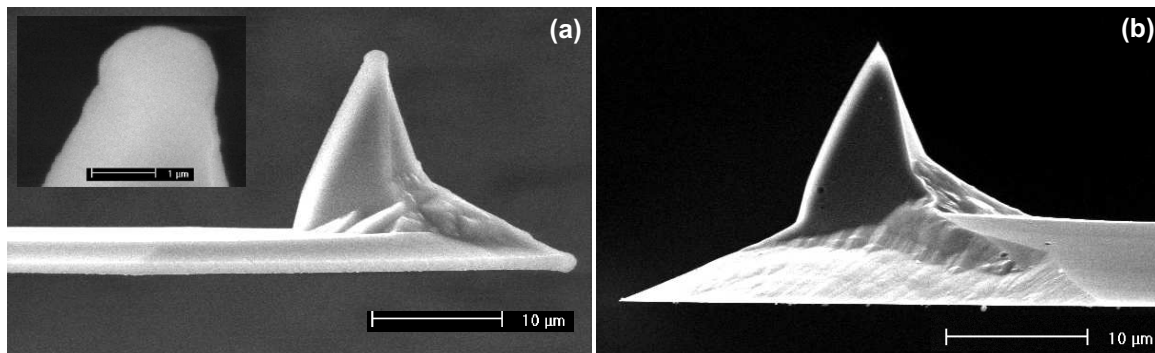


Figure 2.7: (a) Scanning electron microscopy image of a rectangular silicon cantilever with a spherical tip with a curvature radius of $0.9 \mu\text{m}$. (b) Scanning electron microscopy image of a rectangular non-contact silicon cantilever.

	contact lever	non-contact lever
thickness t	$1.3\text{-}2.1 \mu\text{m}$	$6.6\text{-}7.5 \mu\text{m}$
width w	$44\text{-}46 \mu\text{m}$	$34\text{-}36 \mu\text{m}$
length l	$453 \mu\text{m}$	$226 \mu\text{m}$
force constant c	$0.046\text{-}0.21 \text{ N/m}$	$35\text{-}54 \text{ N/m}$
normal resonance frequency f_0	$9\text{-}14 \text{ kHz}$	$177\text{-}198 \text{ kHz}$

Table 2.1: Properties of the different types of rectangular silicon cantilevers used in the experiments.

2.5. Sample Preparation

Under atmospheric pressure, all kinds of adsorbed particles form an adlayer on the topmost atomic layers of a solid. The chemical composition and geometrical structure of these adlayers are usually not very well defined. Thus, real surfaces exposed to atmospheric pressure are very complex and these adlayers hinder a clear analysis of the underlying surface structure and the controlled adsorption of a single and pure species. In ultrahigh vacuum, there are several techniques to prepare clean and well-defined surfaces. Brittle materials like alkali halides can be prepared by cleaving. Surfaces can only be cleaved along certain crystallographic directions. Sputtering and annealing cycles are the most versatile cleaning techniques for metal surfaces. Contaminants and the topmost atomic layers of the crystal are sputtered off by the bombardment with noble gas ions. Subsequent annealing is necessary to remove embedded and adsorbed noble gas atoms and to recover the surface crystallography. It is possible that during the annealing further impurities from the bulk segregate to the surface, so that the ion bombardment/annealing cycle has to be repeated several times [107].

The experiments which will be described in the following chapters were mainly performed on alkali halides, namely potassium bromide (KBr) and sodium chloride (NaCl). Alkali halides are a model system due to their simple structure and their reproducible preparation by cleaving. If an insulating ionic crystal is cleaved, the crystal and especially the region below the new surface become plastically deformed due to the large stress during cleavage [108]. Therefore,

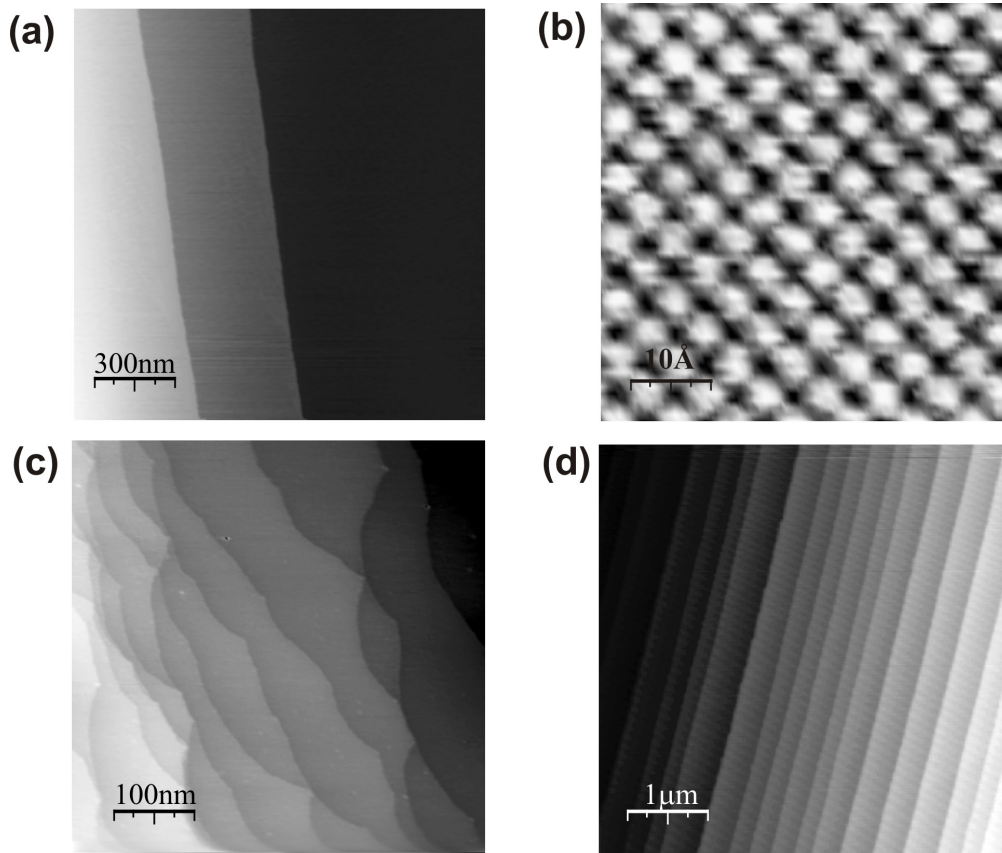


Figure 2.8: Sample preparation: (a) Contact AFM image showing monatomic steps on a KBr surface after cleaving in air and annealing at 120°C in UHV (Load 0 nN). (b) Atomic resolution on KBr obtained with nc-AFM. (c) Clean Cu(100) surface after sputtering and annealing recorded with nc-AFM. (d) Tapping mode AFM image revealing monatomic steps on Al₂O₃ after annealing in air at 1400°C recorded in tapping mode in air.

in most cases the crystals are charged afterwards. These residual charges from the cleavage make it difficult to image the surface by AFM. In order to reduce the electrostatic forces a bias voltage can be applied between the tip and the surface while measuring, but often the highest possible applicable voltage in our setup is not enough. Careful heating in vacuum at around 120°C can help to reduce the charges and still preserve the stoichiometry of KBr and NaCl. Heating in vacuum at higher temperatures, 330°C for KBr and 400°C for NaCl, results in molecular evaporation from corner sites of steps. This process smoothes cleavage steps, and spirals of steps around the intersection of dislocations with the surface are formed. Such spiral steps provide a regular array of monatomic or diatomic steps separating atomically flat terraces with a typical width between 50 and 150 nm [109, 110].

In our experiments we were interested in clean alkali halide surfaces with large atomically flat terraces. Therefore, the KBr(100) surfaces were prepared by cleaving a single crystal in air, followed by a quick transfer to the vacuum system and annealing in ultrahigh vacuum at 120°C for 30 minutes. The NaCl single crystals were cleaved in UHV and heated at 150°C for 30 minutes in order to remove charges produced in the cleaving process. A cleaved KBr surface with large flat terraces is shown in Fig 2.8(a). Fig. 2.8(b) reveals true atomic resolution in

non-contact mode on KBr(100).

The load dependence experiments with the spherical tip in chapter 3.3 were performed on the hard $\text{Al}_2\text{O}_3(0001)$ single crystals which guaranteed negligible deformation of the sample. The $\text{Al}_2\text{O}_3(0001)$ sample was heated in air at 1400°C for four hours and in UHV at 120°C for 30 minutes, producing clean atomically flat terraces with a typical width of 60 nm [111]. Fig. 2.8(d) shows these monatomic steps on $\text{Al}_2\text{O}_3(0001)$ after heating in air. Annealing $\text{Al}_2\text{O}_3(0001)$ in UHV to high temperatures of around 1300°C would result in the loss of oxygen relative to aluminum in the outermost layers and therefore different reconstructions are observed [112–115]. Subsequent heating of the crystal in oxygen atmosphere produces surfaces similar to the bulk terminated structure [116, 117]. In contrast to the extremely hard surface of Al_2O_3 , copper was used as a very soft material in this study. Cu(100) was prepared by several cycles of 20 minutes Argon-ion sputtering ($E = 1$ keV) and 20 minutes annealing (450°C) in UHV. A prepared Cu(100) after several cycles of sputtering and annealing is shown in Fig. 2.8(c).

3

The Influence of the Tip-Sample Contact on Thermal Fluctuations of a Cantilever

3.1. Introduction

The collective mechanical behavior of a multitude of small contacts affects the friction between sliding bodies on the macroscopic scale. Friction force microscopy is used to study the sliding of a sharp tip over an atomically flat surface on the nanometer-scale. This single asperity contact between tip and substrate is a complicated system involving many atoms and is constantly deformed, ruptured and reformed. Unfortunately, no experimental estimates for several parameters such as the mass or the damping of the contact exists. A thermal fluctuation analysis of the cantilever while it is in contact provides a lot of information about the nature of the contact. It allows us to study the contact without scanning, which avoids the permanent rupture of the contact and reduces the atom transfer between tip and sample, which can permanently change the contact. The measured thermal noise of the cantilever was used to determine quantities such as the spring constant of a cantilever [118], or the tip-sample interaction potentials [119–122]. Drobek et al. [123] investigated the elastic properties of the tip-sample contact by analyzing the thermomechanical noise of a surface coupled cantilever at room temperature in air. They extracted the shear stiffness of the tip-sample contact from a power spectrum analysis of the lateral force signal. On the other hand, thermal fluctuations of the cantilever are one of the most significant sources of noise in an atomic force microscope and therefore affect the measurement process by defining the lowest achievable force resolution of the instrument.

In this chapter, we discuss thermal noise measurements of a cantilever in ultrahigh vacuum and we analyze the influence of the tip-sample contact on the thermal fluctuations. Frequency spectra and ring-down measurements were performed to study the strong damping of the cantilever occurring by the tip-sample contact. The advantage of performing such measurements in ultrahigh vacuum is that viscous damping which dominates in ambient atmosphere is suppressed. The measured damping in UHV is only caused by intrinsic damping of the cantilever and damping due to the tip-sample interaction. Moreover, the contact stiffness for different contact sizes was determined from the shift of the resonance peak due to the tip-sample interaction. Such an analysis allows us to explore the limits of continuum mechanics. Finally, these findings are discussed in terms of simple mechanical models, such as a point mass model or beam equation.

In thermodynamic equilibrium, the mean-square displacement of the tip from its neutral position due to thermal activation can be estimated from using the equipartition theorem. Choosing a normal stiffness of $k_N = 0.09$ N/m and a lateral stiffness of $k_T = 62$ N/m for the

cantilever results in a normal respectively lateral mean square displacement of

$$\sqrt{\langle u_z^2 \rangle} = \sqrt{\frac{k_B T}{k_N}} = 212 \text{ pm} \quad \text{and} \quad \sqrt{\langle u_x^2 \rangle} = \sqrt{\frac{k_B T}{k_T}} = 8 \text{ pm} \quad (3.1)$$

for the cantilever at room temperature ($T=293$ K). In friction measurements, a low lateral contact stiffness was found typically of the order of 1 N/m [20]. Since the contact is associated with a lower stiffness than the cantilever, larger thermal amplitudes of the order of 60 pm are found. Nevertheless, the lateral thermal noise amplitude of the lever and contact are much smaller than typical atomic distances. Thus, the tip stays in its equilibrium position and the probability of spontaneous hopping to an adjacent equilibrium position is small in the absence of any further external driving forces. If the cantilever deflections are detected by the optical beam deflection method, the measured amplitudes of the thermal noise are usually different from the actual thermal noise of the cantilever, because the photodiode signals are related to bending and twisting angles. The optical beam deflection method is hence more sensitive to the slope of the cantilever rather than to its displacement. Butt and Jaschke calculated the thermal displacement of a cantilever and distinguished between the actual thermal noise and the measured thermal noise which is obtained using optical beam deflection method assuming a infinitesimal spot size [124]. This study was extended by Schäffer to a finite optical spot size [125]. A calibration of the photodiode signal as described by Pfeiffer et al. [102] was not done for the results presented in this chapter.

The analysis of the thermal noise in ultrahigh vacuum requires a high bandwidth in the measurement electronics. In the atomic force microscopes used for these measurements, a fast preamplifier is integrated into ultrahigh vacuum in order to keep low-voltage signal lines from the photodiode very short. This provides a high bandwidth of 3 MHz . This bandwidth allows the study of the normal and torsional oscillation of a cantilever as well as some of its higher modes. For the fluctuation analysis, both the normal and the torsional deflection of the cantilever were acquired with sampling rates of up to 20 MHz using a digital oscilloscope card (National Instruments, NI5102). The acquisition and detailed analysis of these signals including the calculation of a Fast Fourier Transformation (FFT) to study the properties of the cantilever resonances was done with a LabVIEW program written by the author [126].

3.2. Frequency Spectrum of Thermal Fluctuations: From Non-Contact to Contact

Normal and lateral force signals were simultaneously recorded to characterize the dynamic properties of the cantilever force sensor driven by thermal fluctuations. Fig. 3.1(a) shows a typical overview power spectral density (PSD) plot including higher normal and torsional modes of a free contact lever as used in atomic friction experiments. We identify the first eight modes in the normal spectrum and the first five modes in the torsional spectrum. A cross-coupling between the normal and torsional deflection signal is observed: In the normal spectrum there are peaks at the position of a torsional resonance and vice versa. This cross-coupling originates from a suboptimal alignment of the cantilever in the optical path. Table 3.1 summarizes the measured frequencies of the higher normal and torsional modes. The expected ratio of the resonance to the fundamental frequency is obtained by solving a beam equation for a rectangular beam as described by Rabe et al. [127]. These ratios are in good agreement with the experiment. The small but systematic deviations of the theoretical frequencies for higher

modes are due to deviations from the rectangular shape at the cantilever end, and the neglected mass of the tip. The eigenmodes of the free contact cantilever were simulated by finite elements using the software FEMLAB to illustrate the first normal and torsional eigenmodes in Fig. 3.1. The geometrical parameters used are listed on page 23. The lateral eigenmodes are omitted since they cannot be detected by the optical beam deflection method.

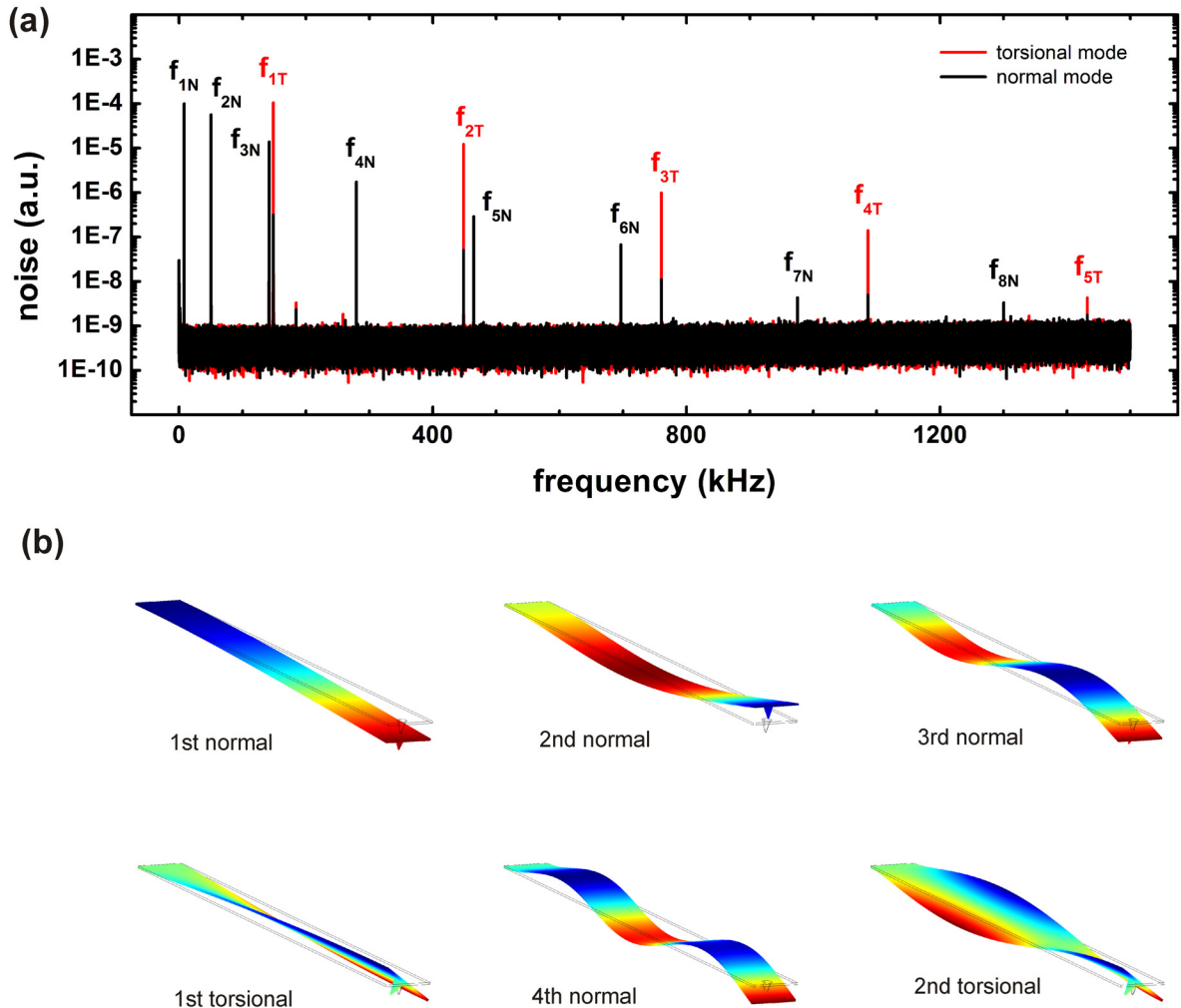


Figure 3.1: (a) Power spectral density of thermal fluctuations in the normal and lateral force signal showing peaks corresponding to the resonances of a free rectangular contact cantilever and its higher modes. (b) Finite element simulation of a rectangular contact lever, as used in atomic friction experiments, showing the first six eigenmodes as observed in atomic force microscope experiments by optical deflection method. The eigenmodes are ordered according to their resonance frequency starting with the smallest frequency. The color coding is proportional to the displacement in z -direction.

Thermal fluctuations of the free cantilever, especially the normal mode, have already been measured in ambient atmosphere as well as in UHV and discussed in detail, see e.g. Refs. [101, 102, 127, 128]. However, about the torsional mode in particular with the tip in contact little is known. In this section, measurements of thermal fluctuations in the lateral force are

mode number	normal mode			torsional mode		
	f_{exp}^i (kHz)	f^i/f_{exp}^1 (kHz)	f^i/f_{theo}^1 (kHz)	f_{exp}^i (kHz)	f^i/f_{exp}^1 (kHz)	f^i/f_{theo}^1 (kHz)
1	7.97	1	1	148.97	1	1
2	50.44	6.3	6.27	448.73	3.0	3
3	141.97	17.8	17.53	760.57	5.1	5
4	279.62	35.1	35.39	1086.29	7.3	7
5	464.53	58.3	56.84	1432.34	9.6	9
6	696.56	87.4	84.91			
7	975.12	122.3	118.59			
8	1300.33	163.2	157.91			

Table 3.1: Frequencies of the higher normal and torsional modes of a free rectangular cantilever measured in UHV from the power spectral density plot in Fig. 3.1. The expected ratio of the resonance to the fundamental frequency is obtained by solving a beam equation for a rectangular beam as described by Rabe et al. [127].

presented, where the changes of the resonance peak upon contact formation is of special interest. Fig. 3.2(a) compares the measured power spectral density of the lateral force for the free cantilever and for the cantilever with the sharp tip resting in contact with a KBr(100) surface. The sharpness of the peak at 168.6 kHz reflects the high quality factor of $Q_{free} \sim 350000$ for this oscillation mode. When the tip is in contact, the resonance frequency shifts to 172.5 kHz, and its width increases significantly. Assuming a harmonic oscillator model to be adequate, the width corresponds to a new Q-factor of $Q_{contact} \sim 700$. The Q-factors for both the free cantilever and the cantilever with the tip in contact were determined with a least-square fit to the resonance curves using Eq. (2.6). Because the peak in contact is relatively weak compared to the noise level, additional ring-down measurements for an externally excited cantilever were performed to confirm the quality factors. For these measurements the cantilever was externally excited with a function generator, with an excitation amplitude small enough so that the cantilever did not jump out of contact. Fig. 3.2(c) shows the ring-down of the oscillating lateral force signal after stopping the external excitation. The ring-down of the amplitude in Fig. 3.2(c) with the corresponding least-square fit using Eq. (2.7) reveals a quality factor of 335, which is of the same order of magnitude as that obtained by fitting the resonance in thermal noise spectrum. The factor two difference is put down to the fact that a different lever was used for the ring-down measurements shown here.

First, let us discuss the increase of the torsional resonance frequency upon contact formation. This increase can be explained by the additional stiffness caused by the fixation of the tip apex. It has been observed in ambient environment and described in a finite element analysis by Drobek et al. who used such measurements to determine the shear stiffness of the contact [123]. In section 3.5 we will discuss different models for a quantitative analysis of the frequency shift upon contact formation. In Fig. 3.2(a) we do not only observe a shift of the resonance frequency but also a drastic increase of the width of the resonance peak, corresponding to a drop in the quality factor by nearly three orders of magnitude, upon contact formation. This observation is only possible in vacuum, as in earlier studies in ambient environment the quality factor is dominated by air damping. Let us consider possible sources of additional dissipation,

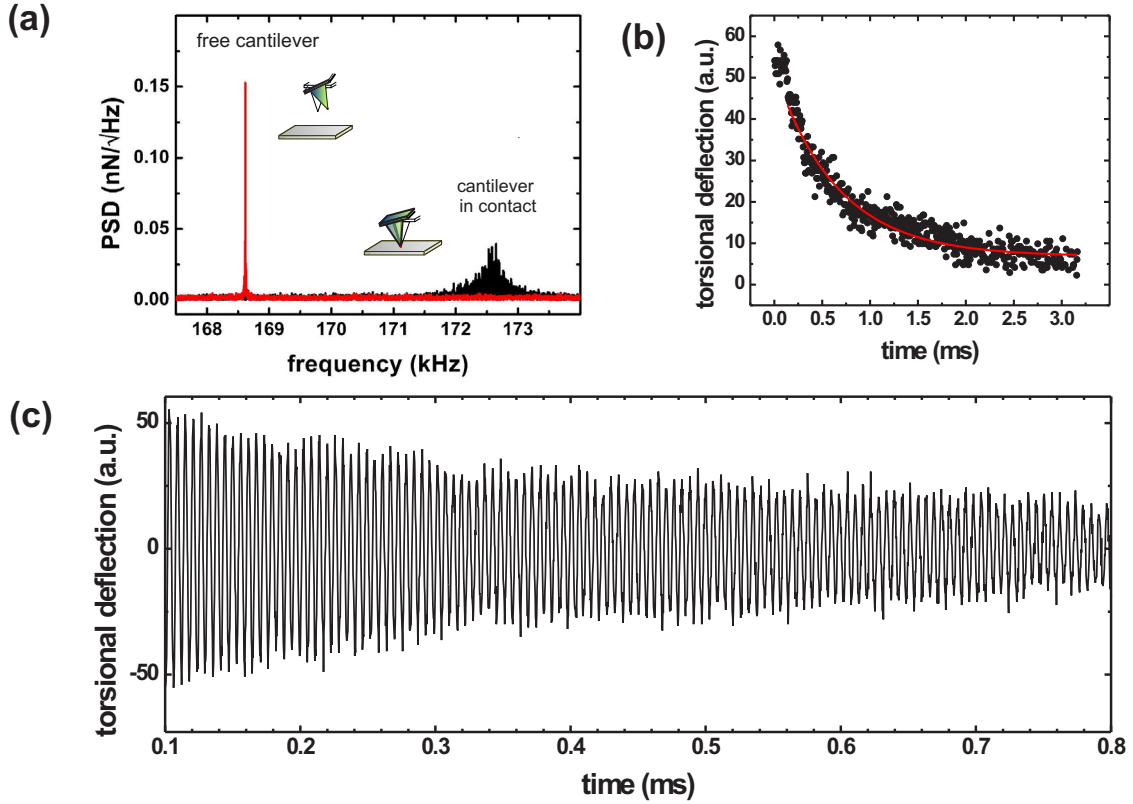


Figure 3.2: (a) Power spectral density of thermal fluctuations in the lateral force signal showing peaks corresponding to the first torsional resonance for the free cantilever (narrow peak) and for the cantilever with a sharp tip in contact with an applied normal force of -0.1 nN (wider peak). (b)-(c) Ring-down of an externally excited cantilever oscillation while the tip is in contact with a KBr sample. The decaying oscillation amplitude of the cantilever with the tip in contact is shown in (b). A quality factor of 335 was determined by a least-square fit. In (c) the decaying torsional oscillation of the cantilever is resolved.

which yield the drastic decrease of the Q -factor upon contact formation. The quality factor of the free cantilever is given by the internal friction in the beam mainly caused by thermoelastic loss and surface and bulk defects. A significant change of the shape of the cantilever deflection upon contact formation can be excluded. Consequently, the observed strong damping cannot be caused by additional internal friction in the cantilever. Rather, dissipation in the tip-sample contact causes the decrease in the quality factor of the cantilever. In order to qualitatively analyze how the damping of the tip deflection will influence the cantilever motion we calculate the quality factor of the cantilever oscillation for the two-spring model in section 3.5.

3.3. Load Dependence of the Resonance

The occurrence of stick-slip instabilities in atomic friction experiments and accordingly energy dissipation has been found to depend critically on the normal load applied to the contact [20].

Therefore it is interesting to study the change in the torsional resonance of the cantilever in contact depending on the normal load. For a standard contact lever as used in atomic friction experiments the power spectral density of the torsional signal was measured in contact with a KBr(100) surface. Upon contact formation, we observed an increase of the resonance frequency and the width of the resonance peak as shown in Fig. 3.2(a). However, once the contact between the sharp tip and surface has been established we found no clear dependence of the position of the torsional resonance peak with the load. Fig. 3.3(c) shows the frequency shift between the free cantilever far away from the surface and the lever in contact depending on variable loads up to 15 nN. The position of the resonance peak varies as much as 700 Hz even for subsequent measurements at the same load. Any distinct relation between resonance and load is hidden by these fluctuations. This result is in some contrast to findings in air by Drobek et al. [123] who reported that for a v-shaped cantilever the resonance frequency of the first torsional mode increases with higher loading forces and related the increase of frequency to an increase of the contact stiffness.

In order to elucidate whether the vacuum environment or the different tip sample interaction causes the differences between our and Drobek's findings we have recorded the thermal fluctuation spectra for spherical tips with micron-scale apex radius. Since KBr is a very soft material and the sample starts to wear off even for small loads [10, 36], the measurable loads were restricted to a narrow range. The measurements with the spherical tip were therefore performed on the hard $\text{Al}_2\text{O}_3(0001)$ surface in order to avoid plastic deformation. The surface was prepared by annealing in air as described in section 2.5. In all these experiments we waited a few minutes between the loading and unloading steps and the data acquisition in order to let the contact relax to an equilibrium position. Upon contact formation with the flat $\text{Al}_2\text{O}_3(0001)$ surface, frequency and quality factor changed in the same way as observed for the sharp tip on the KBr(100) surface, except that the frequency shift of the resonance peak between the free cantilever and the lever in contact is more than 20 kHz and therefore much larger than in the case of the sharp tip. A further increase of the frequency shift is found for higher applied loads, as seen in Fig. 3.3(a). Moreover, the width of the resonance curves decreases by increasing the load and its peak height increases. Using a harmonic oscillator analysis, this would imply that the quality factor in contact increases with increasing load. Fig. 3.3(e) indicates almost a linear dependence of the Q-factor with the load. The quality factor was calculated from the resonance frequency f and full width at the half-maximum of the resonance peak Γ : $Q = \frac{f}{\Gamma}$. These Q-factors are comparable to the values which were found in the last section for the sharp tip in contact. It is important to note that the total area below the peaks is reduced by the increasing load indicating that the contact acts as a hinge changing the shape of the deflection of the cantilever. The Q-factor in the second torsional mode seems to decrease upon loading. The height of the resonance peaks shown in Fig. 3.3(b) is decreasing while the width increases. But the signal-to-noise ratio is too low to make any further quantitative statement.

Alternatively, the contact size and contact stiffness was calculated from the measured slope of the sticking part in friction loops while scanning with the micrometer-sized spherical tip over the $\text{Al}_2\text{O}_3(0001)$ surface. A typical friction loop over a scan range of 10 nm with a scan speed of 10 nm/s and a load of 0.4 nN is shown in Fig. 3.4(a). Because the contact is larger than in atomic friction experiments, more atomic bonds break during a slip which results in higher friction force than with a sharp tip. Moreover, slips of different length are observed. The occurrence of stick-slip behavior along this small scan range let us believe that the tip moves from one equilibrium position to the next, although one might expect the tip is resting

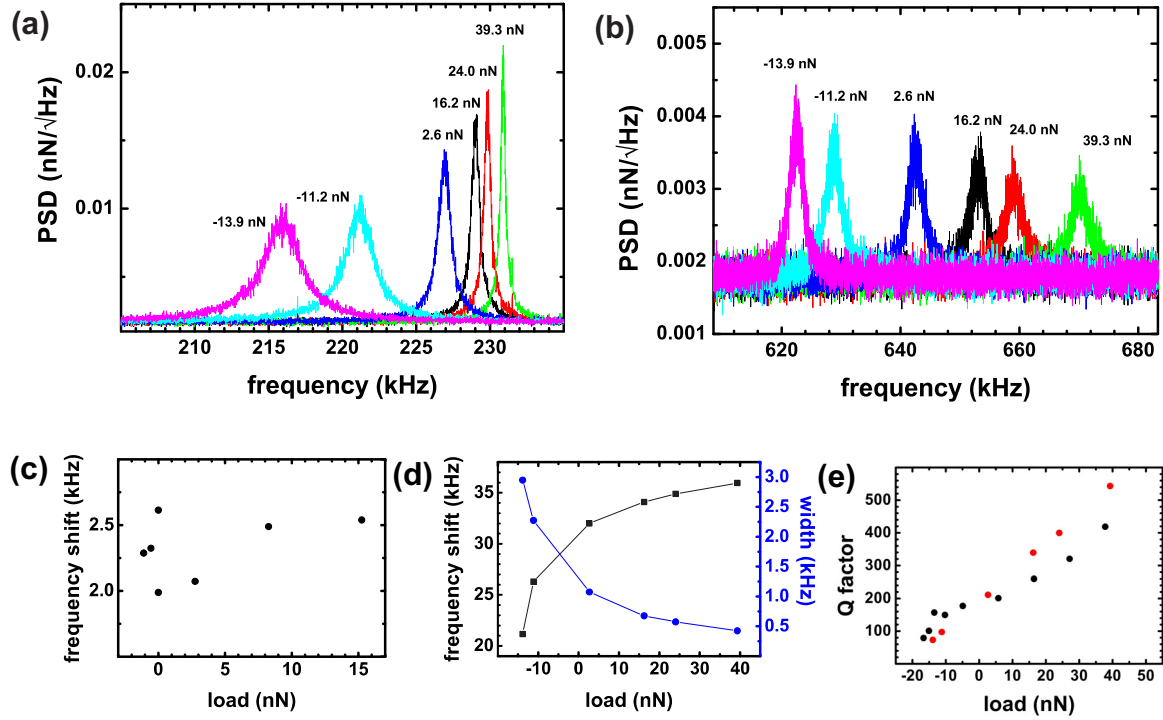


Figure 3.3: (a) Power spectral density (PSD) of the lateral force signal from a cantilever bearing a micrometer-scale spherical tip in contact with an Al_2O_3 surface for different loads. The center frequency increases monotonously with higher loads, while the width of the peaks decreases as indicated in (d). Note that the total area of the peaks is not constant. The torsional resonance frequency of the free cantilever was 195.0 kHz. (b) Simultaneously recorded second torsional mode of the cantilever in contact. (c) The frequency shift between the free cantilever and the cantilever in contact for different applied loads bearing a sharp tip in contact with a $\text{KBr}(100)$ surface. Note that no significant load dependence is found. (d) Frequency shift between the free cantilever far away from the surface and the lever in contact as well as the width for different applied loads of the resonance peaks in (a). (e) Calculated Q-factor from (d) completed with other measurements of similar type (black points).

in contact or rolling due to its large contact size. The measured sticking slope at the beginning of the friction loop corresponds to the effective spring constant which considers the spring constant of the force sensor and the compliance of tip and surface as follows

$$\frac{1}{k_{exp}} = \frac{1}{k_{con}} + \frac{1}{k_T} + \frac{1}{k_{tip}}. \quad (3.2)$$

The inset of Fig. 3.4(b) illustrates the different contributions to the effective stiffness. Lantz et al. pointed out that it is important to consider the lateral stiffness of commercial probing tips k_{tip} [129]. They found by scanning transmission electron microscopy imaging and finite element analysis a value of $k_{tip} = 84 \text{ N/m}$ for a sharp silicon tip, which is comparable to the lateral stiffness of the cantilever. In this calculations we did not consider the tip stiffness separately, because our tip has a different shape than the one described by Lantz et al. and a detailed enough high resolution SEM study of ours was not available.

The contact area between a sphere and a plane is quantified in continuum mechanics by

$$a = \frac{k_{con}}{8G^*} \quad \text{with} \quad G^* = \left(\frac{2 - \nu_1^2}{G_1} + \frac{2 - \nu_2^2}{G_2} \right)^{-1}. \quad (3.3)$$

This equation is valid for various continuum elasticity models and does not depend on the interaction forces [29, 130]. The following values for the shear moduli G_1 and G_2 of the tip and sample as well as Poisson ratio $\nu_{1,2}$ were used to calculate the effective shear modulus G^* : $G_{KBr} = 1.0 \cdot 10^{10}$ N/m², $G_{Si} = 6.8 \cdot 10^{10}$ N/m², $\nu_{KBr} = 0.25$ and $\nu_{Si} = 0.22$ [90]. The calculated contact stiffness and area for the experiment with the spherical tip upon contact with a flat Al₂O₃(0001) surface are shown in Fig. 3.4 (b). The contact stiffness is found to change between 16 N/m and 61 N/m by varying the load from -8 nN to 56 nN. This corresponds to a change in the contact radius of 0.4 nm to 1.67 nm. For small loads, contact radii of the order of atomic dimensions are found, which is at the limit of continuum elasticity theory. A contact radius of 1.67 nm means that more than 200 atoms are involved in a contact. The stiffness of the contact itself and hence the radius would be larger if the stiffness of the tip could be considered independently. These measurements suggest that the lateral contact stiffness k_{con} for high loads becomes equal to the cantilever stiffness k_T . In their experiments on CdTe Drobek et al. measured a contact radius of 3.8 nm [123]. For that reason, the spherical tip measurements on Al₂O₃ are more comparable to their findings than the one obtained with the sharp tip in contact with KBr, where we expect the contact radius to be in the order of a few angstroms, which corresponds to only a few atoms. In conclusion, both the power spectral density measurements and the friction loop measurements using the spherical tip indicate an increase of the contact stiffness with increasing load.

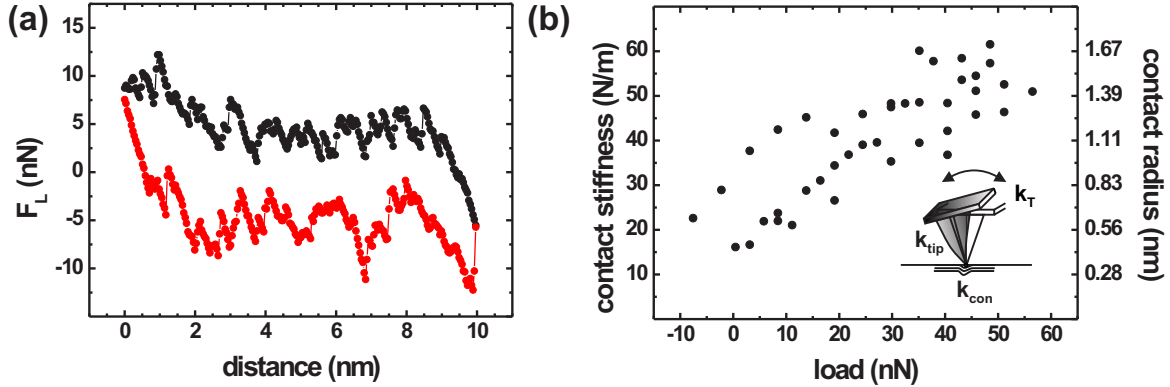


Figure 3.4: (a) Friction loop of a micrometer-sized spherical silicon tip scanning in contact with a flat Al₂O₃(0001) surface. The applied load was 0.4 nN. (b) Contact stiffness and contact radius calculated from the measured slope of the sticking part in the friction loop for different loads. The inset illustrates the different contributions to the effective stiffness.

In comparison to the very hard Al₂O₃(0001), the load dependence of the torsional resonance bearing the micrometer-sized spherical tip in contact was studied on a very soft material as Cu(100). In this case, we observe a discrepancy in the frequency vs. load curves upon loading and unloading, as shown in Fig. 3.5(a). This hysteresis behavior is arising from the fact that

plastic deformation occurs which results in a significant change in the contact area. Concerning the width at half-maximum of the resonance peak, a similar behavior compared to $\text{Al}_2\text{O}_3(0001)$ is observed: The peaks of the first torsional mode become narrower with increasing load. Fig. 3.5 suggests a linear decrease of width at half-maximum of the resonance peak with the resonance frequency. Hence, assuming a harmonic oscillation, the Q-factor increases for higher resonance frequencies, in agreement with the measurements on Al_2O_3 .

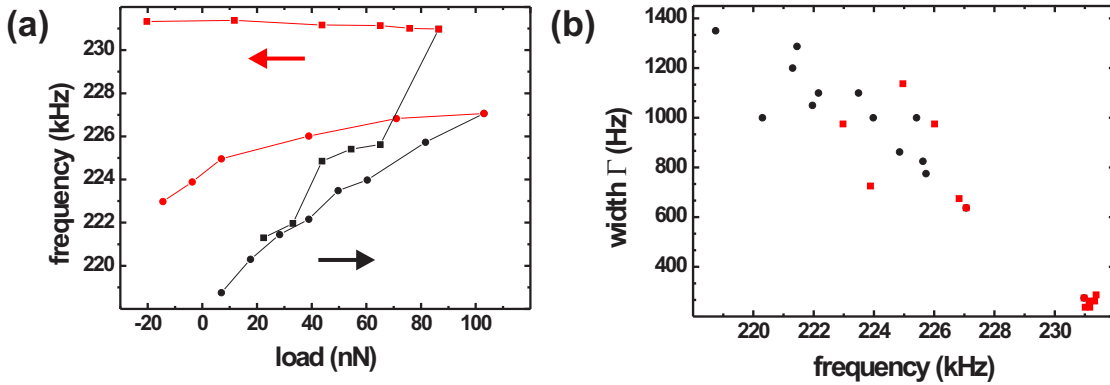


Figure 3.5: (a) The frequency shift between the free cantilever and the cantilever in contact for different applied loads bearing a sharp tip in contact with a $\text{Cu}(100)$ surface. Different measurements are represented by different symbols. The uploading part is plotted in black and the unloading part in red. The discrepancy in the frequency vs. load curve upon loading and unloading suggests a plastic deformation of the sample. (b) Full width at half-maximum of the measured resonances peaks.

In summary, a further frequency shift with increasing load on the contact is found for micrometer-sized spherical tips, while for the sharp tips used in atomic friction experiments, no clear tendency of the frequency shift is observed, only fluctuations of the peak position of about 700 Hz even for measurements at the same load. Following the point-mass model or the model of Drobek et al. [123] and taking the frequency shift as a measure for the contact stiffness, we find that the contact stiffness for very sharp tips is not load dependent but shows smaller variations as a function of time. This is in agreement with prior analysis of the load dependence of the contact stiffness from atomic friction data [20]. In a continuum mechanics approach we expect the lateral stiffness to increase with load proportional to the contact area as described in Eq. (3.3) and shown in Fig. 3.4. The breakdown of continuum models at the nanometer scale for the contact stiffness has recently been discussed by Luan and Robbins, who found that their applicability depends on the atomic structure of the tip apex [30]. Tips which have a spherical shape even on nanometer scale are well described by continuum models, while tips with a stepped atomic structure exhibit discontinuities in the contact area with increasing load. We find apex clusters with a stepped structure a more probable tip model and conclude from our results that for very sharp tips and low loads the contact size and the contact stiffness do not vary as a function of load. The unsystematic changes of the contact stiffness are related to changes of the contact geometry, due to uncontrolled processes such as

diffusion or drift. For larger spherical tips and higher loads, our data in Fig. 3.3 and Fig. 3.4 confirm the established relations between load, contact size, contact stiffness, and shift in the torsional resonance frequency.

The frequency spectra of the lateral force signal were also studied while scanning over the surface. In the case of the sharp tip on the KBr(100) surface, the frequency spectrum does not change significantly. The only additional features appearing in the spectrum are peaks at low frequencies caused by the periodically occurring stick-slip instabilities in the saw-tooth shaped friction signal, and their higher modes. In the case of the micrometer-sized tip in contact with $\text{Al}_2\text{O}_3(0001)$ surface, the height difference between the low and high loading is less pronounced. But a similar dependency in frequency shift and Q-factor is observed upon loading and unloading.

3.4. Calculation of the Torsional Resonance Frequency of the Cantilever in Contact

The increase of the torsional resonance frequency of the cantilever upon contact formation is explained by the additional stiffness caused by the fixation of the tip apex. In this section different theoretical methods to calculate the frequency shift upon contact formation are discussed and compared with the experimental results of the previous section. Fig. 3.6 illustrates the used point-mass model and beam equation model.

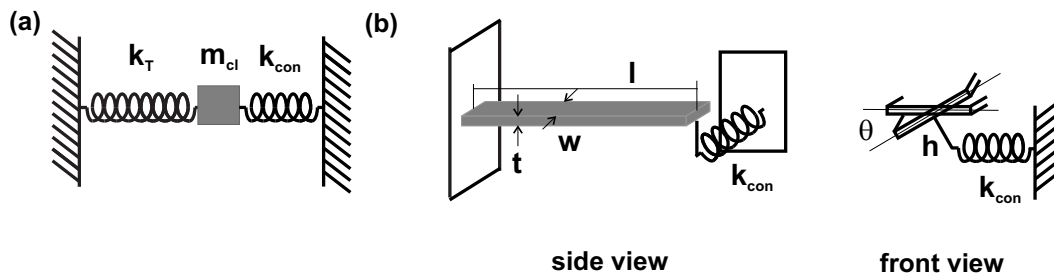


Figure 3.6: Scheme of the point-mass model in (a) and beam equation in (b). In this section the torsional resonance frequency of the cantilever in contact is calculated for both models .

3.4.1 Point-Mass Model

A simple first approach to model the torsional resonance of a cantilever with its tip in contact with a sample is the point-mass model. The effective mass of cantilever and tip is considered as a point-mass connected by a spring, which represents the massless cantilever, to a fixed support. Thus, the resonance frequency of the torsional mode of the free cantilever is given by

$$f_T^{free} = \frac{1}{2\pi} \sqrt{\frac{k_T}{m_{cl}}}, \quad (3.4)$$

where k_T is the spring constant for torsional bending and m_{cl} is an effective mass of the cantilever. The ratio of the effective mass of the cantilever and its real mass depends on the

width of the beam and on the length of the tip [131]. Bringing the tip into contact, the contact stiffness k_{con} adds to the spring constant resulting in

$$f_T^{con} = \frac{1}{2\pi} \sqrt{\frac{k_T + k_{con}}{m_{cl}}}. \quad (3.5)$$

The contact stiffness, a combination of the tip stiffness and the curvature of the surface potential, can be calculated from the slope of the force curve k_{exp} assuming the cantilever and the contact act as springs in series according to Eq. (3.2). Combining Eqs. (3.5) and (3.2), the point-mass spring model predicts

$$f_T^{con} = f_T^{free} \sqrt{1 + \frac{1}{\frac{k_T}{k_{exp}} - 1}}. \quad (3.6)$$

With such a point-mass model only the frequency of the fundamental mode is obtained. By solving a beam equation, which includes a mass distribution, also higher modes are obtained.

3.4.2 Beam Equation

In this section the rectangular cantilever is considered as a beam with length L , width w , and thickness t . The beam is made of a material with mass density ρ and a shear modulus G . The beam is subject to a time-dependent torque per unit length arising from the lateral forces between sample and tip, which causes a twist of the lever. The torsional angle $\theta(x, t)$ is a function of length x and time t . The equation of motion is a second order differential equation and is therefore easier to solve than the one for the normal bending, which is fourth order

$$\frac{\partial^2 \theta}{\partial x^2} = \frac{\rho J}{C} \frac{\partial^2 \theta}{\partial t^2}. \quad (3.7)$$

The torsional stiffness C is

$$C = \frac{w \cdot t^3}{3} \cdot G,$$

where G is the shear modulus of the cantilever. The cross section of the cantilever is rectangular, therefore the polar moment of inertia can be calculated as follows:

$$J = 4 \cdot \int_0^{w/2} \int_0^{t/2} (z^2 + y^2) dy dz = \frac{1}{12} (w^3 t + t^3 w).$$

In our model the cantilever is fixed at one end and at the other end connected with a spring to the surface. This leads to the following two boundary conditions

$$\theta(0, t) = 0 \quad \text{and} \quad \frac{\partial \theta(L)}{\partial x} = -\frac{k_{con} h^2}{C} \theta. \quad (3.8)$$

In the second boundary condition, it was assumed that the lateral displacement of the beam end is small compared to the tip height h , which results in acting the lateral force of $F_{lat} = -k_{con} h \theta$. A more appropriate model describing the tip in contact with a sample would need to include a damping term parallel to the spring term. The equation of motion (3.7) can be solved by the ansatz

$$\theta(x, t) = X(x) \cdot T(t), \quad (3.9)$$

where variables are separated. Substituting Eq. (3.9) into Eq. (3.7) and rearranging leads to

$$\frac{1}{X(x)} \frac{\partial^2 X}{\partial x^2} = \frac{\rho J}{C} \frac{1}{T(t)} \frac{d^2 T}{dt^2}. \quad (3.10)$$

This equation can be separated into spatial and temporal components as following

$$\frac{\partial^2 T}{\partial t^2} + \frac{C\lambda}{\rho J} T = 0 \quad \text{and} \quad \frac{\partial^2 X}{\partial x^2} + \lambda X = 0, \quad (3.11)$$

where λ represents the separation constant. The solution of these two equations are

$$T(t) = A \cos\left(\sqrt{\frac{\lambda C}{\rho J}} t\right) + B \sin\left(\sqrt{\frac{\lambda C}{\rho J}} t\right) \quad (3.12)$$

$$X(x) = E \cos(\sqrt{\lambda} x) + F \sin(\sqrt{\lambda} x), \quad (3.13)$$

with integration constants A , B , E and F . Using the first boundary condition in Eq. (3.8) we find $E = 0$ so that

$$X(x) = F \sin(\sqrt{\lambda} x). \quad (3.14)$$

The second boundary condition in Eq. (3.8) leads to the transcendental equation

$$\frac{C\sqrt{\lambda}}{h^2 k_{con}} = \tan(\sqrt{\lambda} L). \quad (3.15)$$

The solutions of this equation for λ determines the torsional contact resonance frequencies of the first and its higher eigenmodes

$$f_T^{con} = \frac{1}{2\pi} \sqrt{\frac{\lambda C}{\rho J}}. \quad (3.16)$$

which depend on the contact stiffness k_{con} . From the orthogonalization and normalization of the eigenfunctions we could obtain an expression for the integration constants A , B and F and therefore the shape of the different modes. Using different boundary conditions Eq. (3.7) was also used to describe the torsional resonance of the cantilever in contact in ultrasonic friction force microscopy [131–133]. In the following section we calculate the frequencies of the lever in contact f_T^{con} in dependence of k_{con} for the geometry of the spherical tip and compare them to the measured frequencies.

3.4.3 Comparison between the Two Models

In this section the point-mass model and the beam equation model are compared with respect to the measurements presented in the previous two sections. Fig. 3.7 compares the frequency shift upon contact formation obtained with these two models using Eqs. (3.6) and (3.16). The input parameters for the geometry of the cantilever with the spherical tip are listed on page 23. The thickness of the cantilever was adjusted so that the resonance frequency of the free cantilever matches to the measured one. An incorrect frequency shift of the fundamental mode is obtained from the point-mass model, as soon as the contact stiffness is of the order of the cantilever spring constant. For low loads in the order of a few nanonewtons a frequency shift of around 20 kHz and a contact stiffness of 15 N/m was measured. This is in good agreement with the result of the beam equation, which confirms a value of 20.5 kHz for a contact stiffness of 14 N/m. For higher contact stiffnesses, the calculated frequencies are higher than

the measured ones. Such a discrepancy may be caused by the fact that the contact may act as a hinge and change the cantilever deflection, as can be inferred from the changing area under the resonance curves in Fig. 3.3(a). Moreover, one has to keep in mind that the spring is attached to the end of the cantilever, but in reality the tip does not sit right at the end of the lever.

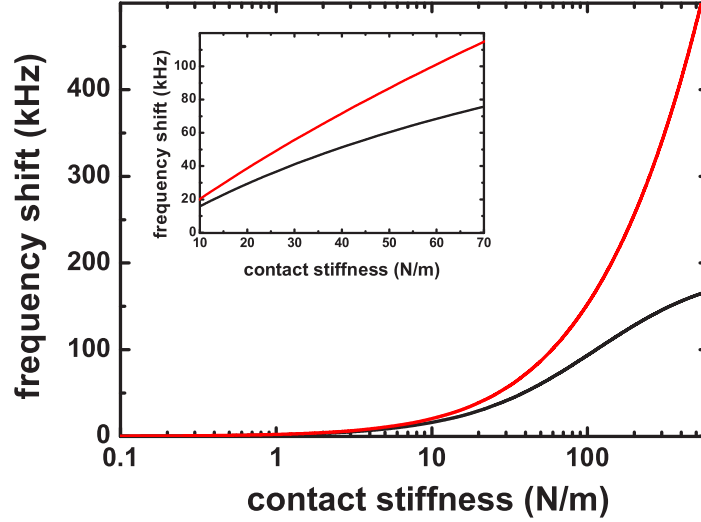


Figure 3.7: Calculated frequency shift for the spherical tip upon contact formation using the point-mass model (red) respectively the beam equation (black). The parameters for these simulations are in accordance with the experimentally found determined for the cantilever with the spherical tip: $w = 45 \mu\text{m}$, $L = 453 \mu\text{m}$, $t = 1.47 \mu\text{m}$, $G_{Si} = 0.68 \cdot 10^{11} \text{ N/m}^2$, $\rho_{Si} = 2328.3 \text{ kg/m}^3$. The inset is a zoom to the range of contact stiffnesses comparable to the experiment.

For the sharp tip used in Fig. 3.2(a) with a measured slope of $k_{exp} = 2.23 \pm 0.05 \text{ N/m}$ (compare Fig. 4.2) we expect $f_T^{con} = 171.75 \pm 0.08 \text{ kHz}$ according the point-mass model Eq. (3.6), which is a little less than the actual measure value of 172.5 kHz . From the beam equation we obtain a resonance frequency of 170.60 kHz for the cantilever in contact. The thickness of the cantilever was chosen so that the resonance of the free cantilever matches the measurement. The discrepancy can easily be caused by the error in the determination of k_T , which depends critically on the precise measurement of the actual height of the tip. Another explanation for the discrepancy could be a change of the effective mass m_{cl} if the shape of the cantilever deflection is modified by the contact formation. However, considering the small relation between contact stiffness k_{con} and cantilever stiffness k_T and the small thermal oscillation amplitude of about one tenth of an atomic diameter at the tip apex, a significant change of the deflection mode can be excluded. In summary, for rectangular cantilevers and a small contact stiffness in the order of a few N/m the point-mass harmonic oscillator model can describe the frequency shift reasonably well, while for the spherical tip a beam equation should be used.

3.5. Calculation of the Quality Factor in Contact

Upon contact formation, we do not only observe a shift of the resonance frequency but also a drastic increase of the width of the resonance peak, corresponding to a drop in the quality factor by nearly three orders of magnitude. In the discussion of this experiment it was concluded that the observed strong damping cannot be caused by additional internal friction in the cantilever. Rather, dissipation in the tip-sample contact was expected to cause the decrease in the quality factor of the cantilever. In order to analyze how damping of the tip deflection will influence the cantilever motion we calculate the quality factor of the cantilever oscillation for a two-spring model. One spring represents the cantilever and the other the tip-sample contact. The tip motion is described by Newton's equation

$$m_{tip}\ddot{x}_{tip} = -k_{tip}(x_{tip} - x_{cl}) - m_{tip}\gamma_{tip}\dot{x}_{tip}, \quad (3.17)$$

where x_{tip} and x_{cl} are the respective deflections of tip and cantilever, γ_{tip} is a damping coefficient for the tip movement and m_{tip} the mass of the tip and contact. We neglect the internal friction of the cantilever since we know that dissipation due to the tip motion dominates. Assuming for this derivation that the cantilever oscillates with $x_{cl} = A_{cl} \sin(\omega_{cl}t)$, with $\omega_{cl} = \sqrt{k_T/m_{cl}}$, the equation of motion Eq. (3.17) becomes

$$\ddot{x}_{tip} + \gamma_{tip}\dot{x}_{tip} + \omega_{tip}^2 x = \frac{k_{tip}A_{cl}}{m_{tip}} \sin(\omega_{cl}t). \quad (3.18)$$

The time-averaged power loss in this driven, weakly damped oscillation of the tip is given as

$$\bar{P} = \frac{k_{tip}^2 A_{cl}^2 \gamma_{tip}}{2m_{tip}} \frac{\omega_{cl}^2}{(\omega_{tip}^2 - \omega_{cl}^2)^2 + \omega_{cl}^2 \gamma_{tip}^2}. \quad (3.19)$$

This dissipation in the tip movement will damp the cantilever oscillation. The quality factor Q_{con} of the cantilever is defined as the relation between the total energy of its oscillation and the power loss per oscillation cycle:

$$Q_{con} = 2\pi \frac{E}{\Delta E} = 2\pi \frac{\frac{1}{2}k_T A_{cl}^2}{2\pi \frac{\bar{P}}{\omega_{cl}}} = \frac{1}{2} \frac{k_T A_{cl}^2 \omega_{cl}}{\bar{P}}. \quad (3.20)$$

Combining Eqs. (3.20) and (3.19) and introducing the critical damping $\gamma_c = 2\omega_{tip}$ for the tip movement we obtain

$$Q_{con} = \frac{1}{2} \left(\frac{m_{tip}}{m_{cl}} \right)^{\frac{1}{2}} \left(\frac{k_T}{k_{tip}} \right)^{\frac{3}{2}} \left(\frac{\gamma_c}{\gamma_{tip}} \right) \left[\left(\frac{\omega_{tip}}{\omega_{cl}} - \frac{\omega_{cl}}{\omega_{tip}} \right)^2 + 4 \frac{\gamma_{tip}^2}{\gamma_c^2} \right]. \quad (3.21)$$

For the following parameters $m_{cl} = 5.5 \cdot 10^{-11}$ kg, $m_{tip} = 1 \cdot 10^{-12}$ kg, $k_T = 62$ N/m, $k_{tip} = 3.5$ N/m, $\omega_{tip} = \sqrt{k_{tip}/m_{tip}}$, and $\gamma_{tip} = \gamma_c$ one obtains $Q_{con} \sim 30$, the same order of magnitude as the result for a resonance analysis of the simulated lateral force data. These parameters will be discussed in detail in the stick-slip simulations explained in section 4.4. For $m_{tip} \ll m_{cl}$ we have $\omega_{tip} \gg \omega_{cl}$ and the expression simplifies into

$$Q_{con} = \frac{1}{2} \left(\frac{m_{cl}}{m_{tip}} \right)^{\frac{1}{2}} \left(\frac{k_T}{k_{tip}} \right)^{\frac{1}{2}} \left(\frac{\gamma_c}{\gamma_{tip}} \right). \quad (3.22)$$

As one would expect, the quality factor Q_{con} of the cantilever is lowered by the effective mass m_{tip} of the tip, the coupling k_{tip} between cantilever and tip, and by the damping γ_{tip} of the tip

movement. In order to reach a quality factor of the order of 600 as found in the experiment, one would have to assume a hundred times smaller tip mass or a strong underdamped tip movement. No signatures of the latter has been observed in experiments. On the other hand, an effective tip mass of only $m_{tip} = 10^{-14}$ kg would make sense as it corresponds to a volume of $1 \mu\text{m}^3$. In comparison, a very rough approximation for the mass of the microscopical tip calculated from the geometrical dimensions obtained from a SEM image assuming a pyramid with a triangular base results in $m_{tip} \approx 5 \times 10^{-13}$ kg. Exactly this value was used by Dupas in his model to describe the normal oscillation modes of a cantilever in contact [128]. Reimann and Evstigneev have come to a similar conclusion in their analysis of friction force microscopy focusing onto the tip deflection and suggested for the effective mass $m \leq 3 \times 10^{-12}$ kg [42].

The increase of the quality factor with increasing load observed for the micrometer-sized contact and higher loads on $\text{Al}_2\text{O}_3(0001)$ and $\text{Cu}(100)$ cannot be explained in a simple two-spring model. The lateral contact stiffness becomes comparable to the torsional stiffness of the cantilever. Consequently, the contact can act as a hinge and change the shape of the cantilever deflection, as can be inferred from the changing area under the resonance curves in Fig. 3.3(a). More complex models including the finite volume of the beam and internal friction following stress distributions will be necessary to predict the quality factor in these cases. In a simple picture one can assume that the additional fixation of the tip, which leads to a higher stiffness, reduces the amount of degrees of freedom in the tip movement and consequently also the amount of possible dissipation channels.

3.6. Conclusions

Thermal fluctuations of the cantilever have a strong impact on the atomic-scale stick-slip process in friction. In this chapter such fluctuations have been studied in detail using a home-built force microscope in ultrahigh vacuum allowing for high bandwidth detection of the lateral and normal force signal. It was found that the thermal fluctuations are strongly damped through the tip-sample contact. Using the frequency shift of the resonance upon contact formation as a measure for the contact stiffness, a power spectrum analysis has suggested that the contact stiffness remains constant for the sharp tip and only changes for micrometer-sized spherical tips with changing loads. This finding was confirmed by measurements of friction loops. This suggests a breakdown of continuum models at the nanometer scale for the contact stiffness as recently discussed by Luan and Robbins, who found that their applicability depends on the atomic structure of the tip apex [30]. Tips that maintain a spherical shape even on the nanometer scale are well described by continuum models, while tips with a stepped atomic structure exhibit discontinuities in the contact area with increasing load. We find apex clusters with a stepped structure a more probable tip model and conclude from our results that for very sharp tips and low loads the contact size and the contact stiffness do not vary as a function of load. Modeling the experiment by a two-spring model, one representing the cantilever force sensor and one the compliant tip-sample contact, a consistent description of the lateral contact stiffness and the quality factor in lateral force measurements has been achieved.

Time Resolved Atomic-Scale Stick-Slip Measurements

4.1. Introduction

Already the first report on friction force microscopy by Mate et al. describes a stick-slip movement of the tip with the atomic periodicity of the sample's surface structure [6]. This atomic stick-slip process has attracted a lot of attention since it can be seen as an elementary mechanism of friction. The tip is locked to one atomic position on the surface until the increasing lateral force is strong enough to initiate a sudden jump to the next position. The occurrence of the stick-slip behavior is one-to-one related to energy loss in the sliding process [20]. When reducing the normal load on the contact, the tip starts to slide continuously over the surface potential and friction is reduced essentially to zero. Only with increased normal load do stick-slip instabilities arise and cause energy dissipation. Other recent results include the understanding of the role of thermal activation for the velocity dependence of atomic friction [12, 26, 41, 42]. It was found that, thermal fluctuations reduces friction at elevated temperatures, and at slow sliding velocities.

All these results indicate the key role of the slip instability for the dissipation of mechanical energy into heat. However, the duration of the slip events have never been investigated experimentally. This chapter describes the results of experiments and simulations which address in detail the dynamics of the atomic-scale slip by means of high bandwidth atomic friction force microscopy. By analyzing the duration of a slip we could distinguish between a single and multiple contact. The experimental results are compared with a multi-tip simulation based on a one-dimensional Tomlinson model including thermal activation.

4.2. Atomic-Scale Stick-Slip on KBr(100)

The lateral force map for the perfect one-atom contact on a KBr(100) surface consists of a regular array of diamonds, their corners touching each other. The size of the unit cell corresponds to the spacing between equally charged ions. Such a pattern can be reproduced by a two-dimensional Tomlinson model, as reported by Lüthi et al. [35]. In the Tomlinson model the tip is considered to move over a periodic potential given by the atomic lattice, while being dragged along the surface by an external spring as explained in detail in section 1.2.1. Fig. 4.1(d) comes very close to a regular pattern of diamonds and also reveals perfect stick-slip curves as shown in Fig 4.2. Unfortunately, irregular tip structures and drift can cause irregularities in the stick-slip pattern. Examples of lateral force maps recorded on KBr(100) surfaces

showing such irregularities are presented in Fig. 4.1(a)-(c). It is important to note that these images do not represent true atomic resolution of a KBr surface, since all the unit cells are the same and no defects were observed suggesting that the atomic contrast in contact mode is a convolution of the tip and surface structure. The interaction of the different atoms at the tip apex with the perfectly symmetric surface atoms results in a distorted shape of each unit cell. In order to compare experimental data to a one-spring Tomlinson model we took data from frames that come as close to the expected diamond pattern as possible. In this chapter we will extend the Tomlinson model to a multiple-tip model which allows us to describe lateral force maps of not so perfect stick-slip measurements arising from multiple contacts.

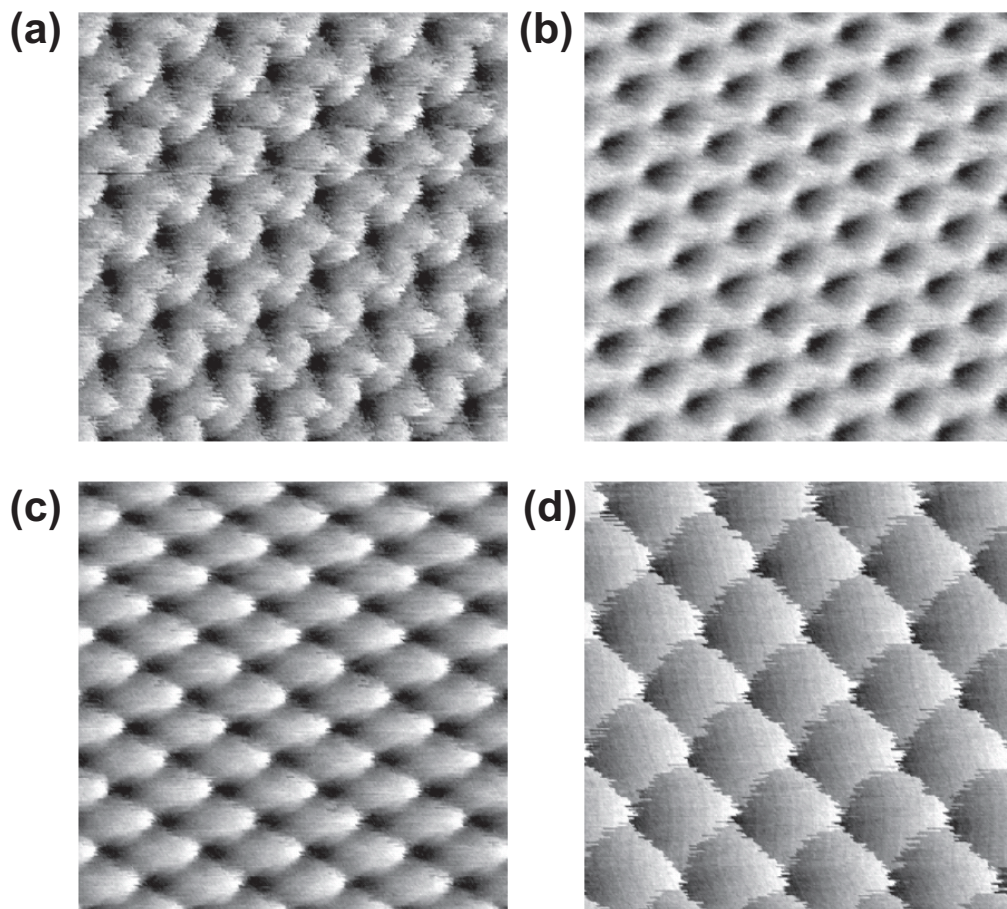


Figure 4.1: Experimental lateral force maps recorded on KBr(100) surfaces. The cubic symmetry of the surface is distorted due to instrumental drift. The atomic patterns in images (a)-(c) show significant deviation from the diamond-like pattern expected from the two-dimensional Tomlinson model for a single asperity. In contrast, (d) resembles the expected pattern rather closely. The scan range in all the images is $3 \text{ nm} \times 3 \text{ nm}$. Applied loads: (a) -0.4 nN , (b) -0.1 nN , (c) -0.4 nN and (d) -0.1 nN .

It would be very helpful to reconstruct the atomic structure of the tip apex from images shown in Fig. 4.1. Algorithms have been suggested for the deconvolution of scanning probe microscopy images for obtaining the shape of the tip [134]. For atomic scale imaging these approaches are hampered by the fact that the tip apex atoms have distances that may vary around the length of one surface unit cell. Therefore, a unique reconstruction from the repeated pattern is not possible. Recently, Giessibl and Hembacher et al. report on distinct substructures in images of individual adatoms on silicon (111) and graphite and interpreted these observations as images of atomic orbitals of the front atom of the tip in non-contact atomic force microscopy [135, 136]. However, additional evidence is necessary to distinguish multi-tip effects from structures that might be found on length scales below the surface unit cell. Wyder et al. discussed the effect of different tip shapes on atomic stick-slip curves on KBr using atomistic simulations [137, 138]. In the following sections, we will discuss how the slip duration provides information on the shape of the contact.

4.3. Determination of Slip Duration

Figure 4.2(a) shows a typical friction loop, where the lateral force for a single scan line in forward and backward directions is measured. All stick-slip friction loops in this section were recorded on a KBr(100) surface along the [001]-direction when the tip was moving through the center of the apparent unit cells, i.e. along lines of maximal modulation of the lateral force. The sawtooth-shaped signal consists of sticking phases where the lateral force is built up in an almost linear way, and slip events where the tip jumps from one atomic position to the next. The slope of the sticking part, k_{exp} , reflects the effective lateral stiffness of the force sensor and the contact. Here, we find $k_{exp} = 2.23 \pm 0.05$ N/m. The data for this figure was acquired with a commercial data acquisition setup (SCALA, OMICRON Nanotechnology). The sampling rate of data points recorded (1250 Hz at scan velocity of 15 nm/s) is not high enough either to detect thermal fluctuations in the force signal or to measure the duration of each slip. Therefore, we simultaneously acquired the lateral force signal with a sampling frequency of 3.3 MHz, the bandwidth of our force detection. The actual stick-slip structure can be made out in a wide band of noise, composed of both thermal fluctuations of the cantilever and electronic noise, see Fig. 4.2(c). In order to analyze the slip duration we have averaged the force data over 50 points so that the stick-slip characteristics can be clearly recognized, reducing the bandwidth of the results to 66 kHz or to a time resolution of 15 μ s. A typical scan line with this temporal resolution in forward direction is shown in Fig. 4.2(b). The following tilted step function was used to perform a least-square fit to the averaged friction force signal in order to determine the slip duration

$$f(x) = \begin{cases} k_{exp}x + b_1 & x \leq t_1 \\ \frac{k_{exp}(t_1-t_2)+b_1-b_2}{t_1-t_2}x - \frac{k_{exp}(t_1-t_2)+b_1-b_2}{t_1-t_2}t_1 + k_{exp}t_1 + b_1 & t_1 < x < t_2 \\ k_{exp}x + b_2 & x \geq t_2 \end{cases}, \quad (4.1)$$

where t_1 and t_2 describe start and end time of the slip and therefore their difference gives the slip duration. b_1 and b_2 correspond to the F_L -axis intercept of a straight line during the stick-phase and their difference is related to the jump height.

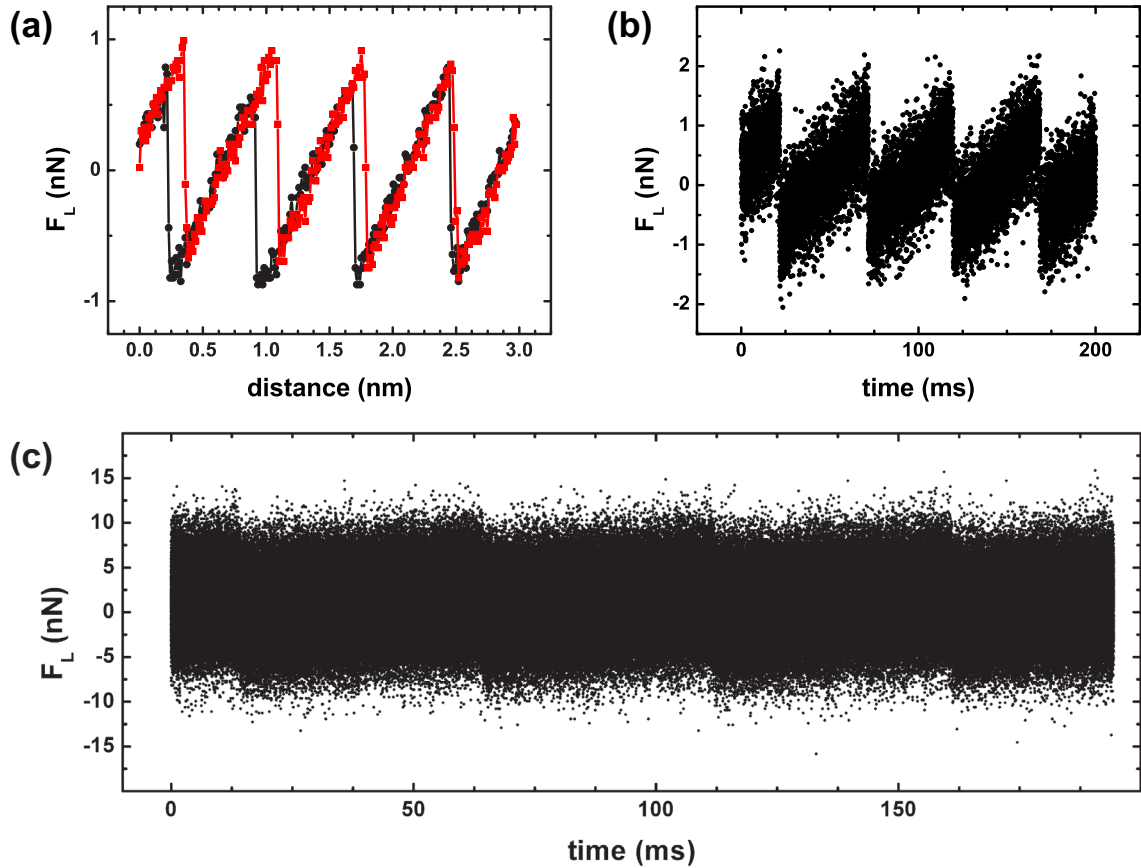


Figure 4.2: (a) Friction force loop recorded as part of a typical scan frame on a KBr(100) crystal along the [001]-direction. The time resolution is typical for commercially available data acquisition setups. The cantilever in this experiment is the same as the one used to produce the data for Fig. 3.2(a). (b) High temporal resolution scan line simultaneously acquired with the forward scan data (square symbol in (a)) at a sampling frequency of 3.3 MHz, subsequently averaged over 50 points in order to clearly reveal the shape of the stick-slip pattern. (c) High temporal resolution scan line of (b) without any averaging.

Fig. 4.3 shows four slips recorded with this high bandwidth. Compared to the typical friction loop presented in Fig. 1.6 all the stick-slip curves are mirrored against the F_L -axis. Since we are interested in the dynamics of single slips this does not influence the result of this chapter in any way. The same instrumental parameters were used for these measurements: normal load $F_N = -0.1$ nN and scan velocity $v = 25$ nm/s. For the slip in 4.3(a) we measure a slip duration of $t \approx 8.2$ ms, and $t < 15$ μ s for the one in 4.3(b). The duration of the second slip is below the limit of time resolution and is almost certainly even shorter than 15 μ s. As a first conclusion we find that the slip process in atomic friction can happen on very different time scales for similar experimental conditions. Figures 4.3(c) and (d) give examples of slip events which suggest possible mechanisms for the prolonged slip duration. In Fig. 4.3(c) the tip jumps forth and back between two atomic positions before finally settling at the new position. In Fig. 4.3(d) the tip jumps into an intermediate position before the jump over a full lattice constant is finished.

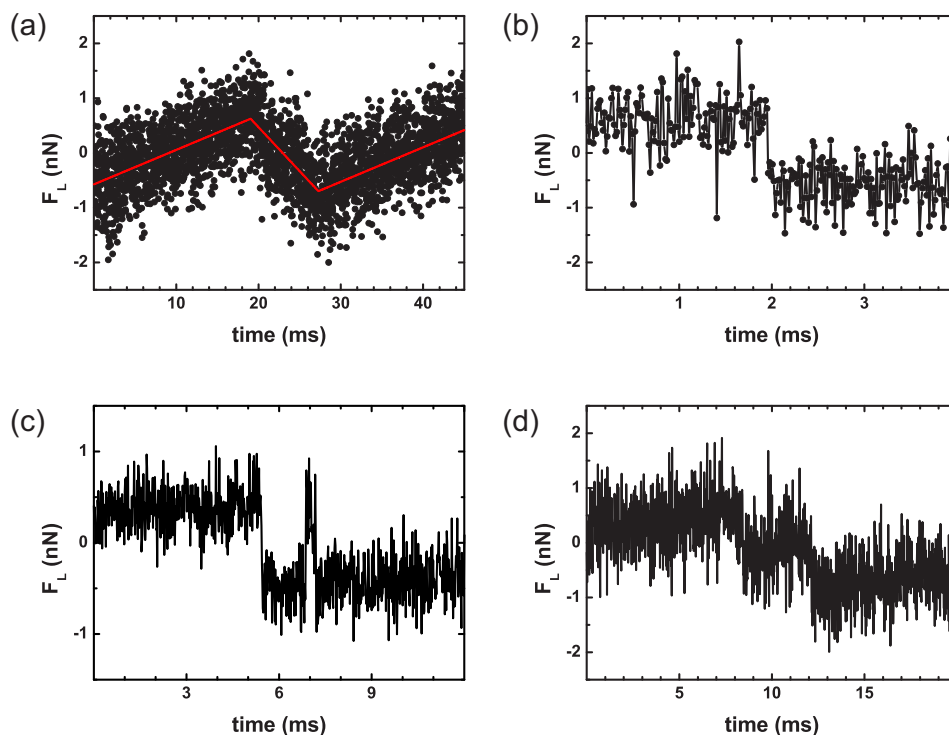


Figure 4.3: Lateral force vs. time acquired on KBr(100) with a sampling frequency of 3.3 MHz and subsequently averaged over 50 data points. The same scan parameters were used for these four measurements of atomic stick-slip: normal force $F_N = -0.1$ nN and scan velocity $v = 25$ nm/s. The slip duration was determined to be (a) $t \approx 8.2$ ms and (b) $t < 15$ μ s. (c) In the process of slipping to the next atomic position, the tip jumps forth and back between the new and the old position. (d) During the slip, the tip assumes an intermediate position.

An overview of the distribution of slip durations for several tips which range from some microseconds up to several milliseconds is given in Fig. 4.4. Corresponding lateral force maps are included in order to reveal possible correlations between the features of such maps and the duration of slip events. Lateral force maps corresponding to fast slips appear as a pattern of flat tilted diamonds with the size of one unit cell of the KBr(100) surface. In contrast, maps associated with slower slips show features on a scale smaller than the unit cell. Such features could arise from an irregular structure of the tip as already discussed in the beginning of this chapter. Several atoms of the tip might be in contact with different unit cells of the surface, having a distance between the contact points that is not commensurable with the KBr(100) surface structure. The bar for shortest slip-duration includes slips with a scan speeds in the range from 9 nm/s up to 100 nm/s indicating that fast slips occur for several scan speeds.

In chapter 3 it was found that the quality factor Q for the cantilever torsion is of the order of 600. With such a quality factor one may expect to observe a ring-down of the oscillation after fast slip events. The excitation of such oscillations by each slip event has been reported for an uncalibrated atomic friction experiment on graphite [139]. The cited experiment is difficult to compare to these results since the magnitude of forces is unknown and the experimental method included band-pass filtering around the expected torsional resonance. In both our experimental and simulation results we do not observe any excitation of cantilever oscillations

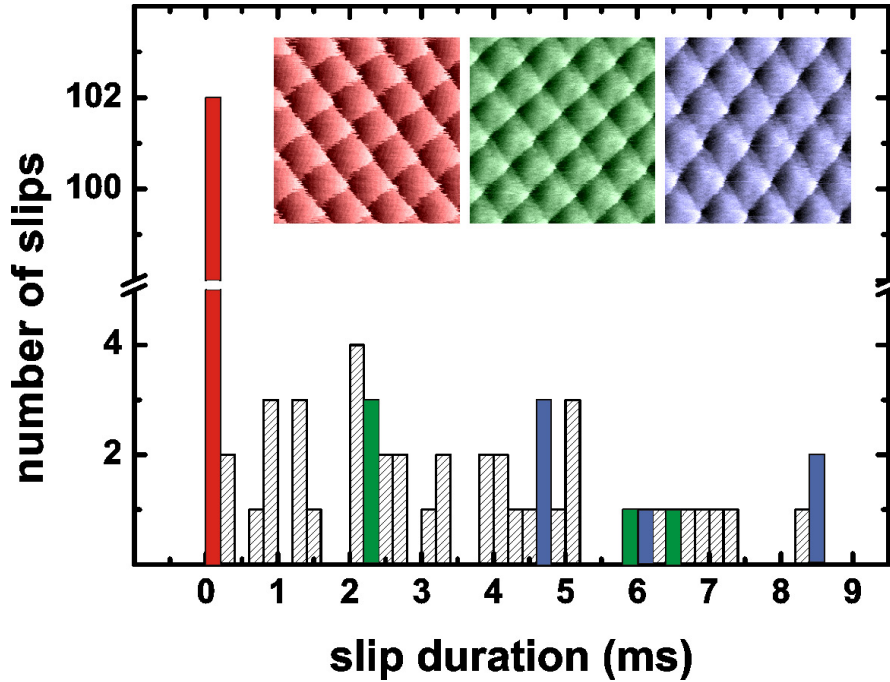


Figure 4.4: Distribution of the slip durations for 150 slip measurements on KBr(100) taken from 46 different scan frames using four different tips. The applied load was always very close to 0 nN. Four lateral force maps are shown to reveal possible correlations between their appearance and the duration of slip events. Note the irregular features within the unit cell for the two maps on the right. The colors indicate which slip durations were found in which lateral force map. The bar for shortest slip duration reflects the slips which happened faster than our time resolution of 15 μ s.

by the slip events. The magnitude of the force relaxation in the slip is of the same order or smaller than the thermal fluctuations of the force signal. Therefore, excitations of oscillations with subsequent ring-down can not be observed because thermal oscillations dominate.

We will discuss now the wide variation of slip durations in the atomic stick-slip experiments. The shortest possible duration of a slip is given by the time the cantilever needs to swing back from the deflected to the relaxed position, i.e. $1/(4f_T)$. With a torsional resonance frequency of $f_T^{con} \approx 172$ kHz this reaction time is 1.5 μ s. While we observe that many slips happen indeed on a time scale faster than our time resolution of 15 μ s, other slips may take up to several milliseconds. These long slips are very surprising as we would not expect any relaxation process on atomic scale to be that slow. A first possible explanation for slow slip events can be found in the framework of the Tomlinson model. The effective potential governing the tip movement consists of a sinusoidal surface potential and a parabolic spring potential which are continuously shifted relative to each other. The tip is stuck in a potential minimum until the ramped spring potential flattens the potential barrier to the next atomic position. The decrease of the resonance frequency of the system in the flattened potential well when approaching the slip instability is described in Refs. [26, 140]. When the resonance frequency decreases in the flattened potential, a slower reaction of the cantilever might be expected. On the other hand, thermal fluctuations activate the slip before the potential barrier has completely vanished, resulting again in a fast slip. The simulation result of the stick-slip instabilities in Fig. 4.6(a)

and (d), which will be discussed in detail in the next section, demonstrates that no retardation of the slip takes place in the single-contact model. All slip durations are clearly faster than the resolution of $15 \mu\text{s}$. As a conclusion, we can rule out any explanation for long slip durations within the simple *one-dimensional* Tomlinson model including thermal activation at room temperature.

Our results suggest that multiple tips in contact play an important role in the understanding of slow slip events. We measure fast slips of the order of several microseconds, if the lateral force maps look similar to the two-dimensional modelling for an ideal single tip reported by Lüthi et al. [35]. Slow slips occur when the lateral force maps exhibit features within a lattice unit cell or deviate significantly from the expected diamond pattern, see Fig. 4.4. Such irregularities can be explained only by multiple tips which are in contact with different unit cells of the KBr surface. In the next section simulations based on a two-spring model are presented to confirm that the picture of multiple tips is realistic.

4.4. Stick-slip Simulations with a Two-Spring Tomlinson Model

A model comprised of a single spring pulling a mass along a sinusoidal potential surface including thermal activation has described atomic friction phenomena like temperature and velocity dependence, and the distribution of jump forces [26]. The results are in agreement with experiments studying the velocity dependence [12], the temperature dependence [39], and the jump force distribution [27]. However, the experimental situation is not well represented, since a one-spring model can not reproduce both the resonance frequency of the cantilever, and the experimentally found lateral stiffness which is dominated by the contact. Therefore we extend the simulations to a two-spring model, where one spring represents the cantilever and the other spring the microscopic contact. The two springs are connected in series to a support moving at constant velocity. A tip attached to the contact spring is dragged over a periodic potential surface (see Fig. 4.5(b)). We have simulated the resulting Langevin equation including the random effect of thermal fluctuations using Ermak's algorithm [141] along the lines pointed out in Ref. [26].

The results in the last chapter suggested that the contact stiffness remains constant upon changing the applied load for a sharp tip resting in contact. This is in agreement with previous measurements by Socoliuc et al. [20] who found that the effective stiffness k is typically 1 N/m , much lower than the torsional stiffness of the cantilever which is i.e. $60\text{-}80 \text{ N/m}$. These findings strongly suggest that mainly the small group of flexible atoms at the tip apex slips rather than the cantilever or macroscopic tip. This hypothesis is also supported by a recent theoretical work by Krylov et al. [142]. They reported on the characteristic frequencies of such a tip apex and showed that what the friction force microscope measures can be very different from what the tip apex does. The small group of flexible atoms at the tip apex forming the contact with the surface is referred to as the tip in context of the Tomlinson model in this chapter. Several atoms of such a tip might be in contact with different unit cells of the surface, having a distance between the contact points that is not commensurate with the KBr(100) surface structure. Such groups of atoms we refer as single tips within a multi-tip model giving rise to a multiple contact. In an earlier study of atomic friction processes, Lifshits et al. demonstrated that for an MgO tip sliding over a LiF(100) surface a regular stick-slip behavior of the lateral force is found only after transfer of several ions from the sample to the

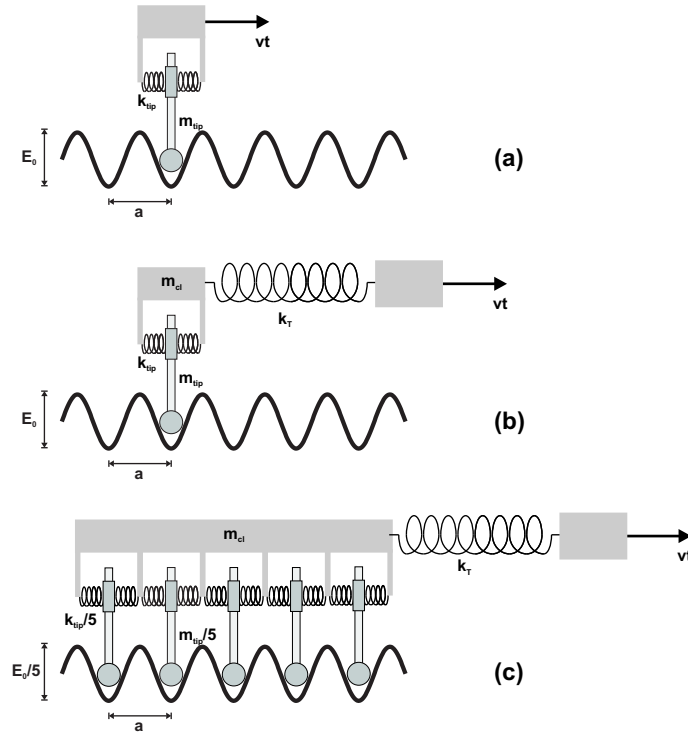


Figure 4.5: Three spring configurations for different implementation of the Tomlinson model. (a) One-spring model (b) two-spring model and (c) multiple-tip model.

tip [143]. This ion transfer, referred as self-lubrication, establishes a higher commensurability between tip and surface structure, resulting on one hand in a significant drop in total energy and on the other hand in the observation of a regular stick-slip pattern. Therefore we can assume that the very end of tip apex forming the contact consists of potassium and bromine ions.

The parameters describing the cantilever spring in the two-spring model are taken from the experimental data. An effective cantilever mass $m_{cl} = k_T / (2\pi f_T^{free})^2 = 5.5 \cdot 10^{-11}$ kg can be calculated using the frequency of the free cantilever $f_T^{free} = 168.6$ kHz and the spring constant $k_T = 62$ N/m. This is in good agreement with the calculated mass of $m_{cl} = 8.4 \cdot 10^{-11}$ kg for the cantilever beam only obtained from the geometrical dimensions ($448 \mu\text{m} \times 52.5 \mu\text{m} \times 1.5 \mu\text{m}$) and the density of silicon ($\rho_{Si} = 2328.3$ kg/m³). For the following simulations we take $m_{cl} = 5.5 \cdot 10^{-11}$ kg. The occurrence of stick-slip instabilities in the tip movement depends on the relation between the potential corrugation E_0 and the elastic energy in the springs. It can be described by the parameter

$$\eta = \frac{2\pi^2 E_0}{k_s a^2} \quad \text{with} \quad \frac{1}{k_s} = \frac{1}{k_T} + \frac{1}{k_{tip}}. \quad (4.2)$$

Stick-slip behavior is found for $\eta > 1$ [20]. We chose $k_s = 3.7$ N/m and a value of $\eta = 2$ in order to obtain a value for the potential corrugation E_0 for which the simulation produces a stick-slip pattern similar to the experimental results. Equation (4.2) allows us to determine $k_{tip} = 3.5$ N/m. The lattice constant $a = 0.66$ nm of KBr(100) determines the spatial period of the potential. The mass of the tip is assumed to be $m_{tip} = 1.0 \times 10^{-12}$ kg. Since we have no experimental estimate for the effective mass of the tip which corresponds to the tip stiffness,

we have varied m_{tip} by a factor of ten for the simulations, and found no influence on the key results described below. The damping of the tip movement is calculated in units of the critical damping $\gamma_c = 2\sqrt{\frac{k_{tip}}{m_{tip}}}$. Reimann and Evstigneev suggested that one may model tip damping based on the tip velocity relative to the surface but also relative to the support [41, 42]. For the low sliding velocities simulated here such a distinction is not necessary. The simulations are performed at room temperature and for a scan velocity of 25 nm/s. The time step used for solving the Langevin equation is 1 ns, and data points are sampled from the simulation at a rate of 3 MHz equal to the experiment.

Simulations using the two-spring model and the parameters described above provided the expected stick-slip results plotted in Fig. 4.6(a). However, the slip duration in these simulations was always shorter than 15 μ s, independent of the damping of the contact spring which was varied from critical to strong damping. Experimental friction maps often show features within a unit cell which let us conclude that the contact between the tip and the surface consists of several smaller contacts. Therefore, we expanded the two-spring model to the case of multiple tips in contact with the potential surface, where the distance between tips was either commensurate or incommensurate with the periodicity of the potential. Fig. 4.5(c) gives a scheme of the multiple-tip model. The parameters for each N -tip simulation were the same as described above, with each of the contact springs having a tip stiffness of k_{tip}/N and a mass of m_{tip}/N . We also divided the potential corrugation E_0 by the number of tips N . This scaling is chosen in order to always reproduce the experimentally observed slope and amplitude of the stick-slip force curves independent of the number of tips involved. For the multiple-tip model, the dynamics of each tip i is described by the Langevin equation

$$m_{tip}\ddot{x}_{tip,i} + m_{tip}\gamma_{tip}\dot{x}_{tip,i} + \frac{\partial E(x_{tip,i})}{\partial x} = \xi(t), \quad (4.3)$$

where the combined surface-tip potential has the form

$$E(x_{tip,i}) = \frac{k_{tip}}{2}(x_{tip,i,0} - x_{tip,i})^2 - \frac{E_0}{2} \cos\left(\frac{2\pi x_{tip,i}}{a}\right). \quad (4.4)$$

$x_{tip,i,0}$ is the equilibrium position where the springs k_{tip} have no deviations. $\xi(t)$ is a random noise satisfying the fluctuation-dissipation relation $\langle \xi(t)\xi(t') \rangle = 2m_{tip}\gamma_{tip}k_B T\delta(t-t')$, where the angular brackets denote the mean, and k_B is Boltzmann's constant. As the mass of the cantilever is many orders of magnitude larger than the tip's mass, the thermal effects on the cantilever can be neglected. Secondly, the tip apex region is associated with lower spring values than the cantilever and thus larger thermal amplitudes result according to the equipartition principle mentioned on page 28. Therefore, the cantilever's motion is described by Newton's equation.

$$m_{cl}\ddot{x}_{cl} + m_{cl}\gamma_{cl}\dot{x}_{cl} - k_{cl}(vt - x_{cl}) + \sum_i k_{tip}(x_{tip,i,0} - x_{tip,i}) = 0. \quad (4.5)$$

Figure 4.6 shows simulation results for the stick-slip process with a multiple-tip model for critical damping of the contact springs. We compare the cases of one, three, and five tips, where the multiple tips are in positions commensurate with the potential surface. The number of tips is crucial for the duration of the slip: The slips become slower for an increasing number of tips. As mentioned above, a single tip always slips faster than 15 μ s. For five tips we observe slip durations in the range of 2.8 ms to 3.2 ms. For three tips, the slips show a wide variation of duration between microseconds and milliseconds. In this case the slip often

contains intermediate states, where one or several tips have jumped but others remained in the sticking position. The duration of the slip does not depend significantly on the damping of the contact springs; no difference was noticed for critical damping and the ten times overdamped system. Details of slip events are plotted in Fig. 4.6(d)-(f). For the one-tip model, the slip happens faster than the data capture rate of 3 MHz. It is interesting to note that the thermal fluctuations clearly follow the frequency of the cantilever resonance. However, no excitation of oscillations with subsequent ring-down can be observed after jumps. The simulation for three tips reveals jumps forth and back between the previous and the final position and into intermediate states, indicating the mechanisms responsible for the wide variation of slip durations. For five tips, multiple tip jumps events smooth the transition from one atomic position to the next and cause the prolonged slip duration.

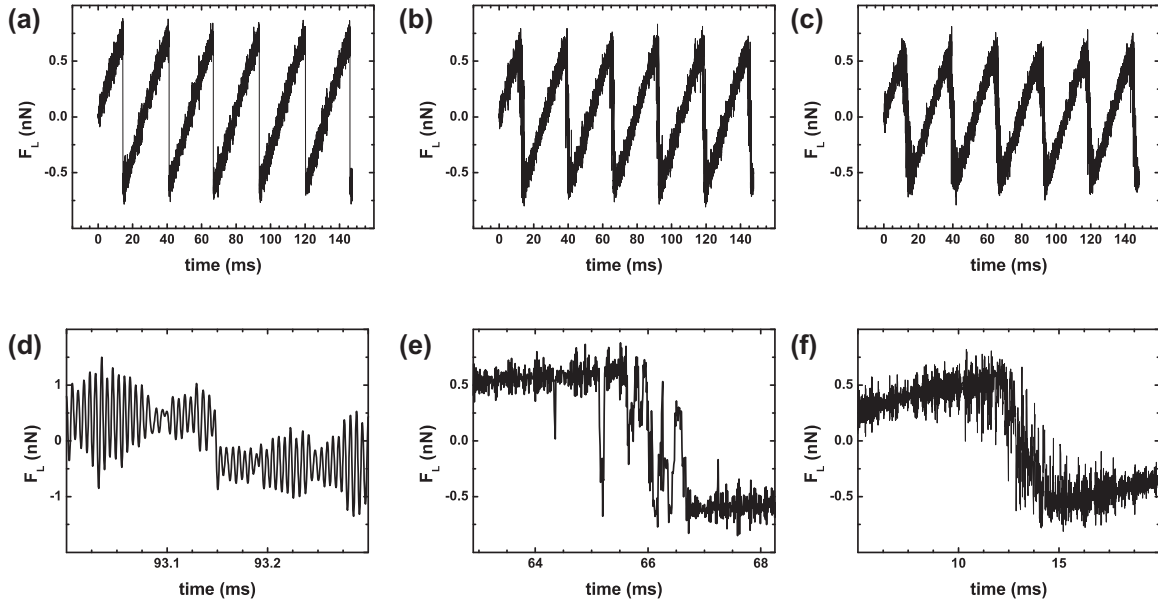


Figure 4.6: Simulation of the stick-slip process with a critically damped two-spring model. The contact consists of (a) one, (b) three and (c) five commensurate tips. Data were sampled from the simulation at a rate of 3 MHz and subsequently averaged over 50 points. (d) Zoom around the slip of the simulation with one tip, no averaging. (e) and (f) Details of the simulation for three and five tips, respectively, averaged over 30 points.

We have also studied the case of multiple tips in incommensurate contact with the periodic surface potential. For a small number of tips with a distance of $1.1 \times a$ the periodicity of the potential can be recognized in the lateral force, as shown in Fig. 4.7(a) for the case of three tips. However, for as few as five tips the asymmetric stick-slip instabilities are almost completely changed into a symmetric force modulation, compare Fig. 4.7(b). For a fully incommensurate configuration in Fig. 4.7(c) with a tip distance $\sqrt{2} \times a$ no structure of the potential is reproduced in the lateral force. This is in agreement with the experimental observations by Dienwiebel et al. on graphite, who measured atomic-scale friction as a function of the rotational angle between two contacting bodies and found that the origin of the ultra-low friction of graphite lies in the incommensurability between rotated graphite layers [51].

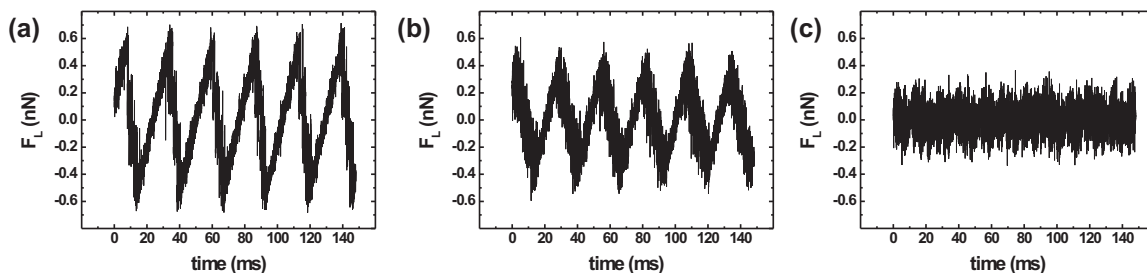


Figure 4.7: Simulation of the stick-slip process with a critically damped two-spring model. The contact consists of (a) three, (b)-(c) five incommensurate tips. Data were sampled from the simulation at a rate of 3 MHz and subsequently averaged over 50 points. The distance between the tips is $1.1 \times a$ in (a)-(b) and $\sqrt{2} \times a$ for the fully incommensurate configuration in (c).

The simulations support the idea that multiple tips can give a clear stick-slip motion, however with a significantly longer slip duration than the reaction time of the force sensor. Our three-tip model with thermal activation also reproduces the wide distribution of slip durations found in the experiments. Furthermore, the simulations indicate mechanisms for the retardation of the slips. Figure 4.6(e) shows that multiple tips do not jump coherently but that single tips can jump ahead and actually may go back to their previous atomic position before the increasing lateral force enforces a jump of all tips. A similar mechanism of molecular rebinding has been predicted through simulations of the rupture of adhesion bonds in dynamic force spectroscopy by Dudko et al. [144]. In a recent theoretical study, Krylov et al. have pointed out that the thermally activated jumps between atomic positions can create a situation of ultra-low friction, provided that the scan velocity is small enough [52]. The jump mechanism is clearly observed in our experiments. Figure 4.3(c) and (d) exhibits signatures of jumps between positions and intermediate states, respectively. The latter may also be an effect of two-dimensional stick-slip where the slipping tip takes a zig-zag path including a neighboring unit cell [8, 145]. However, a zig-zag movement should produce its characteristic slip pattern for all slips in a given scan line. Since we observe a wide distribution of slip times and shapes in a single scan line, we believe that thermally activated jumps of a multiple tip are the appropriate picture for our experiments.

Recently, Evstigneev et al. have studied single vs. multiple contact formation in atomic friction measurements on highly oriented pyrolytic graphite (HOPG) by analyzing the slips according to a single-step rate theory [146]. They found that a single-step rate equation is valid only at relatively high velocities above 90 nm/s. They suggested that at slower pulling speeds a more complicated hopping mechanism must be at work and supposed multiple bond formation to be the reason for the breakdown of the single-slip rate description. Since we observed fast slips on KBr, suggesting a single contact also for velocities below 90 nm/s, it would be interesting to verify whether a single rate theory is valid for such fast slips.

4.5. Local Correlation Function of the Lateral Force

Autocorrelation is a useful tool to find repeating patterns in a signal, such as determining the presence of a periodic signal which has been completely buried in noise. The autocorrelation is a measure of similarity of the samples' distribution, which is computed by the sum of the cross products between the data set and its shifted versions. For a real continuous function $f(t)$ the autocorrelation is defined by $R(t) = \lim_{T \rightarrow \infty} 1/(2T) \int_{-T}^T f(\tau)f(t + \tau)d\tau$. According to the Wiener-Khinchin theorem, the Fourier transform of the autocorrelation function is the power spectrum [147]. Compared to the power spectrum, fewer points are required to detect periodic signals with frequencies in the range of some kilohertz out of a noisy signal, because the information of the presence of such an oscillation is located at the beginning of the autocorrelation function in this case. Therefore, an autocorrelation analysis of the lateral force signal allows us to locally determine the strength of the torsional cantilever oscillation buried in noise. Moreover, the absence of a strong oscillation of the cantilever and its ringdown directly after the slip can be verified by this method.

The autocorrelation of white noise is zero, except at the origin which represents the variance of the signal. This means that a sampled period of white noise is statistically not correlated to a sampled period of the same white noise signal at another time. The autocorrelation of a periodic function is also periodic with exactly the same period. For example, the autocorrelation function of a damped harmonic oscillator is a periodic oscillation with an exponentially decaying amplitude. The decay length is inversely proportional to the Q-factor. Figure 4.8 shows two examples of the autocorrelation functions for the damped harmonic oscillator (a) and for white noise (b). In our measurements we have a mixture of these two signals. Therefore we expect a strong signature at the origin followed by a decaying oscillation depending on the strength of the cantilever oscillation.

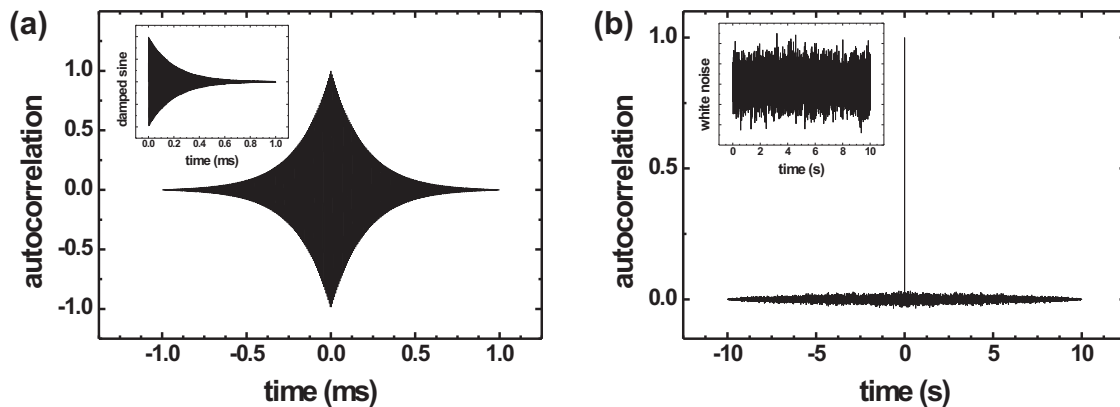


Figure 4.8: Autocorrelation function of a damped oscillator with an oscillation frequency of 160 kHz in (a) and white noise in (b). The insets show the original signal, which were used to perform the autocorrelation function.

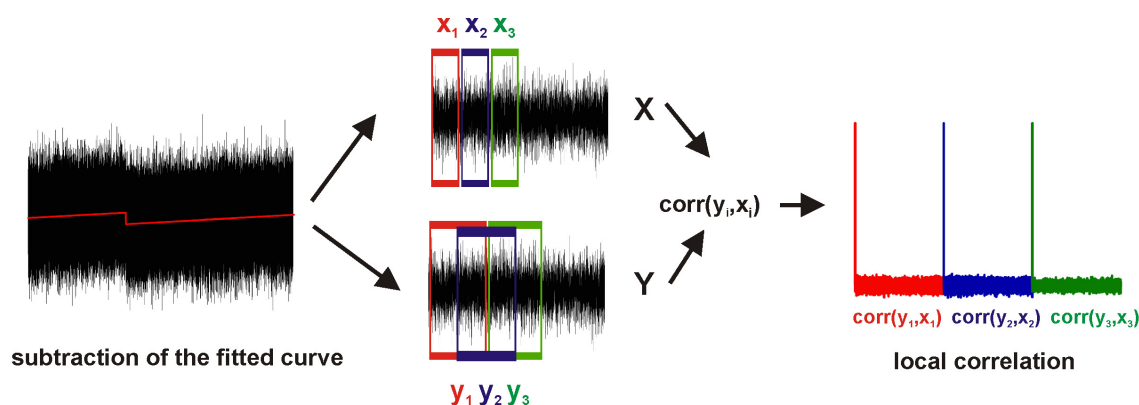


Figure 4.9: Illustration how a local correlation function of the lateral force signal is obtained.

The lateral force signal of a cantilever with its tip in contact was recorded with a high sampling frequency of 3.3 MHz while scanning along the surface. A tilted stepfunction as described in Eq. (4.1) was fitted to this sawtooth shaped friction signal as described in sections 4.3. The obtained analytical curve was subtracted from the measured data so that the resulting force signal has a mean value of zero. This is important because we want to compare different data subsets with each other. In order to obtain local information about the oscillation of the cantilever, the lateral force signal is split into several subsets containing 10,000 points each. To reduce effects which arise by performing a correlation of a finite number of points, the second subset for the correlation calculation contains the same initial data set but is doubled in size. The correlation for all these subsets is calculated and normalized so that the sequence of zero lag is identical to one. Finally, all the calculated correlation functions are plotted in one map, which typically results in a graph as shown in Fig. 4.10(a). Only the positive part of the correlation function is considered. Because the autocorrelation function is symmetric this causes no information loss. The peaks represent the first point of each correlation function calculated from a single data subset. Fig. 4.9 illustrates the calculation of local correlation of the force signal as described above.

Fig. 4.10(a) shows the local correlation of the lateral force signal while scanning over a KBr(100) surface and its corresponding force signal. This subset of a scan line with an applied load of -0.1 nN corresponds to a scan range of approximately one nanometer comprising one slip event. In the middle of the sticking phase the local correlation function indicates a strong oscillation of the cantilever. Zooming in, a frequency of 173.1 kHz is determined, which corresponds to the resonance frequency of the cantilever in contact. In the lateral force signal, the oscillation of the cantilever is completely buried in noise and cannot be distinguished. Directly after the slip event no evidence for a strong oscillation is found. The same behavior was observed for other slips.

In conclusion, this analysis confirms the hypothesis of the absence of a strong ring-down of the cantilever oscillation directly after the slip. At first glance, the strong oscillation during the sticking phase is rather surprising since the tip is in rigid contact with the sample and is not moving. Such oscillations might be explained by mechanical vibrations in the instrument. However, measurements obtained on a NaCl(100) surface measured on another microscope showed similar strong oscillations in the sticking part. In the simulations of the stick-slip

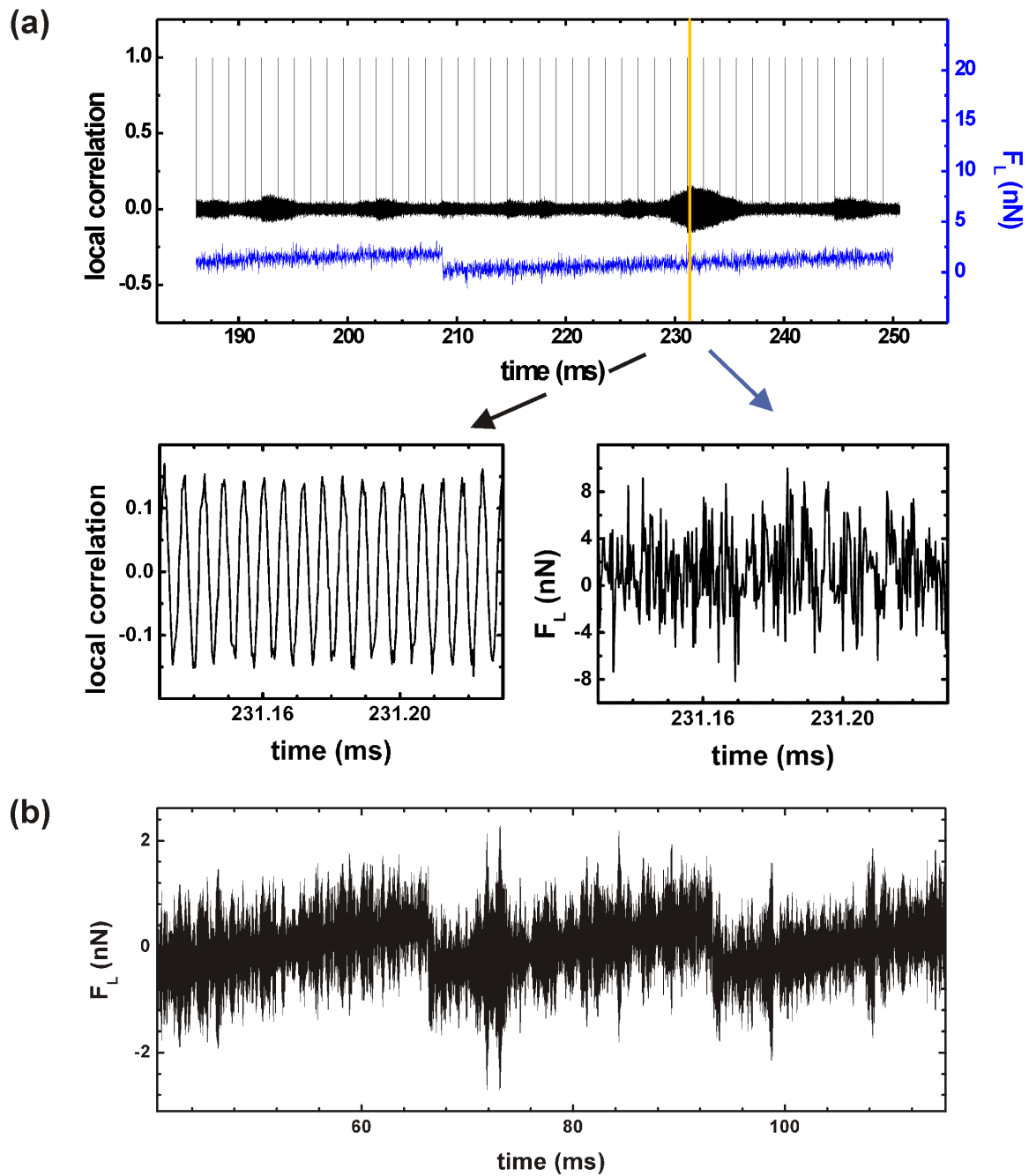


Figure 4.10: (a) The lateral force signal showing one stick-slip event and its local correlation function. A zoom of the local correlation function indicates an oscillation of 173.1 kHz corresponding to the torsional resonance frequency of the cantilever. In the lateral force signal this oscillation is buried in noise. (b) Simulation of the stick-slip with one tip with a high temporal resolution. This unaveraged data confirms possible outburst of the cantilever oscillation in the middle of the sticking phase due to thermal activation.

movement by a two-spring model including thermal noise previously described in this chapter, outbursts of cantilever oscillations were found in the middle of the sticking phase due to thermal activation. Fig. 4.10(b) shows unaveraged simulation data obtained by a one tip model. In this case no local correlation is needed since the simulation is clean of any disturbing additional electronic noise. Therefore, such strong oscillations during the sticking phase as observed in the local correlation function in Fig. 4.10(a) may arise either from a disturbance of the instrument or due to thermal activation.

4.6. Conclusions

Atomic friction phenomena have been studied in detail by means of a home-built force microscope allowing for high bandwidth detection of the lateral force signal. Recording the atomic-scale stick-slip movement of the force microscope tip with high bandwidth revealed a wide variation of slip durations up to several milliseconds, by far longer than expected for a relaxation process on atomic scale. These long slip events are believed to be the consequence of a multiple contact between tip and surface. This conclusion is drawn from a correlation between irregular features in lateral force maps and long slip durations. A comparison of our experimental results with a multi-tip simulation based on a Tomlinson model including thermal activation supports this conclusion.

5

Control of Atomic Friction by Actuation of the Contact

5.1. Introduction

Gears, bearings, and liquid lubricants reduce friction in the macroscopic world, but the minimization of friction for small devices such as micro- or nano-electro-mechanical systems (MEMS/NEMS) requires other solutions. The much greater surface-to-volume ratios lead to serious adhesion forces, which are strong enough to damage tiny devices. On the nanoscale, lubrication is not a viable option because traditional liquid lubricants become too viscous when confined in layers of molecular thickness [45]. This situation has resulted in a number of proposals how to reduce friction [148]. Sliding with negligible friction is related to superlubricity, a term used by Hirano et al. who, starting from Aubry's original ideas [149], predicted vanishing friction when two surfaces in contact are laterally stiff and incommensurate [47]. Dienwiebel et al. have observed superlubricity while dragging a graphite flake out of registry over a graphite surface [50]. Another way of reducing friction involves a reduction of the contact pressure to almost zero [20]. Moreover, a decrease in dry friction was observed when the sliding speed is reduced below a critical velocity that depends on temperature. This effect is related to thermally activated jumps occurring in the contact area and has therefore been called thermolubricity [52]. Unfortunately, all these techniques to achieve ultralow friction cannot be easily applied in practical situations and do not allow a fast switching between the ultralow and the high friction state. Recently, an efficient way to switch friction on and off at the atomic scale has been achieved by exciting mechanical resonances of the sliding system perpendicular to the contact plane [53]. The resulting variations of the interaction energy reduce friction below the sensitivity of the instrument (below 10 piconewtons) in a finite range of excitation and load, without any noticeable wear.

In the beginning of this chapter measurements on a clean NaCl(100) surface will be summarized, further validating the results described by Socoliuc et al. [53]. In the second part an extended Tomlinson model, which explains the experimental findings very well, is discussed in detail. It is shown how the residual friction force depends on the actuation frequency and scan speed. Moreover, the dependence of the energy dissipated in such a system on the damping and the influence of thermal fluctuations will be discussed.

5.2. Experiments on NaCl(100)

The experimental method of controlling friction by external actuation of the contact is discussed in detail in the PhD thesis of A. Socoliuc [150] for KBr and mica. Thus, only some measurements on a NaCl(100) single crystal are mentioned here, which further validate the effect of reduction of friction by external actuation of the contact. For a detailed description of the experiments the reader is referred to [150].

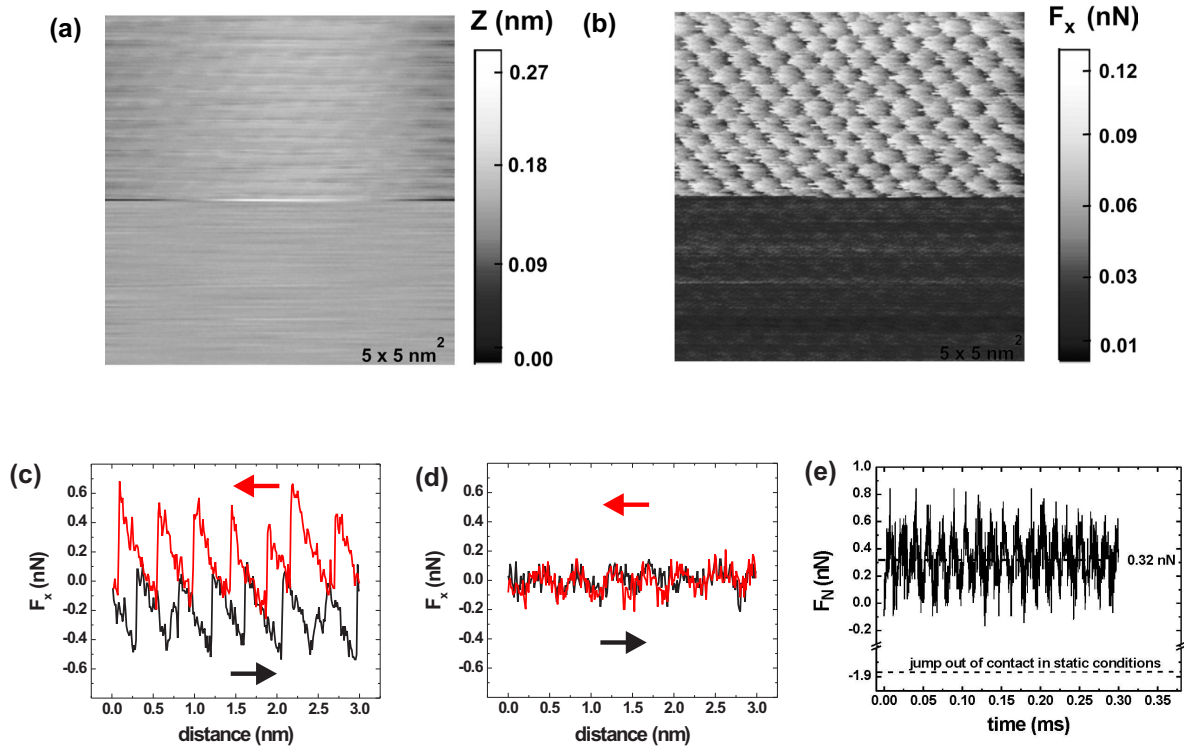


Figure 5.1: (a) Topography and (b) lateral force maps recorded, while scanning over an atomically flat NaCl(100) surface with an applied load of 2.73 nN. In the lower part of the image a sinusoidal voltage of a peak-to-peak amplitude of 1.5 V and a frequency of $f = 56.7$ kHz between tip and sample backside was applied. The lateral force F_x without an excitation voltage applied in (c) taken from the upper part of the image shows a stick-slip behavior leading to a hysteresis loop. The friction loop disappears in (d) taken from the lower part of the image, recorded with an applied excitation, confirms an ultralow friction state of smooth sliding with a perfect match between forward and backward scan. The normal force sampled with 3 MHz bandwidth in (e) suggests a modulation of the interaction due to the externally applied excitation. The mean value indicates that the tip nevertheless remains in contact. The applied load for this measurement was 0.32 nN.

Fig. 5.1(a) shows the topography and (b) the simultaneously measured friction force maps while scanning over an atomically flat NaCl surface. The averaged normal force was set at $F_N = 2.73$ nN. In the lower part of the image an AC-voltage between the cantilever and the sample holder was applied with a frequency $f = 56.7$ kHz and a peak-to-peak amplitude $U = 1.5$ V. This frequency corresponds to the first normal resonance of the cantilever in contact. In the upper part of the image stick-slip instabilities are observed which cause a hysteresis loop between the forward and backward scans and consequently energy dissipation. Fig. 5.1(c) and (d) show two lateral force traces corresponding to these two states. The lateral force traces were recorded along the [001]-direction when the tip was moving through the center of the apparent unit cells, i.e. along lines of maximal modulation of the lateral force. The disappearance of a friction loop with an applied excitation of 1.5 V in Fig. 5.1(d) indicates an ultralow friction state. The sawtooth modulation of the lateral force is transformed into a continuous modulation with a nearly perfect match between forward and backward scans, still showing the atomic periodicity of the surface lattice but negligible net friction. The recorded normal

force sampled with a 3 MHz bandwidth in Fig. 5.1(e) illustrates that the applied AC-voltage causes a modulation of the normal force. Moreover, even its maximum value remains above the negative value for jump out of contact, thus indicating that the excited tip stays in the contact.

The high bandwidth of our scan electronics allows us to monitor resonances of the cantilever excited by thermal fluctuations. In chapter 3 the frequency shift of the resonance upon contact formation was discussed in detail. Fig. 5.2(a) shows the power spectrum of the normal and lateral force fluctuations of the cantilever in contact. This power spectrum analysis confirms that the above mentioned excitation frequency of 56.7 kHz corresponds to the first bending resonance of the cantilever. A sweep of the excitation frequency in Fig. 5.2(b) indicates a reduction of friction at the normal oscillation frequency of the contact resonance and half that value. No reduction of friction was observed at the torsional resonance frequency. When the AC-voltage is switched on, the ionic crystal acts as a dielectric medium placed between two conductors. Because the thickness of the sample is much larger than the tip height, the capacitive interaction occurs mainly between the cantilever body and the sample holder. This interaction results in a capacitive force, which oscillates with twice the excitation frequency f . Besides capacitive forces, any charge trapped at the tip or any charge layer at the surface results in a nonzero contact potential and in an additional force, which oscillates at the actuation frequency f . Thus, the electro-static coupling between cantilever and sample leads to a modulation of the normal force at the normal contact resonance and capacitive coupling at half the resonance frequency. The next section shows that the modulation of the normal force acting between the tip and sample can be modeled using an extended Tomlinson model with a temporally changing surface energy corrugation.

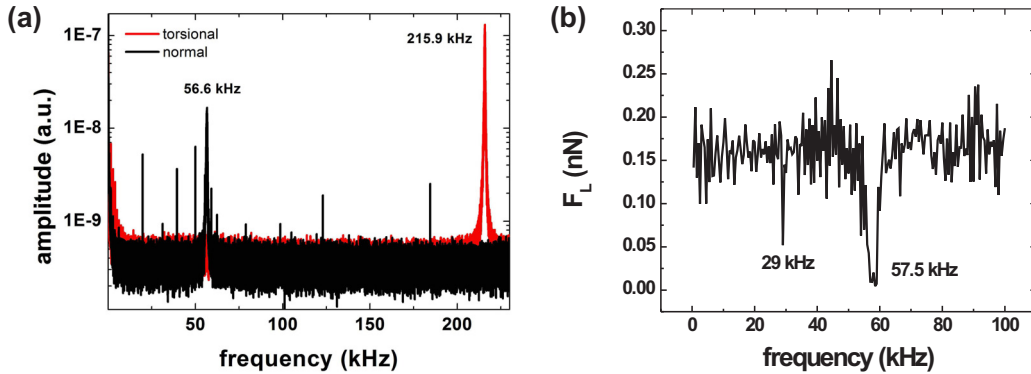


Figure 5.2: (a) Power spectrum of thermal fluctuations of the cantilever in contact showing the first torsional and bending modes. (b) Sweep of the excitation frequency indicating a reduction of friction at the normal oscillation frequency of the contact resonance and half that value.

It is important to note that the topography in Fig. 5.1(a) does not indicate a change in mean tip-sample separation whenever actuation is switched on. Thus, one can assume that the tip scans at constant mean height over the surface and the suppression of friction is not due to tip lift-off. This is in contrast to observations by D. Godfrey [151], Dinelli et al. [152] and Heuberger et al. [153] who attributed the reduction of friction due to normal vibrations to

an increase in the mean separation between the two surfaces. Riedo et al. [40] observed a partial reduction of friction using friction force microscopy when the contact between tip and a mica surface in humid air was laterally excited in a narrow range of frequencies. The actual torsional resonance in contact was not measured in that experiment. In our experiment no substantial reduction of friction was observed by exciting the torsional resonance in contact.

5.3. Dynamic Extension of the Tomlinson Model

The Tomlinson model has been used for describing different aspects of atomic-scale friction such as stick-slip showing lattice periodicity [6], dynamics (as shown in chapter 4), velocity dependence [12], or load dependence [20]. All these results were in good agreement with experiments. In this chapter an extended Tomlinson model is discussed which provides simple but novel explanation for the atomic scale control of friction by normal actuation of the contact. In the last section it was shown that the applied AC-voltage caused a modulation of the normal force. This modulation results in a periodically changing interaction between tip and surface. In terms of the Tomlinson model, this is equivalent to a surface corrugation potential with a periodically oscillating amplitude in terms of time

$$E(t) = E_0(1 + \alpha \cos(2\pi ft)). \quad (5.1)$$

The parameter α represents the normalized amplitude of the applied voltage. In the experiment this amplitude is maximal when the excitation frequency matches a bending resonance of the cantilever with the tip in contact. The modified expression of the surface potential leads to the following equation of motion assuming a one-dimensional Tomlinson model

$$\frac{dx_{tip}^2}{dt^2} + \Gamma \frac{dx_{tip}}{dt} + \omega_{tip}^2(x_{tip} - x_s) = -\frac{\pi E_0}{am} (1 + \alpha \cos(2\pi ft)) \sin\left(\frac{2\pi x_{tip}}{a}\right), \quad (5.2)$$

where $x_s = vt$ is the position of the cantilever support. $\omega_{tip} = \sqrt{\frac{k}{m}}$ represents the angular frequency of the tip and $\Gamma = \frac{\gamma}{m}$ is the damping rate, expressed in terms of the stiffness k , the damping γ and mass m of the tip. So far thermal effects have not been considered. As discussed in the last chapter, the experimental situation is not very well represented since a one-spring model cannot reproduce both the resonance frequency of the cantilever, and the experimentally found lateral stiffness which is dominated by the contact. Using a one spring model we ignore the lateral deflection of the cantilever and consider the equation of motion for the tip apex what we call tip as in the last chapter (compare page 49). In the following simulations a constant lateral stiffness $k = 1$ N/m and a lattice constant of $a = 0.5$ nm are used. As already discussed in the chapter 4, the effective mass of the tip m is difficult to determine. In this chapter, we used $m = 8 \cdot 10^{-13}$ kg, mainly for computational convenience. No qualitative change on the calculated averaged friction force was observed by lowering the mass by a factor of ten.

An adiabatic approximation, in which inertia and damping of the nanotip are neglected and the forces acting on the tip are in balance at every instant, leads to the following criteria

$$f_{tip} \gg f \quad \text{and} \quad f\Gamma \ll 4\pi f_{tip}^2, \quad (5.3)$$

where f_{tip} is the resonance frequency of the tip. The additional criterion $f \gg v/a$ ensures that the tip experiences the minimum energy corrugation many times within a lattice constant.

Due to the periodically changing E , also the parameter η , which describes the relation between the spring energy and the corrugation potential, periodically changes in terms of time. In the quasi-static case ($\alpha = 0$) it was found that if $\eta = 2\pi^2 E_0 / ka^2 < 1$ the total potential has a single minimum so that the tip slides smoothly over the surface [20]. Hence, the actuated tip is expected to slide smoothly once $\eta_{min} = 2\pi^2 E_0(1 - \alpha) / ka^2 < 1$. In other words, the parameter η_{min} replaces η in the condition for the occurrence of ultralow friction. It has been shown that the average friction force equals $F_L \equiv \overline{F_x}$ computed using the full Eq. (5.2) under these conditions for several values of α and η and plotted versus the parameter η_{min} collapse towards the usual dependence computed in the limit where the inertia and damping of the nanotip are neglected [53]. This confirms that the adiabatic approximation provides a good agreement with our observations.

The equation of motion in Eq. (5.2) was numerically solved by means of a fourth-order Runge-Kutta method. Fig. 5.3(a) shows a typical simulation result for the lateral force F_x over one lattice constant using this extended Tomlinson model with a periodically oscillating corrugation potential in terms of time and satisfying three conditions mentioned following Eq. (5.3). The simulation parameters correspond to a realistic measurement on a NaCl(100) sample, but assume actuation at frequencies about hundred times lower than the experimental frequency. This is mainly done for display purposes and chosen so that a simulation time step of one nanosecond is sufficient. In Fig. 5.3(a) a frequency of $f = 567$ Hz is used at a scan speed of $v = 10$ nm/s. In this chapter, the magnitude of η , in this case $\eta = 4$, is always referred to the quasi-static case. In this example the normalized amplitude $\alpha = 0.9$ is close to its maximum value, hence the time averaged lateral friction force is expected to be nearly zero. The time-average of the lateral force F_L for different α is plotted in the inset of Fig. 5.3(a). This plot confirms that the net friction is dramatically reduced for large enough α in both the overdamped (10 times critical damping) and underdamped cases (0.05 critical damping). It is important to note that averaged friction force plots for large η do not match for different damping rates. In the underdamped case at small α multiple slips are found as already predicted in the quasi-static case by Nakamura et al. [22] and experimentally proved by Medyanik et al. [21].

Fig. 5.3(a) indicates that the damping has not a large influence on the rapidly oscillating lateral force for small value of η_{min} , except the very short time interval $1/\Gamma$ around $a/2$ when the tip transits into the next potential well. A zoom corresponding to this moment is shown in Fig. 5.3(b). In the underdamped case, the friction force F_x is oscillating, suggesting that the tip performs a nearly free, non-adiabatic motion. The free motion is most clearly seen if the system is underdamped since the decay time is inversely proportional to Γ , but its contribution is independent of damping. Fig. 5.3(c) illustrates that the lateral force F_x rapidly oscillates between the two quasi-static envelopes corresponding to a change in η between $\eta_{max} = \eta(1 + \alpha)$ and $\eta_{min} = \eta(1 - \alpha)$.

In order to illustrate the evolution of the tip position in this oscillating potential energy landscape, the shape of the potential and the position of the tip is plotted in Fig. 5.4 for different times. All the parameters involved in this simulation are the same like for Fig. 5.3(a), except the damping ($\gamma = 10^{-6}$ kg/s). In frame (1) the friction force F_x touches the quasi-static envelope corresponding to $\eta = \eta_{min}$. At this point the energy barrier has vanished and the tip sits in a single local minimum, which is situated to the left of $a/2$. Hereafter, the growing barrier splits the single potential into two potential wells, which are slightly asymmetric versus $a/2$ so that the one on the left is slightly lower in energy. The barrier reaches its maximum

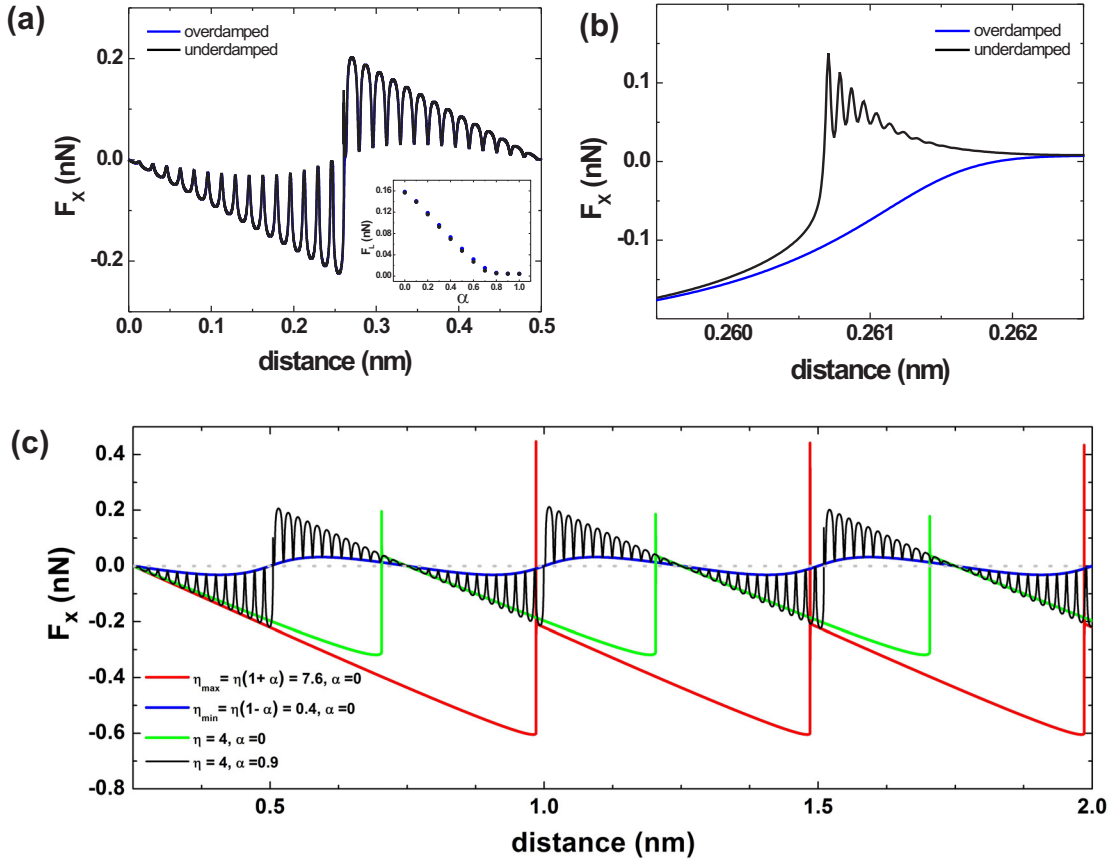


Figure 5.3: (a) Typical simulation result for the lateral force using the extended Tomlinson model with a periodically oscillating corrugation potential. The inset shows the time-averaged lateral friction force F_L for different α and confirms that the net average friction force vanishes for α approaching to one. (b) In the very short time interval right after the nanotip transits to the next potential well, the tip performs a nearly free motion, manifested in the oscillations of the lateral force F_x in the underdamped case. (c) Otherwise the lateral force F_x oscillates adiabatically between the two quasi-static envelopes corresponding to a change in η between η_{min} and η_{max} . Simulation parameters: $\eta = 4$, $\alpha = 0.9$, $f = 567$ Hz in (c) and the inset of (a) and $f = 600$ Hz (a)-(b), $v = 10$ nm/s, $k = 1$ N/m, $m = 8 \cdot 10^{-13}$ kg, $\gamma_{underdamped} = 1 \cdot 10^{-7}$ kg/s and $\gamma_{overdamped} = 2 \cdot 10^{-5}$ kg/s.

when $\eta = \eta_{max}$, as shown in frame (2). Between frame (2) and (3) the barrier vanishes again and the transition of the tip to the right side of $a/2$ occurs. In the underdamped case the tip moves fast to the next potential well and oscillates freely in this relatively flat potential well. This free motion is manifested in the oscillation of the friction force in Fig. 5.3(b). In frame (4) the single symmetric potential is now on the right side of $a/2$. After the energy barrier reappears the local minimum on the right is lower, as seen in frame (5). It is important to note that in all the graphs except frame (3), where the free motion occurs, the tip is sitting in a local minimum corresponding to the assumed adiabatic approximation.

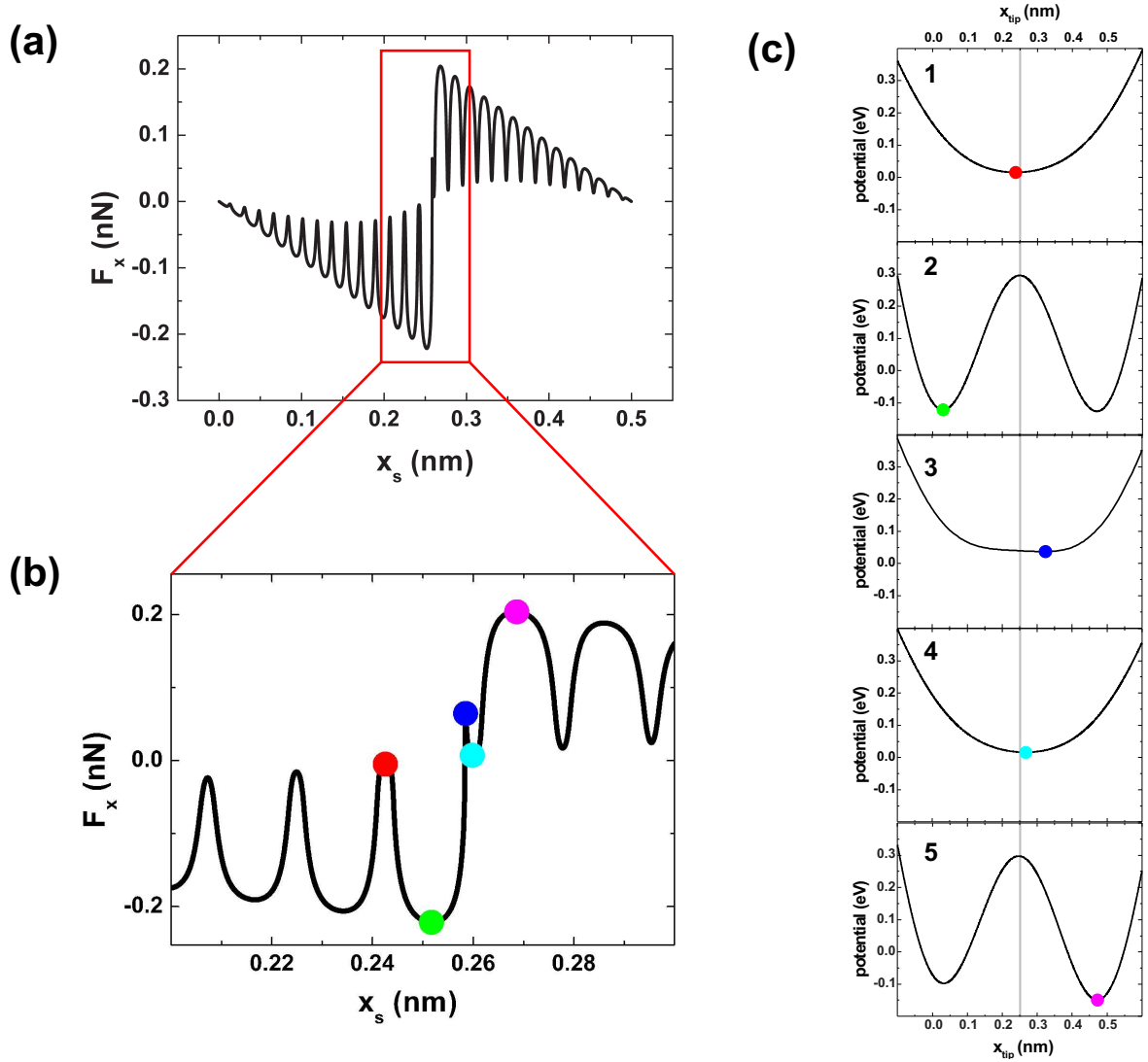


Figure 5.4: Evolution of the tip in the oscillating potential energy landscape: (a) The oscillating lateral force F_x over one lattice unit with a zoom around $a/2$, where the tip transits to the next potential well as shown in (b). (c) Different frames illustrating the instantaneous potential energy and the position of the tip. The corresponding lateral force is marked in (b) using colored points.

5.3.1 Estimation of the Residual Friction

The averaged friction with actuation does not vanish completely even if all the three criteria in Eq. (5.3) are satisfied and $\eta_{min} < 1$. In this section this residual averaged friction force will be discussed in detail. For this purpose, we first have to clarify the relation and the interplay between the four frequencies involved in the simulations. These are namely the excitation frequency f , the so-called wash-board frequency v/a , the damping rate $\Gamma = \frac{\gamma}{m}$ and the frequency of the tip in the potential well $f_{tip} = \frac{1}{2\pi} \sqrt{\frac{k}{m}}$. If the first two frequencies are incommensurate, the energy barrier vanishes at different support positions with respect to

$a/2$ for different unit cells. Such an incommensurability leads to a superstructural pattern in the simulated friction force as shown in Fig. 5.5(a) for $f = 567$ Hz and $v/a = 40$ Hz. The superperiod consists of 40 slips composed of units of five and six slips which are separated by a larger jump. Due to the incommensurability, the averaged friction force for every slip within a superperiod is different. Therefore, the residual friction force has to be determined averaging over an entire superperiod. The number of slips involved in such a superperiod N depends on the ratio between the two frequencies f and v/a and is equal to the smallest integer such that $N \cdot fa/v$ is an integer:

$$N \cdot \frac{fa}{v} \in \mathbb{N}. \quad (5.4)$$

In the case of a commensurate ratio between the actuation frequency and the wash-board frequency all the slips have the same shape and averaged friction force, as seen in Fig. 5.5(b) for $f = 600$ Hz and $v/a = 40$ Hz.

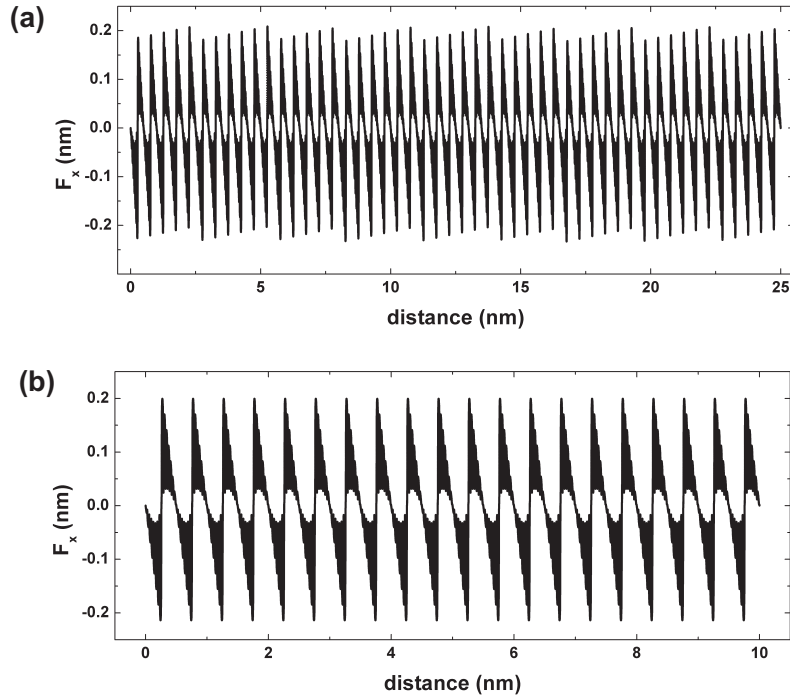


Figure 5.5: (a) The incommensurability between the actuation frequency and the wash-board frequency v/a leads to a spatio-temporal mismatch manifesting itself in a superperiod of the lateral force. This superperiod consists of 40 slips for the excitation frequency $f=567$ Hz and wash-board frequency $v/a=40$ Hz. (b) Commensurate ratio between the actuation frequency and the wash-board frequency ($f = 600$ Hz and $v/a= 40$ Hz): all the slips have the same shape and averaged friction force.

In the commensurate case, the phase shift between the actuation and corrugation determines the point in the scan movement when the energy barrier vanishes and the transition to the next equilibrium position becomes possible. Therefore, we introduce a phase ϕ in the actuation term $E(t) = E_0(1 + \alpha \cos(2\pi ft + \phi))$ and will study how the phase affects the averaged friction force. Furthermore, we define the ratio between the actuation and wash-board frequency by

the parameter M :

$$M := \frac{fa}{v}. \quad (5.5)$$

In the special case when M is an integer, the excitation and washboard frequency are commensurate and no superperiod in the lateral force is observed. For small M 's the actuation becomes comparable to the washboard frequency. This means that the barrier vanishes only a few times per lattice spacing. Fig. 5.6(a) shows the lateral force for four different phases when $M=3$, for an actuation frequency of $f = 600$ Hz and a scan velocity of $v = 100$ nm/s. The averaged friction force vs. the phase in Fig. 5.6(b) reveals an abrupt change for $\phi = 2\pi/3$. This abrupt change can be explained by the fact that the barrier close to $a/2$ vanishes for $\phi = 2.14$ before the support passed $a/2$. Therefore the tip has to wait another actuation period to transit to the next potential minimum. For $\phi = 2.07$ the barrier vanishes after $a/2$ and the tip can directly pass to the next minimum. As will be shown later, the incommensurate case represents a partial phase average and the large jumps in Fig. 5.5(a) are related to the previous phase jumps. Similar phase variation simulations showed that the number of phase jumps is given by N , the number of slips per superperiod. Moreover, there is a different phase dependence found for M odd or even. The phase for which an abrupt change in the averaged friction force is observed is currently under investigation. In any case, the phase allows us to tune the transition of the tip to the next potential minima, which takes place around $a/2$, by one oscillation of the periodically changing surface corrugation. Therefore the number of oscillations to the left and right of $a/2$ can be changed by the phase. This leads to different averaged friction forces for different phases. The residual averaged 'friction' force changes for some phases even to positive values indicating that the tip moves ahead of the support.

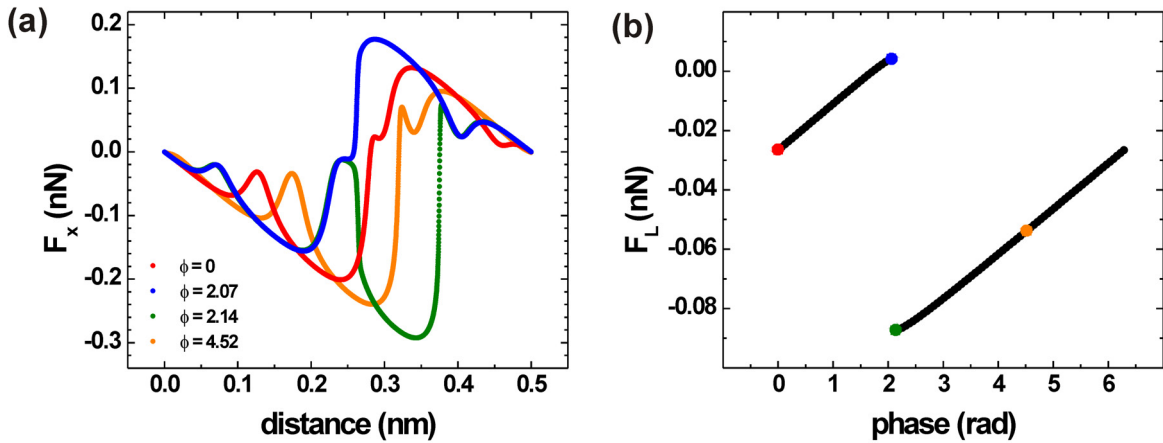


Figure 5.6: The lateral force is sensitive to the phase shift between the actuation and the corrugation: (a) Lateral force for four different phases where the actuation frequency is only three times the washboard frequency. (b) Averaged lateral friction force versus phase for the same parameters. Parameters: $\eta = 4$, $\alpha = 0.9$, $f = 600$ Hz, $v/a = 200$ Hz, ten times critical damping.

Having introduced the spatio-temporal mismatch and the phase dependence we now discuss the residual averaged friction for different scan speeds and excitation frequencies. One reason for the drastic decrease of the averaged friction in these simulations based on the Tomlinson

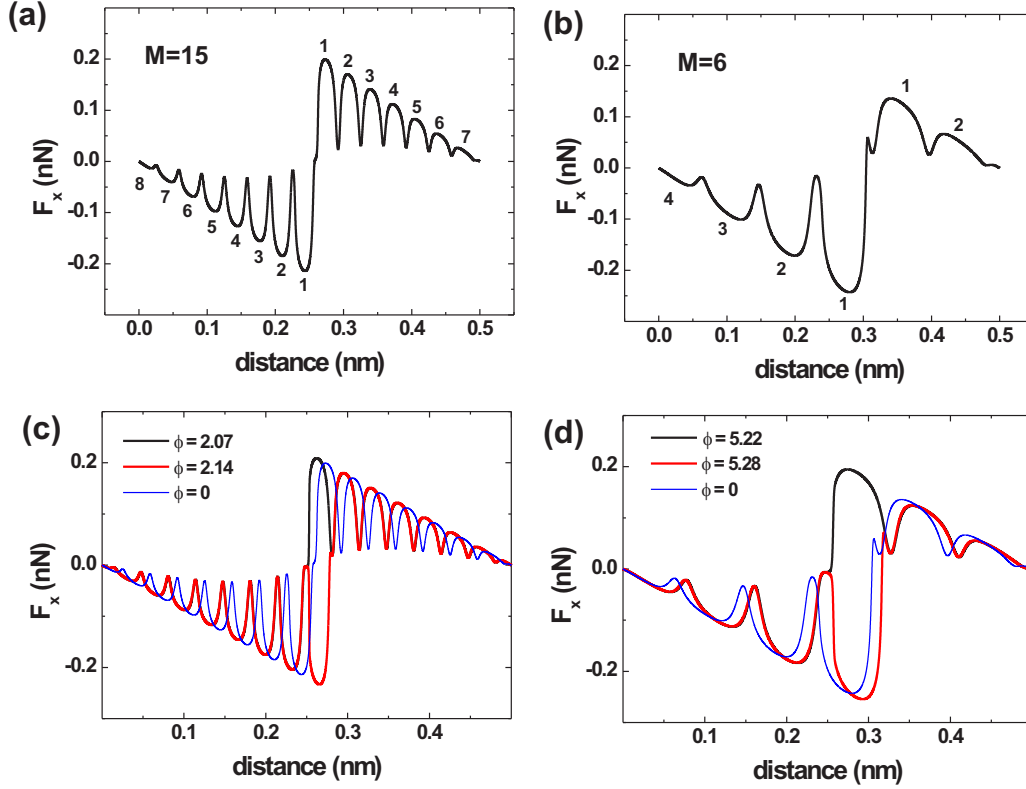


Figure 5.7: The number of oscillations in one unit cell before and after the transition of the nanotip to the next potential minimum is different and leads to an asymmetry in the lateral force. The curves in (a) and (b) indicate for phase zero about one extra period for M odd and two in the case of M even. (c) and (d) indicates zero and two of these extra oscillations by setting the phase to minimal and maximal friction force. The extra oscillations cause the residual friction force. Parameters: $\eta = 4$, $\alpha = 0.9$, $f = 600$ Hz, ten times critical damping.

model is that the lateral force before and after $a/2$ is nearly antisymmetric with respect to $a/2$ in one unit cell, once negative and once positive. Therefore, these contributions cancel each other in the averaged friction force. However, the number of oscillations before and after the support of the tip passes $a/2$ is different. These additional extra periods are not compensated for and are responsible for the residual friction force. This hypothesis is also confirmed by integration of simulated lateral force along one lattice spacing from the left and right side towards $a/2$. Fig. 5.7(a) and (b) illustrates that there is approximately one extra period for M odd and nearly two extra periods for M even with zero phase. Changing the phase corresponding to maximal or minimal averaged lateral force in Fig. 5.7(c) and (d) we find almost two extra periods.

Consequently, we can describe the maximal residual friction in the commensurate case by a simple analytic estimate, assuming two extra oscillation periods per lattice spacing are contributing to this residual friction force. We assume $\eta \gg 1$, but $\eta(1 - \alpha) \ll 1$ for this approximation. In this limit the friction force approximately oscillates between zero and the envelope with slope $k\eta_{max}/(\eta_{max} + 1) = k\eta_+$ for positions of the support between zero and $a/2$. The

slope is approximated in analogy to the relation for the quasi-static case $k_{eff} = k\eta/(\eta+1)$ [20]. This envelope corresponds to a lateral force of $k\eta_+a/2$ for x_s around half a lattice constant. Hence a maximal averaged lateral friction force per lattice spacing of

$$F_{max} = 2Ck\eta_+ \frac{a}{2} \frac{v}{fa} = Ck\eta_+ \frac{v}{f} \quad (5.6)$$

results, assuming that two extra oscillations are contributing. fa/v in Eq. (5.6) is the ratio of the time to cover one lattice spacing to the duration of one oscillation period. The factor C accounts for the anharmonicity of the force oscillation and equals $1/2$ when the force oscillation is harmonic, and 1 in the extreme anharmonic limit.

Fig. 5.8 shows simulation results for the velocity dependence of the residual averaged friction force in order to verify the above discussed analytical approximation. The simulation points confirm a linear dependence of the residual friction force with the velocity. In this simulation $\eta = 4$, and $\alpha = 0.9$ and excitation frequencies of $f = 600$ Hz and $f = 567$ Hz were chosen. The blue (0.01 critically damped) and black (10 times critically damped) bars on the simulation points represent the phase variation described before. The data points themselves correspond to zero phase. The simulations indicate that the phase influences the residual friction force for large velocities more strongly because the barrier vanishes only a few times per lattice spacing. Furthermore, this graph indicates that the incommensurate case of $f = 567$ Hz corresponds to a phase average, since the points nearly overlap the phase averaged data for the commensurate case. Moreover, these simulations show that under the assumed adiabatic conditions the residual averaged friction force is viscous-like, but not influenced by the damping. This is reasonable since the shape of the F_x vs. distance curve does not depend much on damping except in the short time interval when the tip transits to the next potential minimum (compare Fig. 5.3(a)). It is important to note that the residual friction force is below the quasi-static case as long as $f \gg v/a$. In this simulation $\eta = 4$ and $\alpha = 0.9$ were used, resulting in $\eta_+ = 7.6/8.6 = 0.884$; Eq. (5.6) yields $F_{max} = 0.884Ckv/f$. Assuming $C = 1/2$, the analytic estimate comes close to the initial slope of M even, which is itself slightly below the slope of the line through the bottoms of the phase bars corresponding to the maximal lateral force. The estimate with $C = 1/2$, only taking in account one extra period, is in good agreement to the phase averaged values. In conclusion, the linear dependence on velocity predicted by the simple analytical approximation is confirmed by the simulations.

The simple analytical expression in Eq. (5.6) does not only depend on the velocity, but also on the excitation frequency f . Therefore, simulations were also performed with a constant velocity of $v = 50$ nm/s and the frequency was varied between 100 Hz and 10 kHz. Fig. 5.9 includes both simulation with fixed velocity v and variable actuation frequency f and vice versa. The results fit together and indicate a linear dependence of the residual friction force normalized by ka on $1/M$ as predicted by the analytical approximation. Hence, the residual averaged friction force averaged over all phases is in good agreement with the analytical approximation. A difference in the averaged friction force between the overdamped and underdamped system is observed in the $1/f$ dependence for small values of $1/M$. This deviation from the linear dependence for large M in the overdamped case arises because $f\Gamma$ becomes comparable to f_{tip}^2 hence violating the adiabatic criteria in Eq. (5.3) (second condition). As long as the inequalities in Eq. (5.3) are satisfied, Eq. (5.6) and Fig. 5.8 allow one to predict the maximum and phase-averaged residual friction expected under experimental conditions. e.g. $f = 56.7$ kHz and a scan speed of 10 nm/s results in a maximum residual friction force of $8 \cdot 10^{-14}$ N using a harmonic estimate.

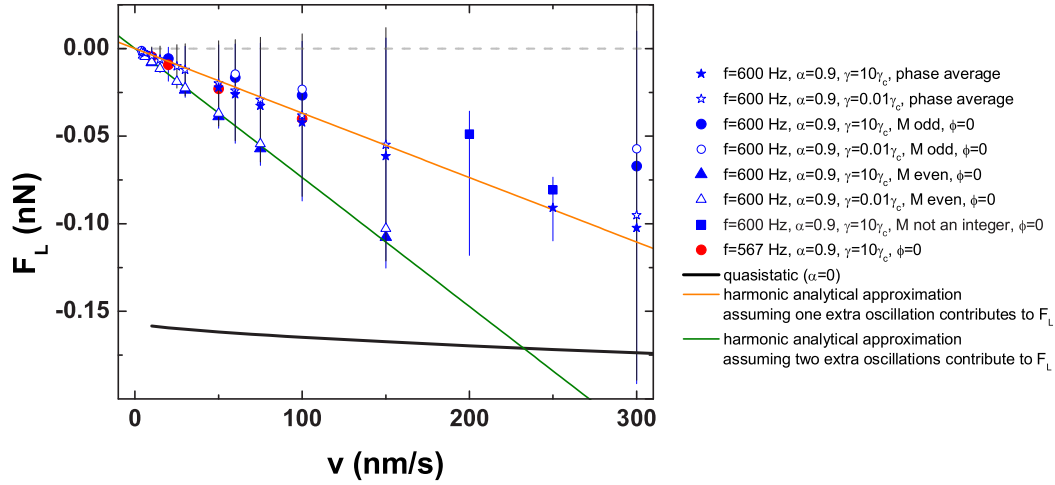


Figure 5.8: Velocity dependence of the residual friction force under adiabatic conditions when $\eta(1 - \alpha) < 1$. The residual friction force scales linearly with the velocity and is below the quasi-static limit. The simulation points for the phase averaged simulations with $f = 600$ Hz are in agreement with the simple analytical approximation in Eq. (5.6) assuming one extra oscillation period contributes on average to the residual friction force. The simulation points for M even are close to the approximation for two extra periods. The bars on the data point represent the phase dependence (blue corresponds to the overdamped points and black to the underdamped). Simulation parameters: $\alpha = 0.9$ and $\eta = 4$.

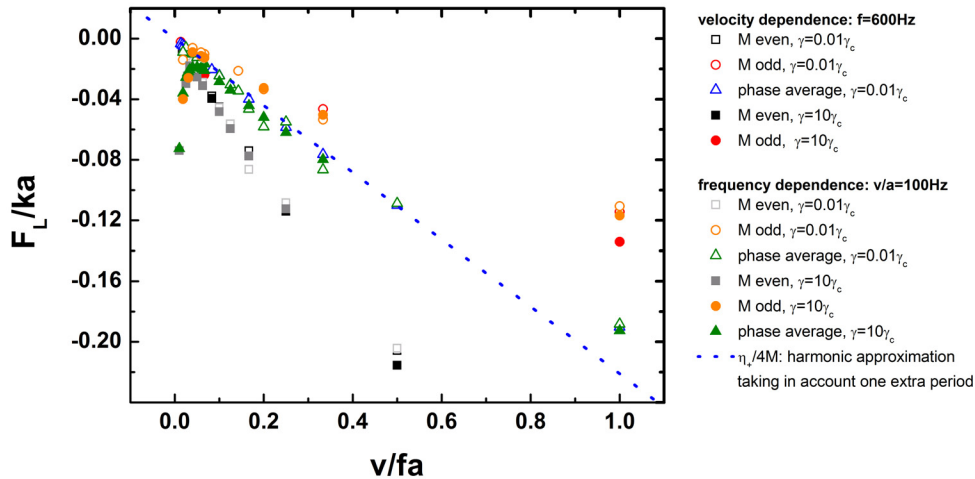


Figure 5.9: The computed normalized residual friction force F_L/ka reveals a linear dependence on $v/fa = 1/M$. Simulations with a variable frequency at a fixed velocity coincide with simulation points with variable velocity at fixed frequency. The dashed blue line represents the analytical approximation assuming one extra oscillation contributes to the residual averaged friction. These points are in good agreement with the phase averaged simulations where we expect one extra period to occur on average. Simulation parameters: $\alpha = 0.9$ and $\eta = 4$.

5.3.2 Estimation of the Energy Loss

In the last section we have approximated the residual friction force in a system with an applied external excitation. Since the normal oscillations take energy to actuate, it is not obvious how this energy compares to the energy saved by reducing friction. For this purpose we calculate numerically the total dissipated energy per lattice spacing from the expression valid for real damping proportional to velocity, as assumed in Eq. (5.2)

$$\Delta E = \gamma \int (dx_{tip}/dt)^2 dt. \quad (5.7)$$

Fig. 5.10 compares the energy loss with and without activation along one unit cell. For this simulations the same parameters as in Fig. 5.3 were used. In the quasi-static case (a) all the energy stored during the stick-stage is dissipated during the slip as indicated by the single step in the loss. The dissipated energy per lattice constant equals the friction loss $\Delta E = F_L a$. It is important to note that in the static-case the energy dissipated per lattice constant does not depend on damping as long as $1/\Gamma \ll a/v$. Because the tip relaxes after the slip long before the next slip occurs, all the energy stored in the spring is dissipated independent of the damping rate. Ignoring thermal effects the loss in the static case is also nearly constant for different velocities as long as the scan velocity is much smaller than the tip velocity [25, 154]. Fig. 5.10(b) and (c) indicates that the actuation in order to reduce friction, causes a strong dependence of the loss on damping. In the overdamped case (b), energy is continuously dissipated over a lattice constant due to the actuation. The energy loss close to $a/2$, when the tip transits to the next local energy minimum is small compared to the entire dissipated energy. Nevertheless, the energy loss in this example is still less than for the static case. In the underdamped case in Fig. 5.10(c), the loss due to actuation is small and the transition to the next energy minimum dominates the energy loss. This loss contribution is due to the non-adiabatic free motion of the tip in the short time interval after the transition.

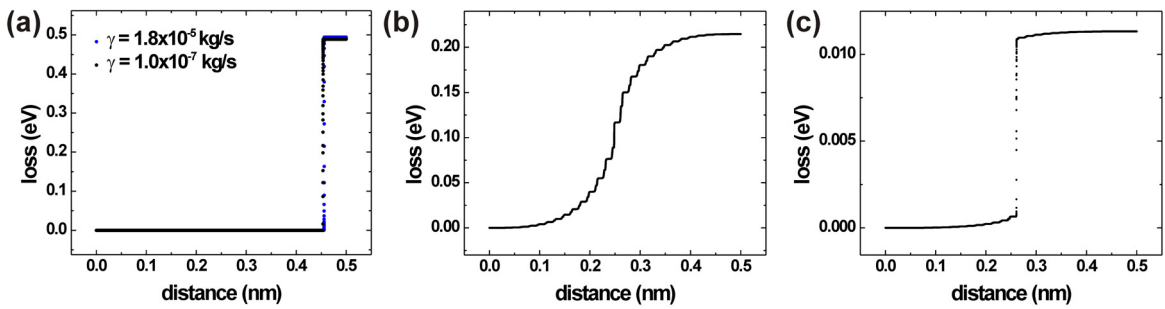


Figure 5.10: Energy loss around one slip for (a) the quasi-static case, (b) the overdamped case with actuation ($\gamma = 1.79 \cdot 10^{-5}$ kg/s, $f = 600$ Hz), (c) the underdamped case with actuation ($\gamma = 1.7 \cdot 10^{-7}$ kg/s, $f = 600$ Hz). In the overdamped case the energy is continuously dissipated over a lattice constant due to the actuation while in the underdamped case the loss due to actuation is small and the transition to the next energy minimum dominates the energy loss. It is important to note that the energy loss with actuation in this example is still less than for the static case. Further simulation parameters: $\eta = 4$, $\alpha = 0.9$, $v = 10$ nm/s.

From these observations we divide the energy loss ΔE over one lattice spacing into two contributions. The first term considers the loss caused by the actuation done and the second term the free motion of the tip during the transition to the next minimum. Let us analyze the loss due to activation first. x_{tip} oscillates between 0 and the envelope with slope η_+vt for the first half of the lattice constant. Hence, the amplitude A of the oscillation in x_{tip} is proportional to η_+vt and the amplitude of dx_{tip}/dt is proportional to $2\pi fA = 2\pi f\eta_+vt$. Therefore the energy loss can be expressed by the following integral according to the definition in Eq. (5.7)

$$\Delta E = \gamma \int_0^{a/2v} (dx_{tip}/dt)^2 dt = 2D\gamma(2\pi f\eta_+v)^2 \int_0^{a/2v} t^2 dt = D\gamma \frac{\pi^2}{3} \frac{(f\eta_+)^2 a^3}{v}, \quad (5.8)$$

where the factor D addresses the anharmonicity of the oscillation. For a harmonic oscillation we have $D = 1/2$ and in general D is between one and zero. The factor 2 considers the contributions from the left and the right side of $a/2$. The second contribution to the loss is related with the free motion as the tip relaxes to the next energy minimum. It was found by numerical simulations that this term scales with v/f . In close analogy with the loss in the absence of actuation one can suppose, that the potential energy stored by the spring during the extra periods, which gives rise to the net residual friction force, is released and dissipated during the free motion. The second term is phase-dependent and scales as $1/M$ like aF_L . The actuation term dominates for large M because it is proportional to M^2 while for small M the second term dominates. The analytical formula representing this term is currently under investigation.

The analytical formula for the loss due to actuation in Eq. (5.8) predicts a linear scaling of the loss with $f^2 a^3/v$ for large M . This scaling was confirmed by numerical simulations shown in Fig. 5.11(a) for an overdamped system and (b) for an underdamped system. For small values of $f^2 a^3/v$ the second term of loss dominates and hence we observe a deviation. This loss due to actuation is not phase-dependent since the data points for M odd and even are on one straight line. Fig. 5.11(c) shows the loss with actuation normalized to the static loss. This curve indicates that in an intermediate range of $M = fa/v$ which increases as the damping increases not only the friction is reduced but compared to the quasi-static case also the net energy loss.

5.3.3 Thermal Effects

In this section we discuss preliminary results including thermal activation effects. For this purpose random noise $\xi(t)/m$ satisfying the fluctuation-dissipation relation

$$\langle \xi(t)\xi(t') \rangle = 2\gamma k_B T \delta(t - t')$$

is added on the right side of the equation of motion in Eq. (5.2). The angular brackets denote a time average, and k_B is Boltzmann's constant. We have simulated the resulting Langevin equation including the random effect of thermal fluctuations using Ermak's algorithm [141] along the lines discussed in Ref. [26]. The Box-Muller algorithm was used to generate normally distributed stochastic numbers with zero mean and unit variance from a pair of uniformly distributed numbers obtained by the random number generator function 'ran2.c' from Numerical Recipes [147].

Fig. 5.12(a) and (b) show the average friction force F_L for different α and η in a 0.05 and a 10 times critically damped system for $T = 293$ K. Since the lateral force is of statistical nature

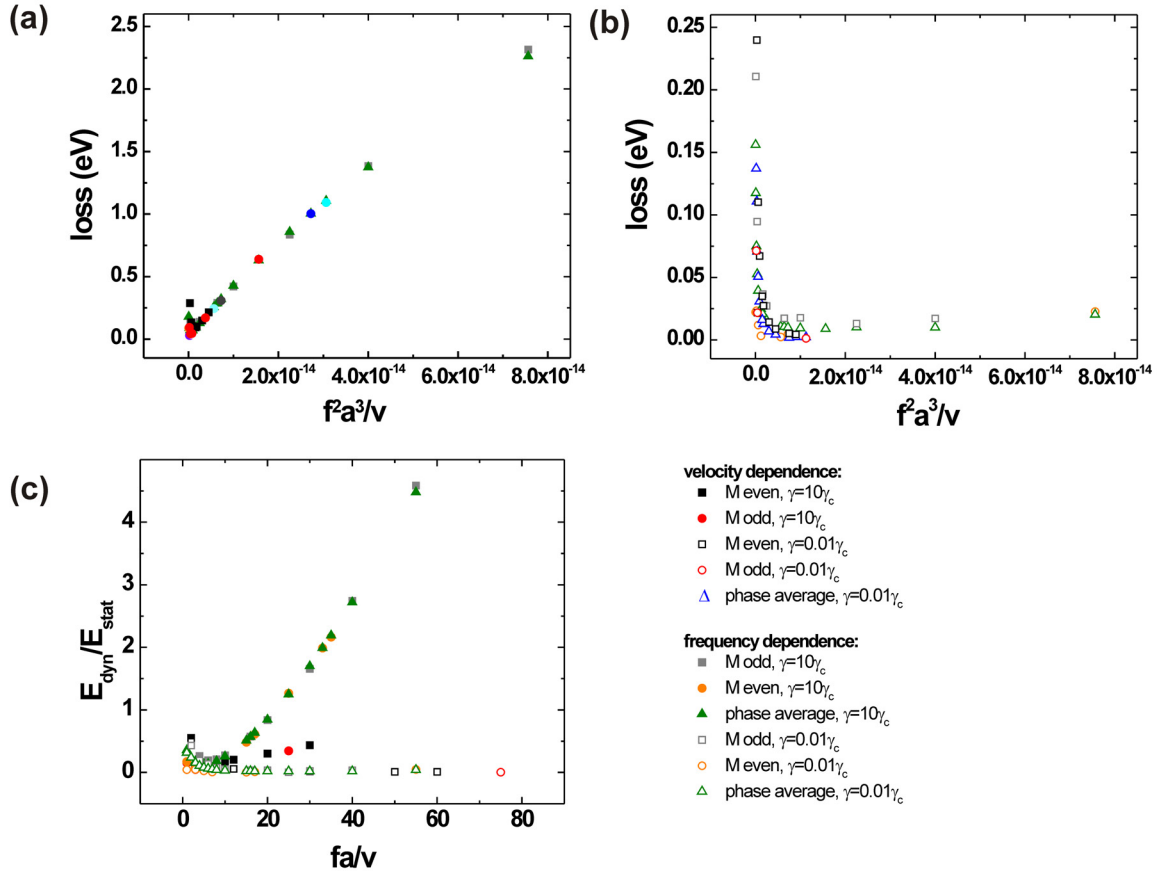


Figure 5.11: Numerical simulation of the energy loss with actuation. (a) and (b) show the loss in the overdamped (a) and underdamped (b) case versus $f^2 a^3 / v$. For large M a linear scaling is found in accordance with the analytical estimate in Eq. (5.8) for the actuation loss. For small M the dissipated energy during the free motion after the tip transits to the next stable potential minimum. (c) The loss with actuation E_{dyn} versus the static loss E_{stat} suggests that in the underdamped case for large M not only the friction is reduced but also the energy loss in the system.

when including thermal activations each point was averaged over 200 lattice constants. Both plots confirm that the reduction of friction by actuation persists also at finite temperatures. For higher η in the underdamped case multiple slips were observed, as already found in the static case by Nakamura [22] and experimentally proved by Medyanik et al. [21]. In both cases friction is reduced for small α compared to the static case since the tip can jump earlier to the next local minimum due to thermal activation. Fig. 5.12(c) and (d) compares the lateral force with and without thermal activation. For α close to one no multiple jumps occur and some of these oscillations are inverted as seen in Fig. 5.12, because the tip jumps back to the previous potential minimum. This partially compensates for the extra oscillations, which gives rise to the net F_L , hence reducing it even more.

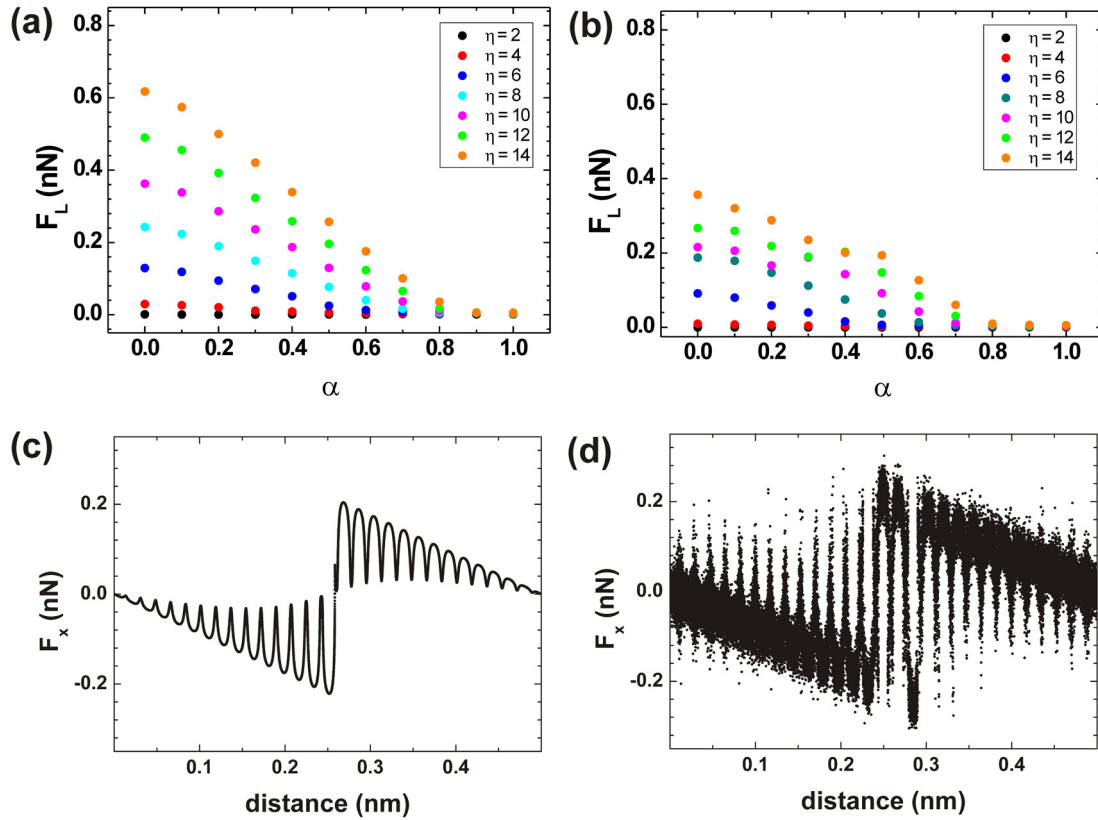


Figure 5.12: Effects of thermal activation on friction simulations with actuation. (a) and (b) show the residual averaged friction force for different α and η for an (a) overdamped (10 times critical damping) and (b) underdamped system (0.05 times critical damping). In both cases data is averaged over 200 lattice constants. (c) and (d) compares the lateral force with (d) and without (c) thermal activation for a critically damped tip. Simulation parameters: $T = 293$ K, $v = 10$ nm/s, $f = 567$ Hz and (c)-(d) $\alpha = 0.9$ and $\eta = 4$.

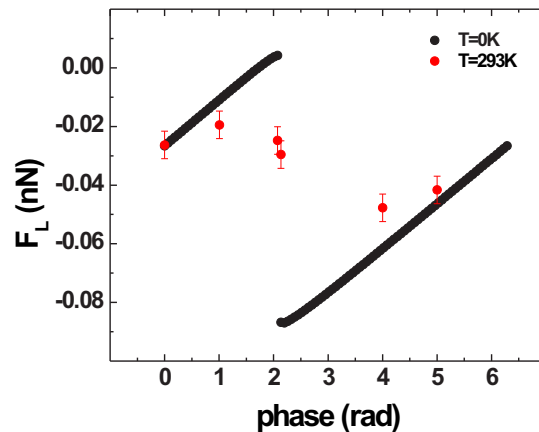


Figure 5.13: Phase dependence with thermal activation at $T = 293$ K for a frequency of $f = 600$ Hz and a scan speed of $v = 100$ nm/s. The clear phase dependence as observed without thermal activation disappears. This indicates that thermal activation leads to a partial phase averaging.

Furthermore we studied the influence of thermal activation on the phase dependence in that limit. Fig. 5.13 shows that the strong phase dependence observed in Fig. 5.6 disappears at higher temperatures. This indicates that thermal activation allows the tip to jump forward and backward when the potential barrier vanishes around $a/2$. The simulation thus shows that thermal activation leads to a partial phase average.

5.4. Conclusions

In recent years several mechanisms for achieving ultralow friction were suggested, but most of them cannot be easily applied in practical situations. Moreover, they do not allow us a fast switching between an ultralow and a high friction state. In this chapter an efficient way to switch friction on and off at the atomic scale has been described and explained by exciting the mechanical resonance of the sliding system perpendicular to the contact plane [53]. In order to understand the atomic scale control of friction by actuation of nanometer-size contacts an extended one-dimensional one spring Tomlinson model was discussed in detail. First, it was explained how the tip is moving in the oscillating surface potential. An analytical estimate for the residual friction force was found which is in good agreement to numerical simulations. This model suggests that for low enough damping the friction but also the energy loss can be dramatically minimized compared to the quasi-static case.

Ultrathin Alkali Halide Films: Heteroepitaxial Growth and Atomic-scale Friction

6.1. Introduction

The lattice mismatch in heteroepitaxy can produce large strain, whose relief creates a multitude of surface structures such as dislocation networks or self-assembly of quantum dots. While these surface structures have interesting physical properties in themselves, they can also be used as templates for the heterogeneous nucleation of island superlattices, or for the regular arrangement of single molecules or molecular clusters [155]. The heteroepitaxy of alkali halide crystals provides model systems for studying strain relief structures of insulators because of the large range of lattice constants and the comparatively simple preparation. Heteroepitaxial growth for various combinations of alkali halide crystals over a wide variety of lattice mismatches has been studied in several reflection high-energy electron diffraction (RHEED) experiments [156–159]. One of the results of these studies is that alkali halide thin films grow epitaxially in a layer-by-layer mode for lattice mismatches smaller than 20% and in a three-dimensional island mode for larger mismatches.

Scanning probe microscopy is not only a tool to reveal strain relief structures and the underlying atomic structure in real space, it also allows us to study the development of individual islands at the very initial stage of film growth. The development of high-resolution non-contact atomic force microscopy has extended these capabilities to insulating surfaces. Several scanning tunnelling microscopy and nc-AFM studies have described the heteroepitaxial growth of ultrathin well-ordered alkali halide films on metals and semiconductors [160–166]. For coverage of one or two atomic layers, a carpet-like growth mode was observed: The first layer grows in form of large islands with hundreds of nanometers side length, smoothly covering substrate steps. The subsequent layers grow in form of smaller rectangular islands with tens of nanometers side length. Very few atomic force microscopy studies have reported on the growth of alkali halide films on alkali halide crystals. Mazur et al. have described a layer-by-layer growth of twenty monolayers of LiBr on LiF(100) and the formation of rectangular pits in these films upon annealing as found in contact-mode AFM experiments [167]. The advantage of the SPM technique compared to numerous scattering and diffraction measurements is that surface structures can be studied in the real space without electron and photon-stimulated decomposition.

Theoretical models and numerical simulations propose various interface structures for the accommodation of the lattice mismatch at the interface of two alkali halide crystals, including stacking faults, elongated lattice constants, and surface rumpling [168–172]. Kiguchi et al.

[173] found that the lattice distortion in the film relaxed more rapidly for systems with a film lattice constant larger than the substrate lattice constant (positive misfit) as compared to systems with a smaller film lattice constant (negative misfit). The difference between the two cases was attributed to the anharmonicity of ionic bonds, which makes the elongation of ionic bonds easier than their compression.

In this chapter the sub-monolayer growth of films of KBr on NaCl(100) and of the complementary system NaCl on KBr(100) are characterized by means of nc-AFM in ultrahigh vacuum. NaCl and KBr have a lattice mismatch of 17%, the ratio of nearest-neighbor distances of NaCl and KBr is very close to seven to six. Despite the large lattice mismatch, a layer-by-layer growth has been observed in RHEED studies [159]. Duan et al. [174] found the signature of a superstructure on top of KBr films grown on NaCl(100) by helium atom scattering experiments. The periodicity of the superstructure was indeed seven times the next-neighbor distance of the NaCl(100) surface. In this chapter images of the superstructure as observed in real space by force microscopy are presented. The growth mode is compared with that of the complementary system of NaCl on KBr(100). In addition to the structure, contact AFM provides information on the local stiffness, potential energy landscape, and frictional properties of the composite system. Hence, we performed a friction force microscopy study to give further insight into the properties of such films. The influence of such structures on friction force microscopy imaging will be discussed in detail.

6.2. Heteroepitaxial Growth of KBr/NaCl(100) and NaCl/KBr(100)

Atomically flat and clean KBr(100) and NaCl(100) were prepared by cleaving in air and UHV, respectively. Further details of the sample preparation are mentioned in section 2.5. Ultrathin films of NaCl and KBr were evaporated on the clean substrate from a Knudsen cell. The evaporation rates were calibrated with a quartz-balance and analysis of the AFM images. Evaporation rates in the range from 0.1 Å/min to 2.4 Å/min have been used.

6.2.1 Heteroepitaxial Growth of KBr on NaCl(100)

The sub-monolayer growth of KBr on an atomically flat NaCl(100) surface is shown in Fig. 6.1(a). Rectangular islands with a height of two or three atomic layers and a typical side length of 15 nm are homogeneously distributed over the surface. Islands of one monolayer height are not observed. While the first two layers always form complete rectangular islands, the third layer may cover only part of double layer rectangular islands. The lateral size of islands depends on the evaporation rate. At a higher evaporation rate islands with side length less than 15 nm are formed. In Figure 6.1(a) and (c) the influence of the evaporation rate can be directly compared, since these images have the same scan range: in (a) a rate of 0.1 Å/min was used compared to 2.4 Å/min in (c). Note that the coverage on both samples was slightly different with 27% in (a) and 37.8% in (c). The histogram in Fig. 6.1(d) illustrates the different distributions of the island size in dependence of the rate. The fitted Gaussians reveal an averaged side length of 13.7 nm for 0.1 Å/min and 7.5 nm for a rate of 2.4 Å/min. During evaporation the NaCl substrate was held at a temperature of 25° C. A complete stripe of KBr decorates the upper terrace at an atomic step on the NaCl substrate as can be seen in Fig. 6.1(c). Some KBr islands on the lower terrace are attached to the steps. However, none of the KBr islands are found to be overgrowing the step.

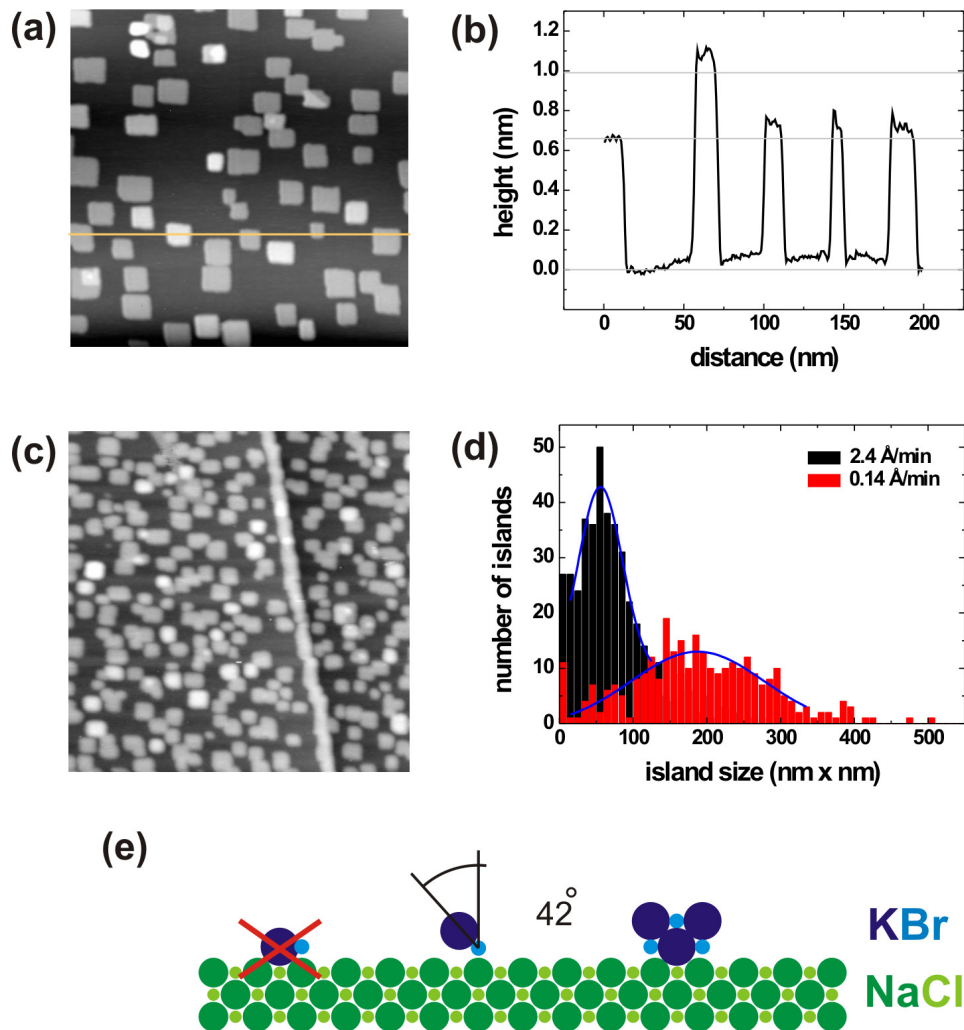


Figure 6.1: Topography images of NaCl(100) partially covered with KBr. The section in (b) shows that the islands are two and three atomic layers high. The typical size of the KBr islands depends on the evaporation rate: (a) slow rate of $0.1 \text{ \AA}/\text{min}$ and (c) high rate of $2.4 \text{ \AA}/\text{min}$. (d) shows the distribution of the island size depending on the evaporation rate. (e) illustrates the adsorption of a KBr monomer on NaCl as discussed by Celli and Urzua [175]. They claimed isolated KBr molecules prefer to stand upright on a NaCl substrate and build directly a double layer. Image sizes: (a) and (c) $200 \text{ nm} \times 200 \text{ nm}$.

In the submonolayer growth of KBr on NaCl we observe islands of two and three atomic layers height, but none of one monolayer. This finding is in agreement with the work by Duan et al. [174], who noted in their high-resolution helium atom scattering measurements that during the growth of KBr onto NaCl(100), the first film layer takes twice as long to complete as subsequent layers. Therefore, they suggested that this first layer is a bilayer. Their conclusion is supported by calculations of Celli and Urzua [175], who suggested a tilt angle of 42° between the axis of an adsorbing NaCl monomer and the normal to the KBr substrate. In these calculations it was assumed that the cation adsorbs on top of the surface anion, as illustrated in Fig. 6.1(e). Hence, they claimed isolated KBr molecules prefer to stand upright on a NaCl

substrate and build directly a double layer. The fact that alkali halide monomers can either stand upright or grow flat on top of the surface has also been observed for the submonolayer growth of NaCl on metallic and semiconductor surfaces, where double layers [160, 163] and monolayers were observed [161].

The surface of the KBr islands exhibits a regular superstructure. This superstructure is observed on islands of both two layer and three layer height. The corrugation of the superstructure is too small compared to the island height to become visible in the topographic representation of the islands in Fig. 6.2(a). In contrast, the derivative of the topography (b), the frequency shift Δf -image (c) and the corresponding A_{exc} -image in (d) reveal the superstructure clearly. The white contrast on the left island edge and the black on the right island edge in the A_{exc} -image indicate that the controller was not fast enough to maintain constant frequency shift. This is also seen in the error signal of the topography control, the Δf -image. Any occurrence of energy dissipation in the tip-sample interaction would dampen the cantilever oscillation and require an increase of the excitation amplitude A_{exc} applied to the piezo actuator. Therefore, A_{exc} is often referred to as damping signal. Despite recent efforts, a quantitative understanding of A_{exc} measurements is not straightforward [73, 75]. In this section we exploit the characteristic distance dependence of the damping signal [76] to reveal surface structures with very small topographic corrugation. By recording the damping signal simultaneously with the topography signal, subtle details of the surface topography can be detected which are often lost by the feedback circuit working with the more long-range frequency shift signal.

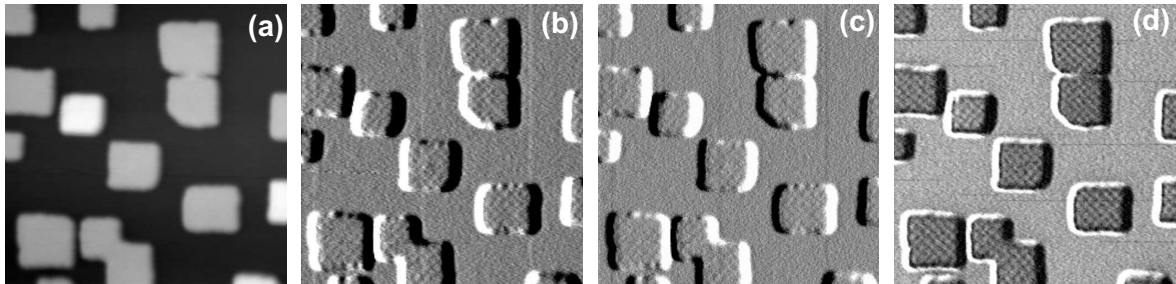


Figure 6.2: The corrugation of the superstructure is too small compared to the island height to become visible in the topographic representation of the islands in (a). However, the derivative of the topography (b), the frequency shift Δf -image (c) and the corresponding A_{exc} -image in (d) reveal the superstructure clearly. This image is a detail of Fig. 6.1(a). Imaging parameters: scan size $100 \text{ nm} \times 100 \text{ nm}$, $f = 153.6 \text{ kHz}$, $\Delta f = -14.11 \text{ Hz}$, $Q = 38100$, $A = 11 \text{ nm}$.

High-resolution images of small areas on top of a double layer island are shown in Fig. 6.3. The periodicity of the superstructure is found to be $3.73 \pm 0.2 \text{ nm}$ along the [100]-direction. The ratio of unit cell size between KBr and NaCl is nearly 6:7. Therefore, a periodicity of six unit cells of the KBr film respectively 3.9 nm could be expected for the periodicity of the superstructure. This is in agreement with the helium scattering results of Duan et al. [174] and the predictions of Baker et al. [169]. Fig. 6.3 shows the topography (a) and the corresponding A_{exc} -map (b) of the superstructure, with a typical cross-section detailed in (c). The corruga-

tion of the superstructure is observed to take values up to 0.12 nm on two layer thick islands and up to 0.11 nm on three layer thick islands depending on the tip used and the frequency shift applied. The measured corrugation increases towards the edge of islands, and depends strongly on the tip shape. These findings resemble the observations for corrugation variations in atomic resolution imaging of alkali halide surfaces which were found to originate in the coordination of surface atom and in the details of the tip structure [176]. The corrugation of the superstructure we measured using nc-AFM is about a factor ten higher than Baker et al. [169] calculated in their Monte Carlo simulations without including an AFM-tip and Duan et al. measured by helium atom scattering [174].

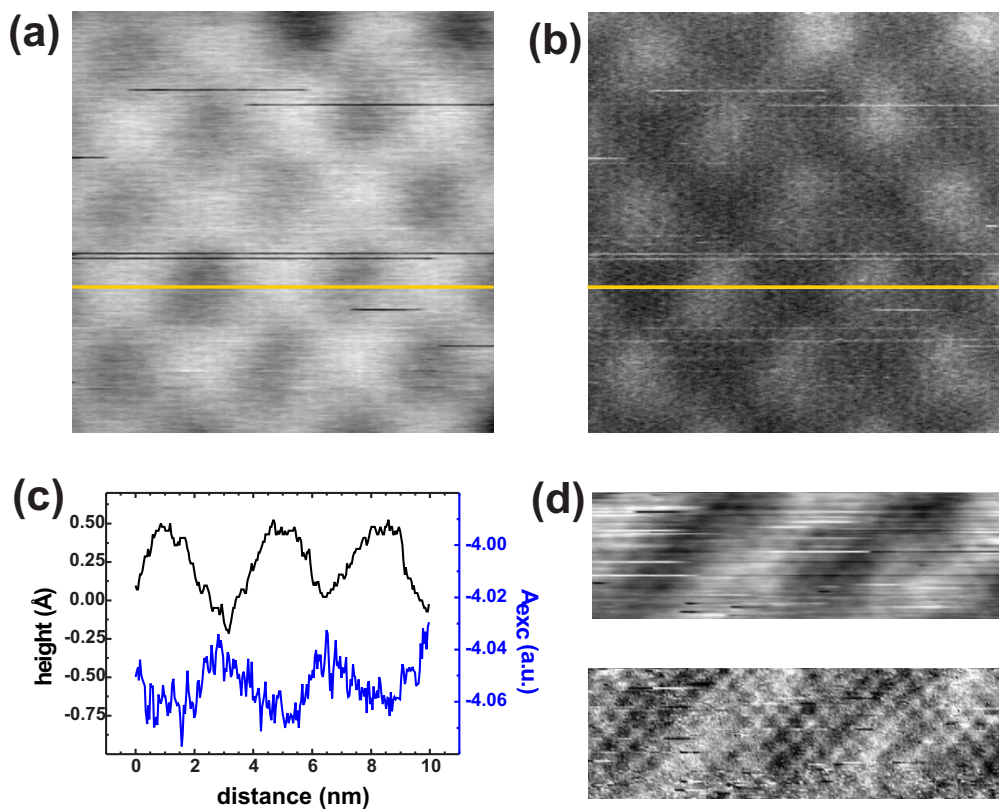


Figure 6.3: Topography (a) and A_{exc} -map (b) showing the superstructure on top of a double layer KBr island grown on NaCl(100). The pronounced corrugation in the upper row of features can be attributed to the fact that this row forms the edge of the film. (c) Cross-section of (a) and (b) along the white lines. (d) Topography (upper image) and corresponding frequency shift image (lower image) showing atomic resolution across the superstructure. Imaging parameters: (a)-(b) $10 \text{ nm} \times 10 \text{ nm}$, $f = 153.6 \text{ kHz}$, $\Delta f = -28.4 \text{ Hz}$, $Q = 38100$, $A = 11 \text{ nm}$ and (d) frame width 10 nm , $f = 154.9 \text{ kHz}$, $\Delta f = -32 \text{ Hz}$, $Q = 36300$, $A = 7 \text{ nm}$.

The cross-section of the damping signal in Fig. 6.3(c) shows an increased damping signal in the topographic valleys of the superstructure. The atomic lattice underlying the superstructure is

revealed by high-resolution images in Fig. 6.3(d). The atomic periodicity appears pronounced in maps of the frequency shift, i.e. of the error signal of the topographic feedback as the tip is moving at quasi-constant height on the lateral scale of the atomic lattice. Fourier analysis of such images verifies a relation of 6:1 between the lattice of the superstructure and the lattice of the KBr(100) island surface.

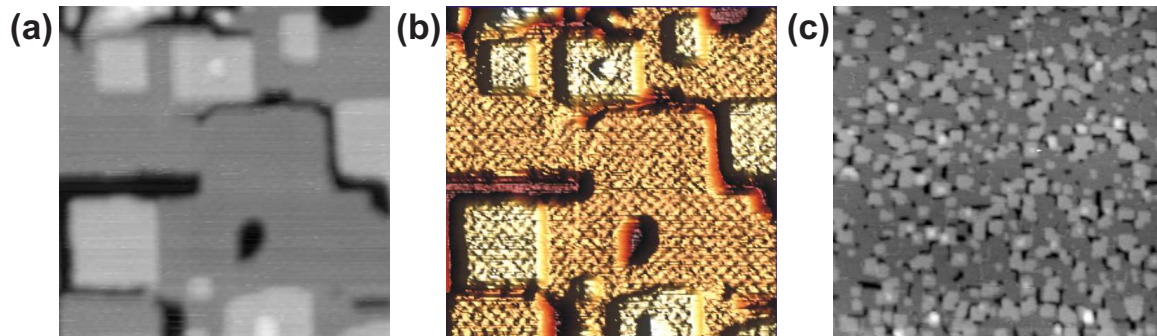


Figure 6.4: In an attempt to grow a complete flat layer of the superstructure we have explored different growth rates. Topography (a) and (b) three dimensional topographical image of the evaporation with a rate of $0.1 \text{ \AA}/\text{min}$. One can clearly observe the superstructure on the second and the third layer while small patches of the open NaCl substrate appear flat. (c) Evaporation with a higher rate of $1.8 \text{ \AA}/\text{min}$. Imaging parameters: (a)-(b) $200 \text{ nm} \times 200 \text{ nm}$, $f = 155.2 \text{ kHz}$, $\Delta f = -20.39 \text{ Hz}$ and (c) $400 \text{ nm} \times 400 \text{ nm}$, $f = 161.5 \text{ kHz}$, $\Delta f = -11 \text{ Hz}$.

In an attempt to grow a complete flat layer of the superstructure we have explored different growth rates and substrate temperatures. Evaporation of two full layers with a low rate of $0.1 \text{ \AA}/\text{min}$ does not result in a completed second layer, as shown by Fig. 6.4(a). The third monolayer continues to grow before the second monolayer is closed. In Fig. 6.4(b) one can clearly observe the superstructure on the second and the third layer while small patches of the open NaCl substrate appear flat. In this image a three dimensional topographical view was chosen in order to reveal the superstructure better. The same growth mode was observed for a higher evaporation rate, see Fig. 6.4(c). In order to promote the formation of a closed layer of the superstructure we have grown KBr films at a slightly elevated substrate temperature. Fig. 6.5(a) shows a film grown at the same conditions as the film shown in Fig. 6.4(a) except that the substrate was kept at 90°C during the evaporation. A similar density and size distribution of rectangular islands is found on a closed surface. These rectangular islands have monolayer height and are covered by an additional incomplete monolayer which exhibits an irregular, dendritic shape. Two interpretations of the result are possible: The closed surface below the rectangular islands is a complete double layer of KBr, the rectangular islands are part of the third layer comparable to the findings in Fig. 6.4(a) and the irregularly shaped layer is part of a fourth and fifth layer. Alternatively, the closed surface could be the NaCl substrate, and the islands part of the first and second layer of a reduced final coverage resulting from the elevated substrate temperature. The latter interpretation seems to be supported by the fact that we could not observe the superstructure under these growth conditions.

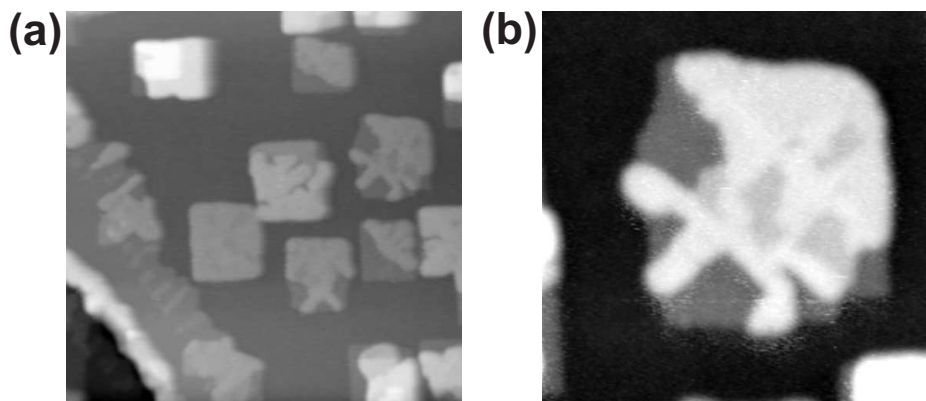


Figure 6.5: KBr film grown at the same conditions as the film shown in Fig. 6.4(a) except that the substrate was kept at 90°C during the evaporation. A similar density and size distribution of rectangular islands is found on a closed surface. These rectangular islands have monolayer height and are covered by an additional incomplete monolayer which exhibits an irregular, dendritic shape. (b) Shows such a dendritic island in detail. Imaging parameters: (a) $300\text{ nm} \times 300\text{ nm}$, $f = 154.9\text{ kHz}$, $\Delta f = -5\text{ Hz}$ and (b) $100\text{ nm} \times 100\text{ nm}$, $f = 154.9\text{ kHz}$, $\Delta f = -5\text{ Hz}$.

For the growth of KBr films at elevated temperature one has to consider the possibility of mixing of ionic species across the interface. Alkali halide crystals are well known for forming solid solutions. Such mixing adjust the average lattice constant and may support the formation of monolayer islands and dendritic structures of KBr as observed here.

It is important to note that the superstructure on top of the KBr islands deposited on NaCl is different in nature from the numerous observations of Moiré patterns in STM [177, 178] and transition electron microscopy (TEM) [179]. The Moiré pattern observed by STM on layered materials [180] and on thin films is related to the electronic structure [181] and modulation of the local work function [178]. The superstructure on the KBr islands is due to the spatial modulation of the atomic position [169, 182]. Duan et al. [174, 183] observed this superstructure by the use of helium atom scattering for the first time. They performed the measurements at 223 K. Our measurements show that this structure is also stable at room temperature. We could resolve the superstructure only on KBr films evaporated with a rate of $0.01\text{ \AA}/\text{min}$ leading to larger islands of an averaged side length of at least 13 nm. The averaged side length was only around 7 nm for higher rates, which corresponds to only about twice the periodicity of the superstructure. Such islands might be too small to build up a superstructure.

The corrugation of the superstructure measured by nc-AFM is about a factor ten higher than that calculated by Baker et al. [169] in their Monte Carlo simulations without including an AFM-tip and that Duan et al. measured by helium atom scattering [174]. The Monte Carlo simulations by Baker et al. revealed that the biggest amplitude of this superstructure is at the interface between these two materials, namely at the last substrate layer. On the KBr film itself the corrugation was found to be relatively weak. The effective corrugation observed in non-contact atomic force microscopy is given by the interplay of long- and short-range forces between the tip and the surface. On a clean KBr surface atomic corrugations up to 0.3-0.4 nm

can be observed [184]. A significant part of the enhanced atomic corrugation is probably due to the displacement of ions in the force field. In comparison, helium atom scattering measurements on a flat KBr surface revealed a corrugation of about 0.3 \AA [185], which is a factor ten smaller.

6.2.2 Heteroepitaxial Growth of NaCl on KBr(100)

Fig. 6.6(a) shows an overview image of the sub-monolayer growth of NaCl on an atomically flat KBr(100) surface. The substrate was held at room temperature during the evaporation of around 2/3 of a monolayer with the slower rate of $0.1 \text{ \AA}/\text{min}$. Islands of one monolayer height are homogeneously distributed over the surface. There is, however a significant difference in the growth mode between the two systems. The NaCl islands on KBr(100) have only monolayer height. Furthermore, their average size is larger at comparable evaporation rates.

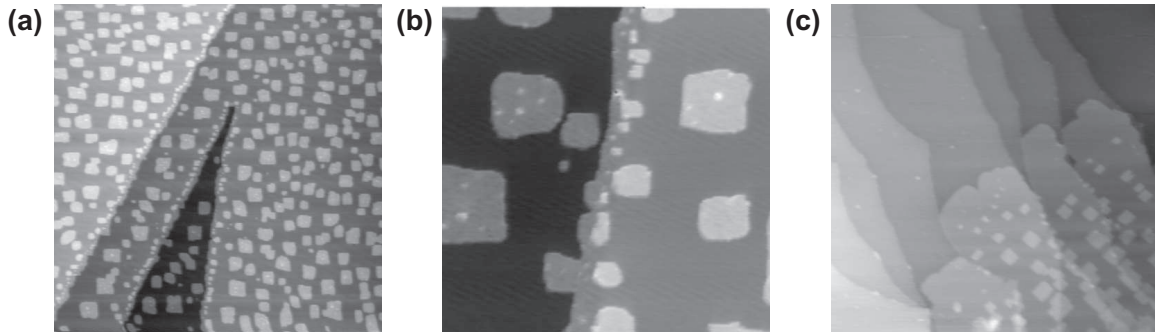


Figure 6.6: (a)-(b) NC-AFM images of the submonolayer growth of NaCl on KBr(100): Homogeneously distributed islands are found in contrast to the carpetlike growth of NaCl on Cu(100) in (c). A series of smaller NaCl islands decorates the substrate steps on the upper terraces. On the lower terrace the NaCl islands are directly attached to the substrate steps. Imaging parameters: (a) $1 \mu\text{m} \times 1 \mu\text{m}$, $f = 163.9 \text{ kHz}$, $\Delta f = -10 \text{ Hz}$ (b) $200 \text{ nm} \times 200 \text{ nm}$, $f = 163.9 \text{ kHz}$, $\Delta f = -13.1 \text{ Hz}$ and (c) $400 \text{ nm} \times 400 \text{ nm}$.

The size of the islands decreases towards the substrate steps. Fig. 6.6(a) and (b) show how a series of smaller NaCl islands decorates the substrate steps on the upper terraces. On the lower terrace the NaCl islands are directly attached to the substrate steps. No clear transition between the attached NaCl islands and the upper terrace of the KBr substrate can be recognized, not even in the atomic resolution image in Fig. 6.9(d). A complete stripe of NaCl seems to have grown along the substrate steps on the lower terrace. This conclusion is supported by the observation that the formerly straight substrate steps have an irregular appearance after evaporation of NaCl and by the finding that the series of smaller NaCl islands on the upper terrace have a distance of about 10 nm to the apparent substrate step. However, none of the NaCl islands is smoothly overgrowing a step. This is different from the carpet growth which has been observed in the growth of NaCl thin films on metallic and semiconductor substrates [160–165]. An example of a carpet growth is presented in Fig. 6.6(c) showing a NaCl thin film grown on a Cu(100) substrate. In the case of a carpet growth, the first layer grows in form of large islands with hundreds of nanometers side length (right lower half of the image),

smoothly covering substrate steps. The subsequent layers grow in form of smaller rectangular islands with tens of nanometers side length. These small islands tend to grow over the step.

A closer look into the NaCl islands reveals some growth irregularities, see Fig. 6.7(a). The island edges exhibit several kinks per island. On most islands a second layer starts to grow, and defects appear in some of the islands. A particular defect shown in the cross-section in Fig. 6.7(b) turns out to be a hole with the depth of the island height. These irregularities may be the result of the large strain in the islands or from a coalescence of smaller precursor islands.

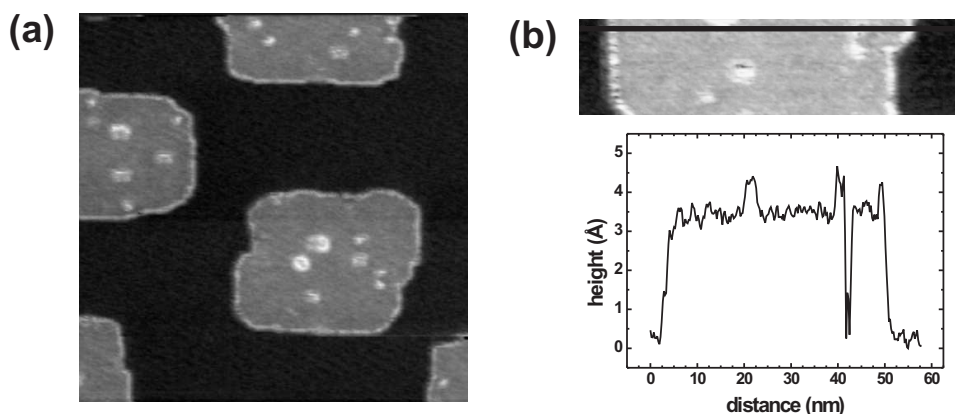


Figure 6.7: Details of NaCl islands grown on KBr(100). The island edges exhibit several kinks per island. During the evaporation the substrate was held at 25°C. The section in (b) reveals that there are small defects in the islands of image (a). Imaging parameters: (a) 100 nm \times 100 nm, $\Delta f = -17$ Hz.

The rectangular shape of the islands described so far is the result of a minimization of corner and kink sites in the island edges and documents how energetically unfavorable corner and kink sites are for these systems. The situation changes for NaCl island grown on KBr(100) at elevated temperature. Figure 6.8 shows the round shape of islands grown at a substrate temperature of 80° C. The images demonstrate that at these growth temperatures a minimization of the length of the island edge becomes more favorable than a minimization of the number of kinks and corners.

The atomic structure of the monolayer NaCl islands on KBr(100) has been investigated in some detail. The structure of both the substrate and an island are resolved in Fig. 6.9(a). The particular appearance of the step edge is a result of the convolution of the respective atomic structures of the tip apex and the step edge. While the immediate surrounding of the step is blurred by this effect, one can still recognize that the lattices of substrate and island have the same periodicity. A Fourier analysis (Fig. 6.9(b)) confirms that NaCl island and surrounding KBr substrate have the same lattice constant, which is within the experimental error identical to the lattice constant of the KBr(100) surface before growth of NaCl islands. We conclude that the ion-ion distance in the monolayer NaCl islands are enlarged to match the lattice of the KBr substrate. Fig. 6.9(c) illustrates the growth of NaCl on KBr. In agreement with this conclusion, no superstructure or dislocation network is observed on NaCl islands grown on

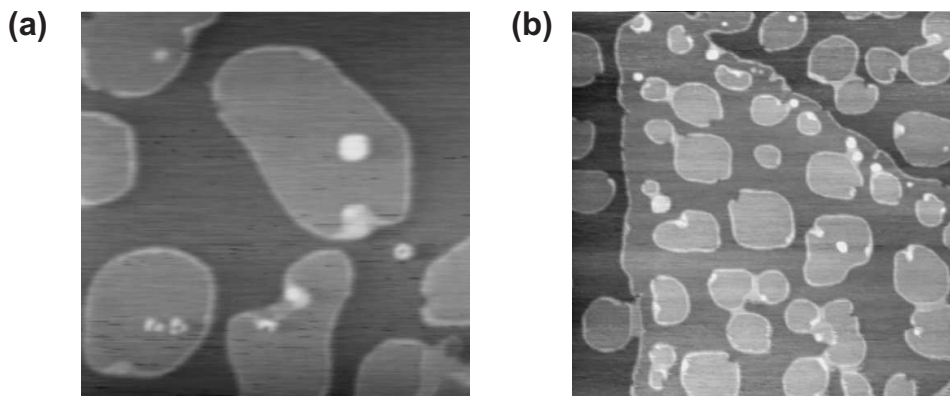


Figure 6.8: Sub-monolayer growth of NaCl on KBr(100) at 80° C substrate temperature. The round shape of the islands demonstrate that at these growth temperatures a minimization of the length of the island edge becomes more favorable than a minimization of the number of kinks and corners. (a) 200 nm \times 200 nm. (b) 500 nm \times 500 nm.

KBr(100). The adaption of the KBr(100) lattice by the islands has been confirmed in many atomically resolved images. One example is the NaCl island attached to a KBr substrate step in Fig. 6.9(d).

With increasing thickness of the NaCl films we would expect the lattice constant to change towards the bulk lattice constant of NaCl. Fig. 6.10(a) shows the KBr(100) surface after evaporation of approximately three layers of NaCl. The surface was held at room temperature during the evaporation and the rate was 0.1 Å/min. The surface appears rough compared to the complementary system discussed in section 6.2.1. Annealing flattens the surface significantly. Fig. 6.10(b) shows the same surface as in (a) after 90 minutes annealing at a temperature increasing from 60°C to 80°C. The first layer of NaCl seems now to be almost closed with only a few defects observed. Similar changes in topography upon annealing were observed for films of LiBr on KBr(100) and on LiF(100) by Goleck et al [186]. The authors attributed the changes to an Ostwald ripening which favors the growth of larger islands at the cost of smaller ones.

6.2.3 Discussion about the Different Growth Modes

In the last two sections, the initial stage of misfit accommodation at the interface between NaCl and KBr has been studied in real space by the atomic resolution capabilities of non-contact atomic force microscopy. For the case of sub-monolayer coverage of KBr deposited on NaCl(100), a superstructure was found on islands of two and three layers height. In the complementary system of NaCl deposited on KBr(100), flat islands of one monolayer height without any evidence for a superstructure or rumpling were observed. Atomically resolved nc-AFM images of the sub-monolayer coverage proved that the ion-ion distance in the monolayer high NaCl islands is enlarged to match the one of the KBr(100) substrate. In this section the different possibilities leading to such a different growth mode between these complementary systems are discussed.

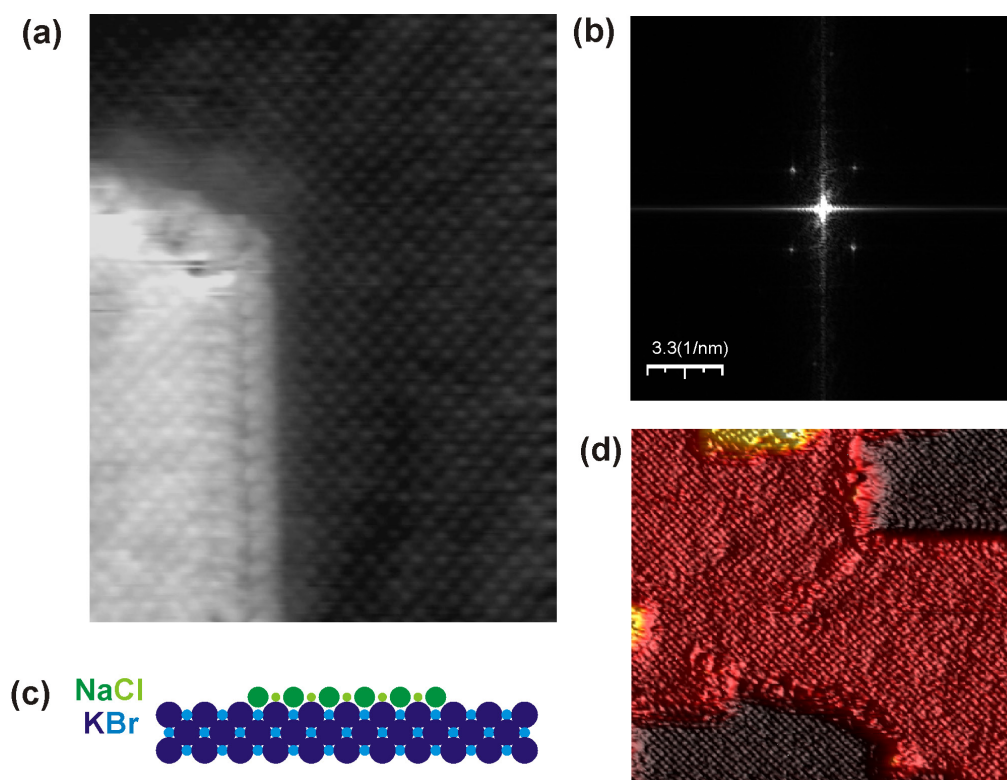


Figure 6.9: (a) Atomic resolution image showing a NaCl island and the KBr substrate ($15 \text{ nm} \times 19.6 \text{ nm}$). (b) A Fourier analysis over the entire image reveals the four folded symmetry of the rock salt structure. There is no split up of the main peaks suggesting different lattice constants for the film and the substrate. Moreover, there are no peaks indicating the existence of a superstructure. (c) Illustration of the proposed atomic arrangement showing that the ion-ion distance in the monolayer NaCl islands are enlarged to match the lattice of the KBr substrate. (d) Atomic resolution image of a NaCl island which grew on a step. A three dimensional topview was chosen in order to enhance the atomic contrast ($33 \text{ nm} \times 30 \text{ nm}$).

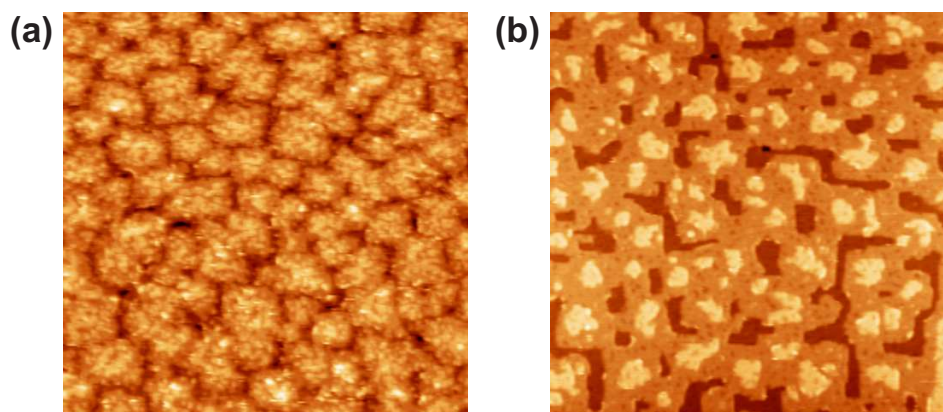


Figure 6.10: Growth of approximately three monolayers of NaCl on KBr(100) (a) before and (b) after 90 minutes annealing at a temperature increasing from 60° C to 80° C . The surface after evaporation appears rough. Annealing flattens the surface significantly. Image sizes: $500 \text{ nm} \times 500 \text{ nm}$.

Shluger et al. [182] discussed how the alkali halide clusters can accommodate the strain in their static calculations based on total-energy minimization for NaCl clusters at the MgO surface. They found that small planar clusters of around eleven molecules stabilize their structure by deforming perpendicular to the surface. They assume the same stabilization mechanism might be working for much larger clusters. Small three-dimensional clusters were found to deform strongly both parallel and perpendicular to the surface plane. In contrast to the simulations of Shluger et al., we could not observe any bending perpendicular to the surface on the planar NaCl islands on KBr(100). The amplitude of such a deformation might be too small to be resolved with atomic force microscopy. However, it is important to note that Shluger et al. studied a system with a positive misfit while NaCl on KBr has a negative misfit.

Natori et al. [171] have theoretically investigated the initial stage of heteroepitaxial growth KCl/KBr(001), which has a lattice mismatch of -4.7% . They found by means of energy minimization calculations that for their system strained layers (the lateral lattice constant of the film is that of the substrate) are more stable than pseudomorphic commensurate layers (the lateral lattice constant of the film is that of the film material) below the critical thickness of three atomic layers. This indicates that enlarged lattice constants rather than a rumpling might be a possible way of strain relaxation for negative misfit below a critical coverage.

Kiguchi et al. [173] described the differences between alkali halide systems with positive and negative misfit. They found that the lattice distortion relaxed more rapidly for the system with a positive misfit compared to the system with a negative misfit. The difference between the two cases was explained by the anharmonicity of ionic bonds, which makes the ionic bond easy to elongate but hard to contract. This might explain the different relaxation of NaCl/KBr and KBr/NaCl.

6.3. Contact Atomic Force Microscopy at the Resolution Limit

In the last section we have seen that strain relief in heteroepitaxial growth creates different surface structures depending on the lattice mismatch. High-resolution non-contact atomic force microscopy is a perfect tool to study such patterns and their underlying atomic structure in real space. In addition to the structure information, contact atomic force microscopy provides information on the local stiffness of the contact, the potential energy landscape of the surface, and frictional properties of the composite system. In the remaining part of this chapter, the influence of such structures on friction force microscopy imaging will be discussed in detail.

Fig. 6.11(a) shows the topography and (b) the lateral force map of a KBr double layer, deposited on NaCl(100) imaged with contact atomic force microscopy. We used the same evaporation conditions as for Fig. 6.4(a). The applied mean load for imaging was around -0.1 nN close to the jump-off-contact at -0.37 nN. These images confirm the existence of a superstructure on top of the KBr films as already found by nc-AFM. A Fourier analysis of this image verifies a superstructure periodicity of six nearest-neighbor distances of KBr. Surprisingly, this image reveals a small defect in the superstructure as indicated by the red arrow. It seems that none of the atoms is missing, but a couple of them are slightly elevated. The position of the atoms around the defect deviates from the perfect lattice and the atomic rows are slightly curved. Such curved atomic rows can also be observed to the right of the defect as marked

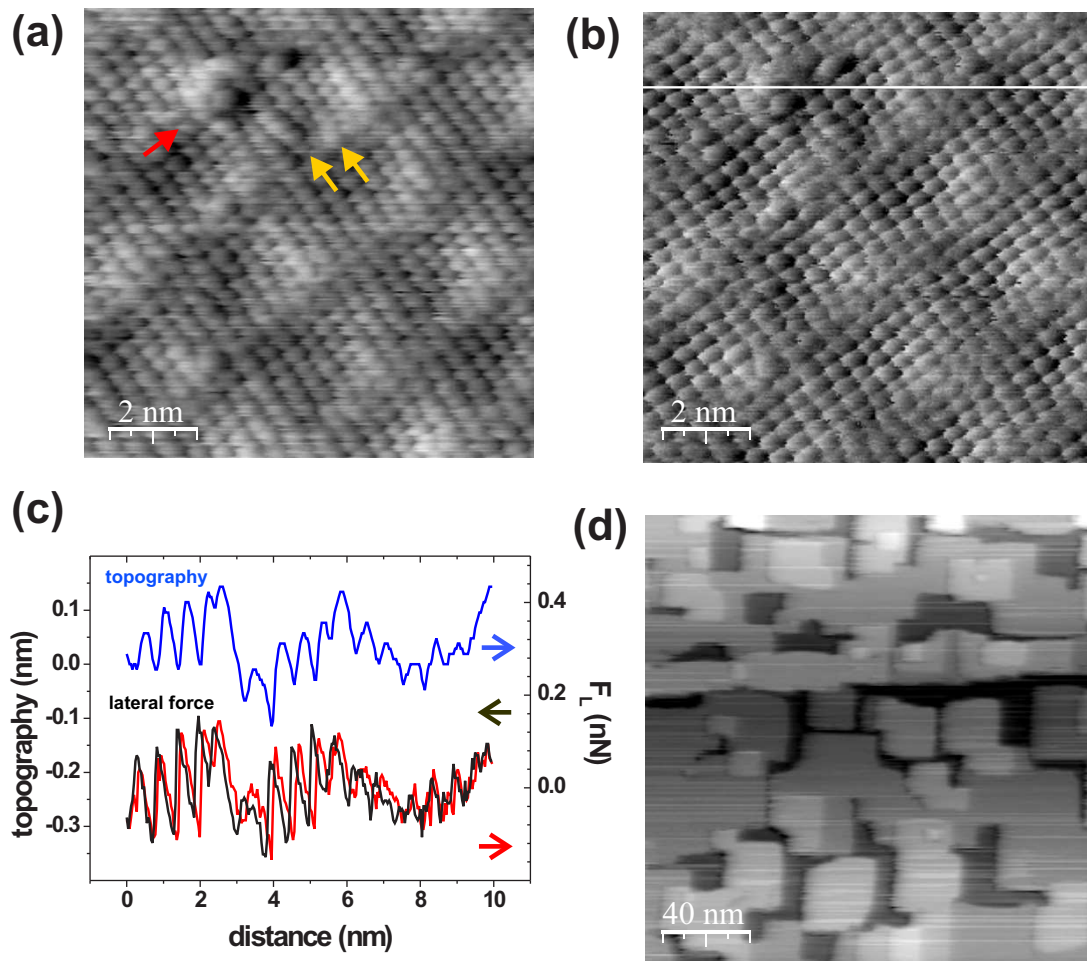


Figure 6.11: (a) Topography and (b) lateral force map of a KBr double layer, deposited on NaCl(100), showing a superstructure with atomic scale defects. Such an image confirms the high resolution capability of friction force imaging using a sharp tip and loads close to a ultralow friction state ($F_N = -0.1$ nN). A defect is marked by the red arrow. The yellow arrows point out irregular deformations of atomic rows. (c) Section across the defect. (d) Topographical overview of KBr islands on NaCl(100) in contact mode imaged with a load of $F_N = -0.26$ nN.

by the yellow arrows. These defects were imaged under stable conditions and reproduced over subsequent images in both topography and lateral force map. The section in Fig. 6.11(c) across the defect indicates that the stick phase is stretched over the defect. Apart from this defect, the modulated surface structure suggests a coherent interface, and there is no evidence for misfit dislocations.

It is important to note that it is very exceptional in contact mode imaging to distinguish single defects. Usually, contact mode images on the atomic scale show always a perfect symmetry without any defects and let therefore suggest that the atomic contrast in contact mode is a

convolution of the tip and surface structure and is only representing the periodicity of the surface. This is reasonable considering that in general the size of a contact between tip and surface presumably exceeds atomic dimensions. So far, there are only very few examples in literature suggesting that true atomic resolution is also possible in contact mode, i.e. reports on point defects on NaCl measured in air [57] and on LiF in UHV [58], resolved kinks on a 2H-NbSe₂ surface steps [59] and sublattice atom identification on NaF depending on the applied load [14]. In all these studies, it was concluded that the tip structure plays a major role and that the tip has to be very sharp. Therefore, we can assume that for the measurements described above the tip was very sharp and only a few atoms were involved in the contact. For blunter tips we were not able to image the superstructure with the same quality. The blunter the tip became, the more difficult it was to resolve the pattern, which supports the importance of a sharp tip.

Fig. 6.11(d) demonstrates that it was possible to image double and triple layer high KBr islands grown on the NaCl substrate on a larger scale without destroying or moving the film around, provided the load was of the order of a few nanonewtons close to the jump-off-contact. This allowed us to choose a suitable spot on the KBr film for atomic friction studies and to determine the thickness of the KBr film at that spot. In general, relative low loads were applied in this study preventing damage while scanning.

6.4. Atomic-Scale Stick-Slip on Top of KBr Films Grown on NaCl

In this section, we present a detailed analysis and discussion of atomic-scale stick-slip measurements on ultrathin KBr films, deposited on NaCl(100). Fig 6.12(a) shows the lateral force map and (d) the simultaneously recorded normal force map while scanning over the pattern on top of a double layer high KBr island for two different applied loads. The load was reduced from -0.01 nN to -0.32 nN after half of the image. The load in the lower half of the image is very close to the jump-off-contact of the lever, which was around -0.37 nN. All normal forces are given with respect to the unbent cantilever, negative normal forces refer to an up bending of the cantilever that partially compensates adhesion forces. The load in the lower part of the image is so small that the tip follows smoothly the atomic corrugation and no stick-slip instabilities occur as described by Socoliuc on a flat NaCl surface [20]. For this load the corrugation of the superstructure is very small and not apparent. In contrast, the lateral force maps imaged with a slightly higher load show strong variations of atomic friction along the pattern. The feedback on constant load was slow in this measurement to avoid any influence of the topography on the friction signal resulting in a constant height scan. All the topographic information is therefore represented in the normal force image in Fig. 6.12(d), which shows the error signal of the topographic feedback. The section in Fig. 6.12(e) along the indicated line shows that the change in load due to the slow feedback is only in the order of about 0.004 nN. However, the normal signal is very similar to the lateral force signal in Fig. 6.12(b) suggesting a coupling between the normal and lateral force.

The sections in Fig. 6.12(b) and (c) taken along the lines marked in the lateral force map represent typical lateral force signals as observed for these two applied loads. Section (d), imaged with the lower load close to the jump-off-contact, shows the atomic periodicity of the surface lattice, and only a faint variation of the superstructure along the pattern is buried in the weak

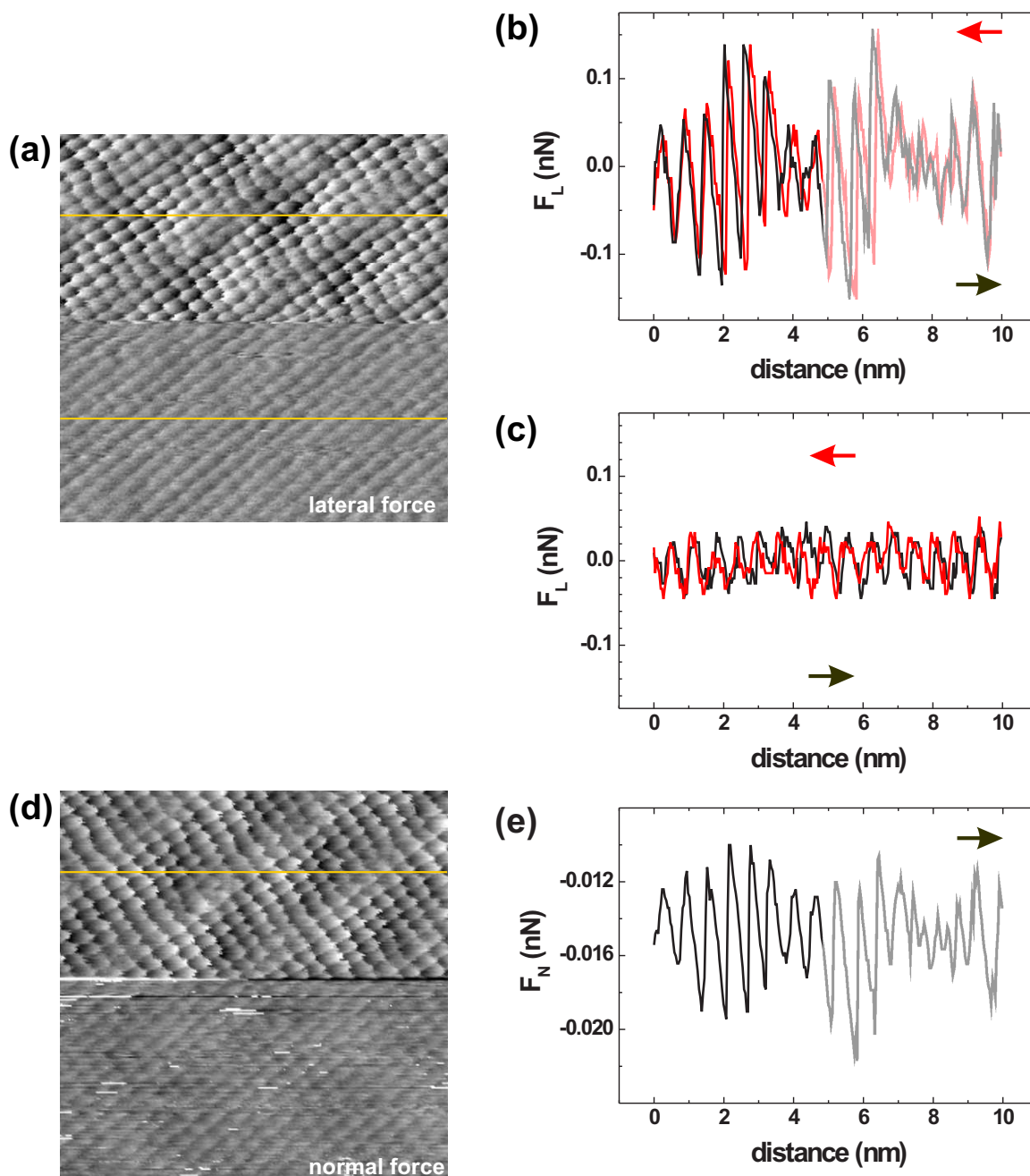


Figure 6.12: (a) Lateral and (d) normal force maps on KBr films grown on NaCl(100) showing strong variations of atomic scale friction due to small topographic undulations of the superlattice. The load was changed from -0.32 nN in the lower part of the image to -0.01 nN in the upper part. The superstructure is nearly invisible for small loads corresponding to a ultralow friction state. (b) and (c) show lateral force traces along the two lines marked in (a) corresponding to two different applied loads. Note that in (b) only about the first seven slips are along lines of maximal modulation of the lateral force. (e) Presents a section along the normal force suggesting that the load changes little while scanning in constant height over the pattern. The frame size in (a) and (d) is $10\text{ nm} \times 10\text{ nm}$. In (a) and (d) the background was subtracted line by line.

signal. The hysteresis loop, and with it the dissipation, disappears within the sensitivity of the experiment resulting in a perfect match of forward and backward scan. On the other hand, the section in Fig. 6.12(b) shows a beating pattern signaling a strong variation of the maximum lateral force. One has to note that only about the first seven slips are along lines of maximal modulation of the lateral force. Comparing the hysteresis loop of every single slip along the 6×6 unit cell, a transition from atomic-scale stick-slip in the middle of the unit cell to a smooth sliding of nearly perfect match between forward and backward scan at the edges of the unit cell is observed. In this smooth sliding state often referred as superlubricated or ultralow friction state no stick-slip instabilities occur. The lateral force signal in the ultralow friction part is nearly symmetric while in the stick-slip state an asymmetric sawtooth-like shape is observed. A zoom on the first part of the lateral force signal in forward direction only is shown in Fig. 6.14(a), where these different shapes of the individual slips in the lateral force signal are better recognizable. A similar transition from stick-slip to smooth sliding was observed on NaCl by Socoliuc et al. [20] by reducing the load. To elucidate whether a change in the local stiffness of the structure or a change in the energy barrier leads to such a beating pattern in the lateral force signal, these parameters will be calculated for each slip along the unit cell of the superstructure.

A one-dimensional Tomlinson model comprised of one spring which drags a point mass over the surface potential, describes several aspects of atomic-scale friction in agreement with experiments. Assuming a sinusoidal effective potential, the parameter η describes the relation between corrugation amplitude E_0 and the elastic energy stored in the spring

$$\eta = \frac{2\pi^2 E_0}{ka^2}. \quad (6.1)$$

It is known from the stability criterion explained in the introduction (compare chapter 1.2.1, Eq. (1.3)) that if $\eta < 1$ the movement is continuous and no hysteresis occurs, while for $\eta > 0$ stick-slip behavior is found [20]. To prove that the atomic-scale friction over the pattern is changing from a continuous smooth sliding to a stick-slip state, we have to determine the surface corrugation E_0 and the stiffness k , which combines the lateral stiffness of the contact and stiffness of the cantilever. Thus, we can estimate η for every single slip.

The corrugation of the surface potential E_0 is linearly related to the maximum lateral force F_L^{max} as shown in section 1.2.1

$$E_0 = \frac{a}{\pi} F_L^{max}. \quad (6.2)$$

This relation permits us to reconstruct the potential energy landscape from the experimental data by extracting all the F_L^{max} along a scan line. The experimentally determined slope k_{exp} differs for small η from k and has to be corrected accordingly [20]:

$$k = \frac{\eta + 1}{\eta} k_{exp}. \quad (6.3)$$

Substitution Eqs. (6.2) and (6.3) into the definition of η yields to

$$\eta = \frac{2\pi F_L^{max}}{k_{exp} a} - 1. \quad (6.4)$$

In this form η depends only on parameters which can be directly determined from the experimental data.

Fig. 6.13 summarizes the experimentally determined parameters E_0 , k and η using Eqs. (6.2), (6.3) and (6.4) across a single unit cell of the superstructure on these ultrathin KBr films grown on NaCl. In (a)-(c) the parameters for the lateral force signal in Fig. 6.12(b) and Fig. 6.14(a) are presented, which represents a typical lateral force signal along this superstructure. Fig. 6.13(d)-(f) show these three experimentally determined parameters for three different lines taken from the upper part of the lateral force map in Fig. 6.12(a). All the lateral force traces considered in this analysis were recorded along the [001]-direction when the tip was moving through the center of the apparent unit cells, i.e. along lines of maximal modulation of the lateral force. The F_{max} was determined for every slip by taking the mean of the minimum lateral force from the forward direction and the corresponding maximum lateral force from the backward direction. The measured slope of the sticking part k_{exp} is accurate to ± 0.05 N/m and the maximum lateral force to ± 0.01 nN. A constant lattice spacing $a = 0.66$ nm for the KBr film was used in the entire data analysis. In Monte Carlo simulations of this surface structure [169] the largest rumpling was found to occur in the topmost layer of the substrate and the double layer of KBr itself is only weakly corrugated, approaching the properties of the bulk material. Therefore the assumption of the bulk value for the lattice constant might be reasonable.

The beating shape of the lateral force signal across the unit cell of this superstructure shows that the maximum lateral force F_L^{max} is periodically changing. As a result the amplitude of the surface energy E_0 has to change within the superstructure in accordance to Eq. (6.2). Fig. 6.13 (a) and (d) indeed indicate a strong variation in the amplitude of the energy barrier between 0.06 eV and 0.17 eV for the applied load of -0.01 nN. The slope of the sticking part k_{exp} was varying between 0.26 N/m and 0.56 N/m. However, the spring constant k shows no clear tendency of a change along the structure. Finally, η was found to vary between 0.25 and 1.5 across the unit cell. This strengthens the hypothesized transition from the ultralow friction state to the stick-slip state across the unit cell of the superstructure.

Comparing the corrugation of the surface potential E_0 with the effective stiffness k in Fig. 6.13, we find that E_0 varies more strongly within one unit cell than k , which is nearly constant. This explains also the variation in the relation η between these two quantities E_0 and k . The change in the slope of the sticking part is therefore mainly associated with the variation for small values of η and is not related to a change in the local lateral stiffness of the structure. The fact that the effective stiffness is nearly constant is in agreement with the findings in chapter 3. It was found by means of a detailed analysis of the load dependence of the resonance in contact, that once the contact between the sharp tip and surface is formed the resonance curve does not shift when increasing loads further and therefore the contact stiffness does not change [187]. A nearly constant effective stiffness k was also observed by Socoliuc et al. in atomic friction measurements for different applied loads on NaCl [20].

The magnitude of the effective energy corrugation obtained in our measurements is in agreement to what has been reported in literature. Riedo et al. reported on the linear behavior of the energy barrier in friction measurements with the applied load on mica in ambient conditions [40] and values of $E_0 = 1$ to 2 eV. Socoliuc et al. found from atomic-scale friction measurements on NaCl energy barriers in the range of 0.1 to 0.5 eV depending on the applied load [20]. Recently, Schirmeisen et al. reported a barrier height of 48 meV on NaCl by three dimensional force mapping using non-contact atomic force microscopy [188]. Their measurement confirmed also a sinusoidal shape of the energy profile.

For a flat surface the corrugation E_0 is assumed to be constant. In our experiment E_0 is

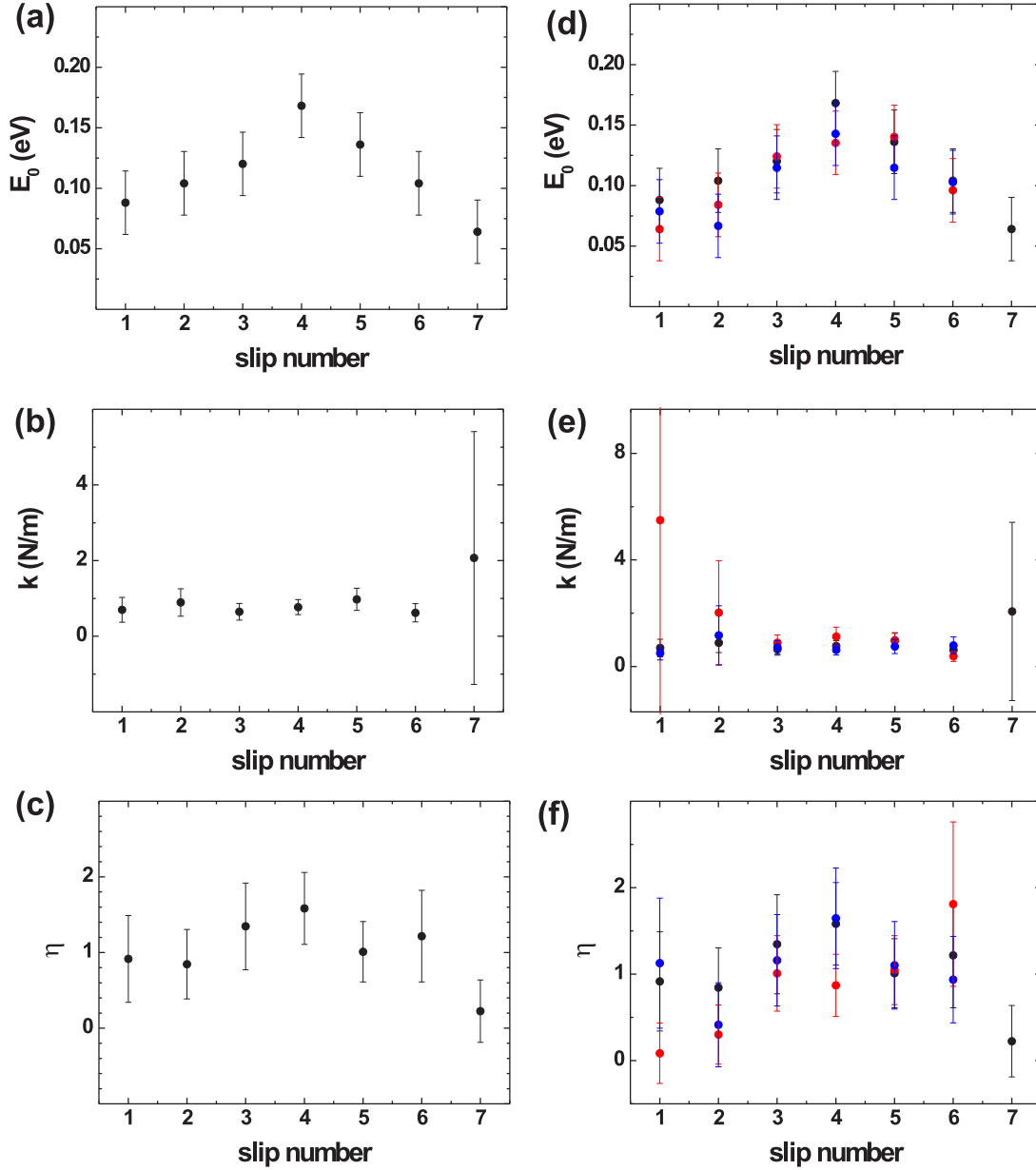


Figure 6.13: The amplitude of the energy barrier E_0 , the effective stiffness k and the parameter η measured for every slip along the 6×6 unit cell on the KBr-terminated superstructure: (a)-(c) show these three parameters along the first seven slips in Fig. 6.12(b). (d)-(f) represent the same parameters for three different sections from Fig. 6.12. Variations of the energy barriers between 0.06 to 0.17 eV are determined and a transition from atomic-scale stick-slip to smooth sliding within the unit cell is confirmed by the change in η from values below one to value larger than one. The effective spring constant does not suggest a clear tendency and can be assumed to be constant.

periodically oscillating around a mean potential barrier E_0^* and therefore the so far constant E_0 has to be replaced by

$$E_0 = E_0^* \left(\alpha \cos \left(\frac{2\pi x_{tip}}{b} \right) + 1 \right). \quad (6.5)$$

The parameter b describes the periodicity of the superstructure, and corresponds to $b = 6a$. The constant α defines a normalized amplitude of the E_0 -variation, and hence the range in which the parameter η changes. The parameter α was estimated from the experiment as $\alpha = 0.45$ with a mean potential corrugation of $E_0^* = 0.144$ eV for a load of -0.01 nN. These values fit to the upper part of Fig. 6.12, where the beating pattern due to the superstructure is observed. In conclusion the complete effective potential consisting of surface potential and spring potential can be written in the following form

$$V = -\frac{E_0^*}{2} \left(\alpha \cos \left(\frac{2\pi x_{tip}}{b} \right) + 1 \right) \cos \left(\frac{2\pi x_{tip}}{a} \right) + \frac{1}{2} k (x_{tip} - vt)^2. \quad (6.6)$$

The effective potential described in Eq. (6.6) is plotted in Fig. 6.14(d) using the parameters mentioned above without inclusion of the spring term. The corresponding η for this effective potential is shown in Fig. 6.14(e). The background color identifies the two states of stick-slip (yellow) and smooth sliding (white). Assuming a one-dimensional one-spring Tomlinson model the motion of the tip is described by Newton's equation

$$m\ddot{x}_{tip} + m\gamma\dot{x}_{tip} + \frac{\partial V}{\partial x_{tip}} = 0. \quad (6.7)$$

This equation of motion including the effective potential in Eq. (6.6) was numerically solved by means of a fourth-order Runge-Kutta method. For the simulations a scan velocity $v = 10$ nm/s matching the experimental one was used. For the effective spring constant a mean value $k = 0.75$ N/m was determined from the data set in Fig. 6.13(b). The following parameters were chosen for this simulation: an effective mass $m = 8 \cdot 10^{-13}$ kg, a sampling frequency $f = 10$ kHz and the time step of the simulation of 1 ns. These parameters are the same than already used in the last chapter. The result of the numerical simulation for a five times critically damped system is shown in Fig. 6.14(b). The shape of the beating pattern in the lateral force does not depend significantly on the damping of the contact springs. In Fig. 6.14(c) thermal fluctuations are included. For this purpose random noise $\xi(t)$ satisfying the fluctuation-dissipation relation $\langle \xi(t)\xi(t') \rangle = 2\gamma k_B T \delta(t - t')$ is added on the right side of the equation of motion in Eq. (6.7). The Langevin equation was solved with Ermak's algorithm as described in section 5.3.3. Otherwise the same parameters were used as in (a). For the above used parameter set no difference was observed for a five times critical damping and a 0.05 times underdamped system. In conclusion, the beat-like pattern is perfectly reproduced by simulations with and without thermal activation using a constant stiffness k and periodically oscillating E_0 . Hence, the simulations are in very good agreement with the experiment and represent the transition from a stick-slip state to a continuous sliding state.

Fig. 6.15(a) shows a topographical overview in contact mode of the complementary system of NaCl islands on KBr. Non-contact measurements of this system, indicated flat and well-ordered NaCl islands with an expanded lattice spacing to match the one of the KBr substrate. The lateral force map in (b) and the atomic friction loop measurements in (c) show regular stick-slip without a systematic variation of the maximum lateral force. Therefore the amplitude of the energy corrugation is constant. This confirms the hypothesis based on the non-contact measurements that these films are flat. Note the irregular features within the unit cell for this

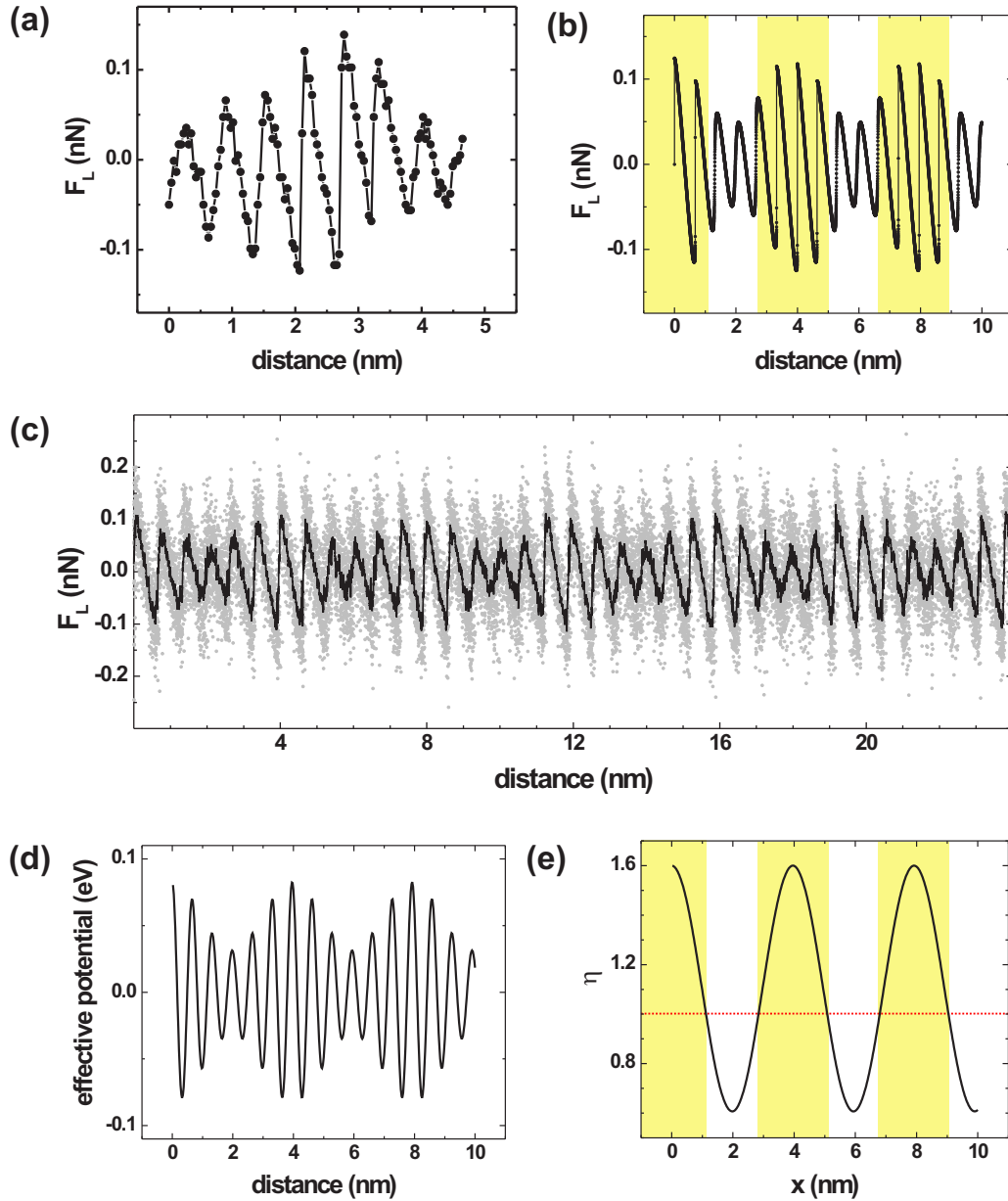


Figure 6.14: Comparison of the experimental measured lateral force with simulations based on a one-dimensional Tomlinson model comprised of one spring. (a) Typical measured lateral force along the 6×6 unit cell on top of the KBr thin films. (b) Numerical simulation with a Tomlinson model including a modulated energy corrugation but constant stiffness. The background color identifies the two states of stick-slip (yellow) and smooth sliding (white). (c) Numerical simulation with a Tomlinson model including a modulated energy corrugation and thermal effects ($T = 293\text{K}$). The grey dots represent the lateral force with thermal fluctuations sampled at 10 kHz and the black line is an average over 20 simulation points. (d) Effective potential without the spring term and (e) calculated η which was used for the simulations in (b) and (c).

measurement indicate a multiple contact. Hence it is unlikely to resolve a superstructure with such a tip.

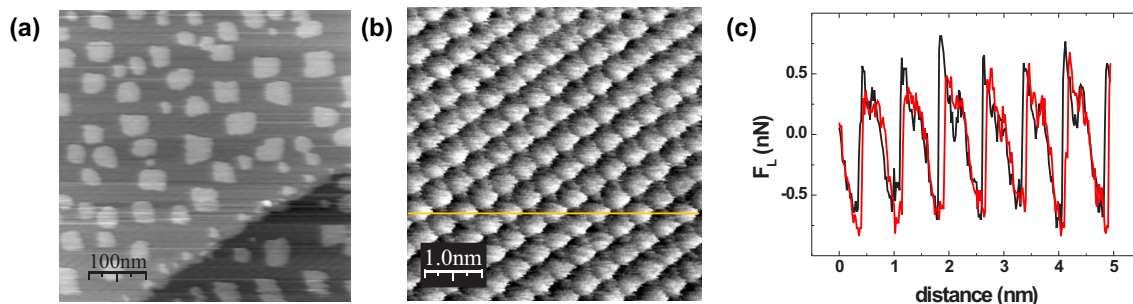


Figure 6.15: (a) Topographical overview in contact mode showing flat NaCl islands on KBr(100) ($F_N = 0.4$ nN). (b) Lateral force map on such a NaCl island suggests no superstructure. Note the irregular features within the unit cell indicate a multiple contact. Applied load: -0.4 nN. The friction loop in (c) shows atomic-scale stick-slip similar to a flat NaCl surface (red: forward, black: backward).

From the helium atom scattering measurements on the top of the KBr film by Duan et al. [174] and the Monte Carlo simulations by Baker et al. [169] one has to assume that the corrugation of this superstructure is rather weak of the order of 0.1 \AA . However, the effective corrugation felt by the tip is much larger as already observed in non-contact measurements. The observed disappearance of the long wavelength modulation of the superstructure while retaining lattice resolution in going from high to low load in Fig. 6.12 supports the idea, that the modulation is weak on the free sample but is enhanced when the tip is close to the sample. The variations of the energy barriers determined on these KBr-terminated surfaces demonstrate that chemically homogeneous surfaces can have significant variations of their atomic friction properties due to small structural inhomogeneities. Compared to a flat surface the coordination of the surface atoms is slightly changing along the pattern which might result in the observed changes in E_0 . Another possible explanation for the change in E_0 might be the difference in interactions felt by the tip on the top and in the valley of the pattern. Since we were able to resolve atomic-scale defects, we can assume to have a very sharp nanotip at the apex, which is smaller in size than the periodicity of the superstructure. The very end of the tip is then mainly sensitive to the atomic corrugation, whereas the change over the superstructure can be associated to a larger region of the tip apex, which experiences more interaction in the valley than on top of the structure. The effective contact size and interaction felt by the tip on top and in the valley of the structure would be different and lead to a change in E_0 . A comparison of the topography image with the lateral force map in Fig. 6.11 might suggest that the stick-slip pattern in the topographical valley is more pronounced than on top of this superstructure. However, the topography can be influenced by the lateral force. Also the normal force in Fig. 6.12(d), which is the error signal of the topographic feedback as the tip is moving at constant height, follows strongly the lateral force and hence suggesting a coupling between normal force and lateral force.

The Tomlinson model comprised of a single spring pulling a mass along a sinusoidal potential surface has described atomic friction phenomena like load dependence [20] as well as temperature and velocity dependence, and the distribution of jump forces [26] by including thermal effects. In chapter 4 it was shown that the experimental situation is not well represented, since a one-spring model cannot reproduce both the resonance frequency of the cantilever, and the experimentally found lateral stiffness which is dominated by the contact. Nevertheless, the above mentioned simulations and the ones presented in this section use both a single-spring model and are in agreement with the experiments. The capability of resolving a single defect confirms that the contact was very small and multiple contacts can be excluded. The extension of the Tomlinson model discussed in this chapter is similar to the extension described in chapter 5, where the energy barrier was modulated in time. In these simulations here the barrier is modulated in space. But it is important to note that the modulation in space is quasi-static and not dynamic. Moreover, the parameter α depends on the structure and the applied load in this chapter and cannot be switched on and off in the same way than described in the last chapter.

The potential energy landscape of the surface governs not only atomic friction, but it determines also the diffusion of adsorbed molecules and is responsible for dynamic surface processes such as growth and catalytic action. The experimentally determined energy barriers are directly correlated to diffusion energy barriers. However, the absolute values cannot be directly compared, because the influence of long range forces between the tip and the surface are not known. If the change in the modulated energy barrier is large enough, these surface structures on insulators are promising candidates as templates for self assembly of adsorbates, i.e. molecules or particles, or anisotropic catalysis. Such nanostructured surfaces are especially of importance on insulators because molecules are in general quite mobile on insulating surfaces and need to be trapped at steps or pits [83, 189] in order to be imaged. Many examples of Moiré patterns on metals are known as candidates for periodic diffusion anisotropies giving rise to be an ideal substrate to grow island networks [155, 190, 191]. The structure presented here is an interesting insulating candidate.

An interesting observation is found in the normal force image in Fig. 6.12(c). In this measurement the controller was almost switched off to avoid any influence on the friction signal. All the topographic information is therefore represented in the normal force image. In the ultralow friction state (lower part of the image), the normal force map shows stripes along one scanline indicating some instabilities where the tip is lifted up for a short moment. These stripes were not observed while scanning in the stick-slip regime (upper part of the image). The height of these instabilities are all comparable. Similar stripes were observed in the topography of non-contact measurements and may interpreted as mobile KBr monomers which are not attached to an island. This observation shows that imaging in contact mode in the ultralow friction state needs to be further investigated, in order to completely understand such details.

6.5. Conclusions

Ultrathin epitaxial films of KBr on NaCl(100) and NaCl on KBr(100) have been grown to study the surface structure produced by the large strain due to a lattice mismatch of 17%. In the first part of this chapter images of these films in real space using non-contact atomic force microscopy are shown. For the case of sub-monolayer coverage of KBr on NaCl(100),

a superstructure was found on islands of two and three layers height. In the complementary system, NaCl on KBr(100), flat islands without any superstructure or rumpling were observed. Atomically resolved non-contact images of the sub-monolayer coverage proved that the lattice constant of the NaCl islands is elongated to match the one of KBr(100). The differences in growth of the two systems can be ascribed to the anharmonicity of ionic bonds, which make the ionic bond easy to elongate but hard to contract. Friction force measurements on these thin KBr films on NaCl revealed transitions from atomic-scale stick-slip to the smooth sliding within the unit cell of the superstructure. An explanation was found in the framework of a Tomlinson model by a variation of the energy barriers along the unit cell which is in agreement with the measurements. Scans across atomic scale defects confirmed the high resolution capabilities of friction force microscopy close to an ultralow friction state.

Conclusions and Outlook

In this thesis several aspects of contact dynamics from the atomic scale to nanostructured surfaces were analyzed and discussed based on results from atomic force microscopy in ultrahigh vacuum. These studies involved high temporal resolution measurements of thermal fluctuations of the force sensor in contact, measurements of the slip duration in atomic-scale stick-slip, and atomic friction measurements on ultrathin heteroepitaxial films on alkali halides. Alkali halides provide model systems for atomic friction measurements and heteroepitaxial growth studies on insulators because of their simple structure, the large range of lattice constants and the comparatively simple preparation. Moreover, different simulations based on a one-dimensional Tomlinson model provided explanations for several experimental observations.

In **chapter 3** the influence of the tip-sample contact on the thermal fluctuations of the force sensor and on the dynamics of the stick-slip process were characterized. Thermal fluctuations of the cantilever which have a strong impact on the atomic stick-slip process were found to be strongly damped through the tip-sample contact. Using the frequency shift of the resonance in contact as a measure for the contact stiffness with different applied loads, a power spectrum analysis suggested that the contact stiffness remains constant for the sharp tip and only changes for micrometer-sized spherical tips. In a continuum mechanics approach we expect the lateral stiffness to increase with load proportional to the contact area. Hence, these measurements demonstrate the breakdown of continuum models at the nanometer scale for the contact stiffness. By modeling the experiment with a two spring model, one representing the cantilever force sensor and one the compliant tip-sample contact, a consistent description of the lateral contact stiffness and quality factor upon contact formation in lateral force measurements has been achieved.

The atomic-scale stick-slip process has attracted a lot of attention since it can be seen as an elementary friction mechanism. The occurrence of the stick-slip behavior is one-to-one related to energy loss in the sliding process. Measurements of the stick-slip movement of the force microscope tip with high bandwidth have been presented in **chapter 4**. They revealed a wide variation of slip durations up to several milliseconds which is far longer than expected for a relaxation process on atomic scale. Such long slip events were believed to be the consequence of a multiple contact between tip and surface. This conclusion was drawn from a correlation between irregular features in lateral force maps and long slip durations. Moreover, a comparison of our experimental results with a multiple-tip simulation based on a Tomlinson model including thermal activation supports this hypothesis. These findings show that the slip duration can be seen as a measure of the contact shape.

Over the past years, several mechanisms to reduce friction have been suggested. However, most of them cannot be easily applied in practical situations and do not allow for fast switching between ultralow and high friction states. Recently, an efficient way to switch friction on

and off at the atomic scale has been achieved by exciting the mechanical resonances of the sliding system in a direction perpendicular to the contact plane [53]. In order to obtain better understanding of the atomic scale control of friction by actuation an extended one-dimensional Tomlinson model was discussed in detail in **chapter 5**. This model allowed us to understand how the tip is moving along the surface potential. This led us to an analytical approximation for the residual friction force which is in good agreement with numerical simulations. Moreover the simulations suggest that in a sufficiently underdamped system not only the friction but also the energy loss is dramatically minimized compared to the static case. This effects could be useful in efforts to develop micro- and nanoelectromechanical systems (MEMS/NEMS) that do not tolerate lubrication.

The heteroepitaxy of alkali halide crystals provides model systems for studying strain relief structures on insulators because of the large range of lattice constants. Ultrathin epitaxial films of KBr on NaCl(100) and NaCl on KBr(100) have been grown to study the surface structure caused by a lattice mismatch of 17%. In **chapter 6** images of these films in real space using non-contact atomic force microscopy are shown. For the case of sub-monolayer coverage of KBr on NaCl(100), a superstructure was found on islands of two and three layers height. In the complementary system, NaCl on KBr(100), flat islands without any superstructure or rumpling were observed. Atomically resolved non-contact images of the sub-monolayer coverage prove that the lattice constant of the NaCl islands is elongated to match the one of KBr(100). The differences in growth of the two systems can be ascribed to the anharmonicity of ionic bonds, which make the ionic bond easy to elongate but hard to contract. Friction force measurements on these thin KBr films on NaCl revealed transitions from atomic-scale stick-slip to the smooth sliding within the unit cell of the superstructure. An explanation was found in the framework of a Tomlinson model by a variation of the energy barriers along the unit cell which is in agreement with the measurements. Scans across atomic scale defects confirm the high resolution capabilities of friction force microscopy close to an ultralow friction state. This suggests that scanning in a ultralow friction state may also be very promising as a future imaging technique.

The superstructure formed by the large strain showed interesting properties in themselves. If the change in the modulated energy barrier is large enough, such surface structures are promising candidates as templates for ordered island growth or the self assembly of adsorbates, i.e. molecules or particles. Recently, several examples of Moiré patterns on metals have been shown to be an ideal substrate to grow island networks [155, 190]. On insulators such structures are especially important because molecules are in general very mobile and need to be trapped at steps or pits in order to be imaged.

Acknowledgments

My PhD has been an inspiring, exciting, sometimes challenging, but always very interesting experience. It has been made possible by the many people who have supported me and I would like to thank them all very much.

First, I am very grateful to my supervisor Prof. Ernst Meyer who has given me the chance to participate in several interesting research projects and attend various international conferences.

A very special thanks goes out to Prof. Roland Bennewitz. My one year stay in Montreal in his research group was one of the highlights of my PhD. The time in Montreal was very motivating and I enjoyed the experience very much. Thank you for your support of my thesis as well as for many helpful discussions and valuable advice in the interpretation of the measurements. Moreover, I am grateful for your assistance in writing papers.

I would like to thank Prof. Alexis Baratoff for his theoretical support, enlightening discussions and encouraging comments with his impressive knowledge.

I am grateful to Dr. Yi Sang for providing me with the code to perform simulations on the two-spring model described in chapter 4.

It was a pleasure for me to work with all the friendly people in the lab. Many thanks to all the current and former group members for all their help, friendship and their familial atmosphere in the lab. These are: Dr. Oliver Pfeiffer, Dr. Adrian Wetzel, Dr. Anisoara Socoliuc, Dr. Laurent Nony, Dr. Enrico Gnecco, Dr. Thilo Glatzel, Dr. Sacha Schär, Lars Zimmerli, Akshata Rao, Dr. M. Schönenberger, and Dominique Schär from the University of Basel and Tobin Filleter, Patrick Delage, Jonathan David, Paris Hubbard-Davis, and Ben Drevniok from McGill University.

A special thank goes to everybody of the mechanical and electronic workshop: A. Tonin, R. Maffiolini, Dr. h.c. H.-R. Hidber, J. Sylvester, H. Breitenstein, E. Del Campo, S. Kecani deserve special mention. I would like to acknowledge Verena Thommen for the SEM images of the AFM-tips. I am grateful to the secretaries for helping me with administrative things and for assisting me in many other different ways. G. Weaver, B. Kammermann, A. Kalt, and E. Shearon deserve special mention.

I am particularly grateful to everybody who was so kind to read parts of the manuscript and correct the English spelling and grammar. Special thanks to Dr. Oliver Pfeiffer, Dr. Adrian Wetzel, Dr. Enrico Gnecco, Prof. Alexis Baratoff, and Dr. Stuart Whitehouse.

I would like to thank also Carla Fröhlich and Ute Deyer for the tea break conversations which have enriched my daily life in the department.

Finally, I would like to thank my parents and my brother for their continuous support during my study and my PhD.

For financial support, I would like to acknowledge the Swiss National Science Foundation.

Bibliography

- [1] G. Binnig and H. Rohrer. Scanning tunneling microscopy. *Helv. Phys. Acta*, 55: 726–735, 1982.
- [2] G. Binnig, C.F. Quate, and Ch. Gerber. Atomic force microscopy. *Phys. Rev. Lett.*, 56(9):930–933, 1986.
- [3] G. Meyer and N.M. Amer. Novel optical approach to atomic force microscopy. *Appl. Phys. Lett.*, 12:1045–1047, 53.
- [4] D. Rugar, H.J. Mamin, and P. Gütthner. Improved fiber optic interferometer for atomic force microscopy. *Appl. Phys. Lett.*, 55:2588, 1989.
- [5] M. Tortonese, R.C. Barrett, and C.F. Quate. Atomic resolution with an atomic force microscope using piezoresistive detection. *Appl. Phys. Lett.*, 62: 834, 1993.
- [6] C.M. Mate, G.M. McClelland, R. Erlandsson, and S. Chiang. Atomic-scale friction of a tungsten tip on a graphite surface. *Phys. Rev. Lett.*, 59(17):1942–1945, 1987.
- [7] S. Fujisawa, Y. Sugawara, S. Ito, S. Mishima, T. Okada, and S. Morita. The two-dimensional stick-slip phenomenon with atomic resolution. *Nanotechnology*, 4(3):138–142, 1993.
- [8] S. Morita, S. Fujisawa, and Y. Sugawara. Spatially quantized friction with a lattice periodicity. *Surf. Sci. Rep.*, 23 (1):1–41, 1996.
- [9] J. Kerssemakers. Atomic force microscopy imaging of transition metal layered compounds: A two-dimensional stickslip system. *Appl. Phys. Lett.*, 67: 347–9, 1995.
- [10] R. Lüthi, E. Meyer, L. Howald, M. Bammerlin, H.-J. Güntherodt, T. Gyalog, and H. Thomas. Friction Force Microscopy in Ultrahigh Vacuum: An Atomic-Scale Study on KBr(001). *Tribology Letters*, 1:129, 1995.
- [11] R. Bennewitz, E. Gnecco, T. Gyalog, and E. Meyer. Atomic friction studies on well-defined surfaces. *Tribology Letters*, 10:51, 2001.
- [12] E. Gnecco, R. Bennewitz, T. Gyalog, Ch. Loppacher, M. Bammerlin, E. Meyer, and H.J. Güntherodt. Velocity dependence of atomic friction. *Phys. Rev. Lett.*, 84:1172, 2000.
- [13] R.W. Carpick, Q. Dai, D.F. Ogle-tree, and M. Salmeron. Friction force microscopy investigations of potassium halide surfaces in ultrahigh vacuum: Structure, friction and surface modification. *Tribology Letters*, 5(1):91–102, 1998.

- [14] M. Ishikawa, S. Okita, N. Minami, and K. Miura. Load dependence of lateral force and energy dissipation at NaF(001) surface. *Surface Science*, 445(2):488–494, 2000.
- [15] R. Bennewitz, T. Gyalog, M. Guggisberg, M. Bammerlin, E. Meyer, and H.-J. Güntherodt. Atomic-scale stick-slip processes on Cu(111). *Phys. Rev. B*, 60:R11301, 1999.
- [16] M.R. Sørensen, K.W. Jacobsen, and P. Stoltze. Simulations of atomic-scale sliding friction. *Phys. Rev. B*, 53:2101–2113, 1996.
- [17] M. Enachescu, R.W. Carpick, D. F. Ogletree, and M. Salmeron. The role of contaminants in the variation of adhesion, friction, and electrical conduction properties of carbide-coated scanning probe tips and Pt(111) in ultrahigh vacuum. *J. Appl. Phys.*, 95(12):7694–7700, 2004.
- [18] L. Howald, R. Lüthi, E. Meyer, and H.-J. Güntherodt. Atomic-Force Microscopy on the Si(111)7×7 Surface. *Phys. Rev. B*, 51:5484, 1995.
- [19] G.A. Tomlinson. *Philos. Mag. Ser.*, 7: 905, 1929.
- [20] A. Socoliuc, R. Bennewitz, E. Gnecco, and E. Meyer. Transition from stick-slip to continuous sliding in atomic friction: Entering a new regime of ultralow friction. *Phys. Rev. Lett.*, 92(13):134301, 2004.
- [21] S. Medyanik, W.K. Liu, I.-K. Sun, and R.W. Carpick. Predictions and observations of multiple slip modes in atomic scale friction. *Phys. Rev. Lett.*, 97: 136106, 2006.
- [22] J. Nakamura, S. Wakunami, and A. Natori. Double-slip mechanism in atomic-scale friction: Tomlinson model at finite temperatures. *Phys. Rev. B*, 72:235415, 2005.
- [23] S. Fujisawa, E. Kishi, Y. Sugawara, and S. Morita. Two-dimensionally discrete friction on the NaF(100) surface with the lattice periodicity. *Nanotechnology*, 6(1):8–11, 1995.
- [24] S. Fujisawa, K. Yokoyama, Y. Sugawara, and S. Morita. Analysis of experimental load dependence of two-dimensional atomic-scale friction. *Phys. Rev. B*, 58(8):4909–4916, 1998.
- [25] H. Hölscher, U.D. Schwarz, and R. Wiesendanger. Modelling of the scan process in lateral force microscopy. *Surface Science*, 375:395–402, 1997.
- [26] Y. Sang, M. Dube, and M. Grant. Thermal effects on atomic friction. *Phys. Rev. Lett.*, 87:174301, 2001.
- [27] A. Schirmeisen, L. Jansen, and H. Fuchs. Tip-jump statistics of stick-slip friction. *Phys. Rev. B*, 71:245403, 2005.
- [28] E. Gnecco, R. Bennewitz, T. Gyalog, and E. Meyer. Friction experiments on the nanometre scale. *J. Phys. C: Solid State Phys.*, 13:R619R642, 2001.
- [29] K.L. Johnson. *Contact Mechanics*. Cambridge University Press, Cambridge, United Kingdom, 1985.
- [30] B. Luan and M.O. Robbins. The breakdown of continuum models for mechanical contacts. *Nature*, 435:929, 2005.
- [31] R.W. Carpick, F.D. Ogletree, and M. Salmeron. A general equation for fitting contact area and friction vs load measurements. *Journal of Colloid and Interface Science*, 211:395–400, 1999.

- [32] U.D. Schwarz. A generalized analytical model for the elastic deformation of an adhesive contact between a sphere and a flat surface. *Journal of Colloid and Interface Science*, 261:99–106, 2003.
- [33] B. V. Derjaguin, V. M. Mueller, and Yu. P. Toporov. Effect of contact deformations on the adhesion of particles. *Journal of Colloid and Interface Science*, 53(2):314–326, 1975.
- [34] D. Maugis. Adhesion of spheres: The JKR-DMT transition using a dugdale model. *Journal of Colloid and Interface Science*, 150(1):243–269, 1992.
- [35] R. Lüthi, E. Meyer, M. Bammerlin, L. Howald, H. Haefke, T. Lehmann, C. Loppacher, and H.-J. Güntherodt. Friction on the Atomic Scale: An Ultra-high Vacuum Atomic Force Microscopy Study on Ionic Crystals. *J. Vac. Sci. Technol. B*, 14:1280, 1996.
- [36] E. Gnecco, R. Bennewitz, and E. Meyer. Abrasive wear on the atomic scale. *Phys. Rev. Lett.*, 88:215501, 2002.
- [37] A. Socoliuc, E. Gnecco, R. Bennewitz, and E. Meyer. Ripple formation induced in localized abrasion. *Phys. Rev. B*, 68:115416, 2003.
- [38] T. Bouhacina, J.P. Aime, S. Gauthier, D. Michel, and V. Heroguez. Tribological behavior of a polymer grafted on silanized silica probed with a nanotip. *Phys. Rev. B*, 56:7694, 1997.
- [39] S. Sills and R.M. Overney. Creeping friction dynamics and molecular dissipation mechanisms in glassy polymers. *Phys. Rev. Lett.*, 91:095501, 2003.
- [40] E. Riedo, E. Gnecco, R. Bennewitz, E. Meyer, and H. Brune. Interaction potential and hopping dynamics governing sliding friction. *Phys. Rev. Lett.*, 91(8):084502, 2003.
- [41] P. Reimann and M. Evstigneev. Non-monotonic velocity dependence of atomic friction. *Phys. Rev. Lett.*, 93(23):230802, 2004.
- [42] P. Reimann and M. Evstigneev. Description of atomic friction as forced Brownian motion. *New Journal of Physics*, 7:25, 2005.
- [43] M. Evstigneev and P. Reimann. Refined force-velocity relation in atomic friction experiments. *Phys. Rev. B*, 73:113401, 2006.
- [44] E. Riedo, F. Levy, and H. Brune. Kinetics of capillary condensation in nanoscopic sliding friction. *Phys. Rev. Lett.*, 88:185505, 2002.
- [45] Y.-Z. Hu and S. Granick. Microscopic study of thin film lubrication and its contributions to macroscopic tribology. *Tribology Letters*, 5(1):81–88, 1998.
- [46] M. Hirano, K. Shinjo, R. Kaneko, and Y. Murata. Observation of superlubricity by scanning tunneling microscopy. *Phys. Rev. Lett.*, 78(8):1448–1451, 1997.
- [47] M. Hirano. Atomistic locking and friction. *Phys. Rev. B*, 41(17):11837–11851, 1990.
- [48] M. Hirano. Superlubricity: A state of vanishing friction. *Wear*, 254:932–940, 2003.
- [49] M.H. Müser. Structural lubricity: Role of dimension and symmetry. *Europhys. Lett.*, 66(1):97–103, 2004.
- [50] M. Dienwiebel, G.S. Verhoeven, N. Pradeep, J.W.M. Frenken, J.A. Heimberg, and H.W. Zandbergen. Superlubricity of graphite. *Phys. Rev. Lett.*, 92(12):126101, 2004.

- [51] M. Dienwiebel, N. Pradeep, G.S. Verhoeven, H.W. Zandbergen, and J.W.M. Frenken. Model experiments of superlubricity of graphite. *Surface Science*, 576:197–211, 2005.
- [52] S.Yu. Krylov, K.B. Jinesh, H. Valk, M. Dienwiebel, and J.W.M. Frenken. Thermally induced suppression of friction at the atomic scale. *Phys. Rev. E*, 71(6):65101 – 1, 2005.
- [53] A. Socoliuc, E. Gnecco, S. Maier, O. Pfeiffer, A. Baratoff, R. Bennewitz, and E. Meyer. Atomic-scale control of friction by actuation of nanometer-sized contacts. *Science*, 313:207–210, 2006.
- [54] F.J. Giessibl, M. Herz, and J. Mannhart. Friction traced to the single atom. *Proc. Natl. Acad. Sci. USA*, 99(19):12006–12010, 2002.
- [55] G. Binnig, Ch. Gerber, E. Stoll, T.R. Albrecht, and C.F. Quate. Atomic resolution with atomic force microscopy. *Europhys. Lett.*, 3(12):1281–1286, 1987.
- [56] L. Howald, H. Haefke, R. Lüthi, E. Meyer, G. Gerth, H. Rudin, and H.-J. Güntherodt. Ultrahigh-Vacuum Scanning Force Microscopy: Atomic-Scale Resolution at Monatomic Cleavage Steps. *Phys. Rev. B*, 49:5651, 1994.
- [57] A.L. Shluger, R.M. Wilson, and R.T. Williams. Theoretical and experimental investigation of force imaging at the atomic scale on alkali halide crystals. *Phys. Rev. B*, 49(7):4915–4930, 1994.
- [58] M. Ohta, T. Konishi, Y. Sugawara, S. Morita, M. Suzuki, and Y. Enomoto. Observation of atomic defects on LiF(100) surface with ultrahigh vacuum atomic force microscope. *Jap. J. Appl. Phys.*, 32(6B):2980–2982, 1993.
- [59] Th. Schimmel, Th. Koch, J. Küppers, and M. Lux-Steiner. True atomic resolution under ambient conditions obtained by atomic force microscopy in contact mode. *Appl. Phys. A*, 68:399–402, 1999.
- [60] F.J. Giessibl. Atomic resolution of silicon(111)7x7 by atomic force microscopy through repulsive and attractive forces. *Science*, 267(68):1451–1455, 1995.
- [61] Y. Sugawara, M. Ohta, H. Ueyama, and S. Morita. Defect motion on an inp(110) surface observed with non-contact force microscopy. *Science*, 270:146, 1995.
- [62] Y. Martin, C.C. Williams, and H.K. Wickramasinghe. Atomic force microscope-force mapping and profiling on a sub 100-Å scale. *J. Appl. Phys.*, 61(10):4723–4729, 1987.
- [63] T.R. Albrecht, P. Grütter, D. Horne, and D. Rugar. Frequency modulation detection using high-Q cantilevers for enhanced force microscope sensitivity. *J. Appl. Phys.*, 69:668, 1991.
- [64] B.I. Kim. Direct comparison between phase locked oscillator and direct resonance oscillator in the noncontact atomic force microscopy under ultrahigh vacuum. *Rev. Sci. Instr.*, 75(11):5035–5037, 2004.
- [65] Ch. Loppacher, M. Bammerlin, F.M. Battiston, M. Guggisberg, D. Müller, H.R. Hidber, R. Lüthi, E. Meyer, and H.-J. Güntherodt. Fast Digital Electronics for Application in Dynamic Force Microscopy Using High-Q Cantilevers. *Appl. Phys. A*, 66:215, 1998.
- [66] S. Sadewasser and M. Ch. Lux-Steiner. Correct height measurement in noncontact atomic force microscopy. *Phys. Rev. Lett.*, 91(26):266101, 2003.

- [67] J.N. Israelachvili. *Intermolecular and Surface Forces*. Academic Press, London, 1985.
- [68] N. Sasaki and M. Tsukada. Effect of microscopic nonconservative process on noncontact atomic force microscopy. *Jap. J. Appl. Phys.*, 39:L1334, 2000.
- [69] U. Dürig. Conservative and dissipative interactions in dynamic force microscopy. *Surf. Interface Anal.*, 27(5-6): 467, 1999.
- [70] R. Boisgard, J.P. Aimé, and G. Couturier. Surface mechanical instabilities and dissipation under the action of an oscillating tip. *Surface Science*, 511:171–182, 2002.
- [71] R. Boisgard, J.P. Aimé, and G. Couturier. Analysis of mechanisms inducing damping in dynamic force microscopy: Surface viscoelastic behavior and stochastic resonance process. *Appl. Surf. Sci.*, 188:363–371, 2002.
- [72] W. Denk and D. Pohl. Local electrical dissipation imaged by scanning force microscopy. *Appl. Phys. Lett.*, 59(17): 2171–2173, 1991.
- [73] M. Gauthier and M. Tsukada. Damping mechanism in dynamic force microscopy. *Phys. Rev. Lett.*, 85(25):5348, 2000.
- [74] M. Gauthier and M. Tsukada. Theory of noncontact dissipation force microscopy. *Phys. Rev. B*, 60(16):11716, 1999.
- [75] L.N. Kantorovich. A simple non-equilibrium theory of non-contact dissipation force microscopy. *J. Phys.: Condens. Matter*, 13(5):945, 2001.
- [76] Ch. Loppacher, R. Bennewitz, O. Pfeiffer, M. Guggisberg, M. Bammerlin, S. Schär, V. Barwich, A. Baratoff, and E. Meyer. Experimental Aspects of Dissipation Force Microscopy. *Phys. Rev. B*, 62:13674, 2000.
- [77] R. Bennewitz, A.S. Foster, L.N. Kantorovich, M. Bammerlin, Ch. Loppacher, S. Schär, M. Guggisberg, E. Meyer, H.-J. Güntherodt, and A.L. Shluger. Atomically Resolved Steps and Kinks on NaCl islands on Cu(111): Experiment and Theory. *Phys. Rev. B*, 62:2074, 2000.
- [78] S.P. Jarvis, H. Yamada, K. Kobayashi, A. Toda, and H. Tokumoto. Normal and lateral force investigation using magnetically activated force sensors. *Appl. Surf. Sci.*, 157:314, 2000.
- [79] B. Such, J. Kolodziej, P. Czuba, P. Piatkowski, P. Struski, F. Krok, and M. Szymonski. Surface Topography Dependent Desorption of Alkali Halides. *Phys. Rev. Lett.*, 85:2621, 2000.
- [80] J.J. Kolodziej, B. Such, P. Czuba, F. Krok, P. Piatkowski, P. Struski, M. Szymonski, R. Bennewitz, S. Schär, and E. Meyer. Frenkel defect interactions at surfaces of irradiated alkali halides studied by non-contact atomic force microscopy. *Surface Science*, 482-485:902–909, 2001.
- [81] R. Bennewitz, S. Schär, V. Barwich, O. Pfeiffer, E. Meyer, F. Krok, B. Such, J. Kolodziej, and M. Szymonski. Atomic resolution images of radiation damage in KBr. *Surface Science*, 474:L197, 2001.
- [82] L. Nony, R. Bennewitz, O. Pfeiffer, E. Gneco, A. Baratoff, E. Meyer, T. Eguchi, A. Gourdon, and C. Joachim. Cu-TBPP and PTCDA molecules on insulating surfaces studied by ultra-high-vacuum non-contact AFM. *Nanotechnology*, 15:91–96, 2004.

- [83] L. Nony, E. Gnecco, A. Baratoff, A. Alkauskas, R. Bennewitz, O. Pfeiffer, S. Maier, A. Wetzler, E. Meyer, and Ch. Gerber. Observation of individual molecules trapped on a nanostructured insulator. *Nano Letters*, 11:2185–2189, 2004.
- [84] L. Howald, E. Meyer, R. Lüthi, H. Haefke, R. Overney, H. Rudin, and H.-J. Güntherodt. Multifunctional force microscope for facile operation in ultrahigh vacuum. *Appl. Phys. Lett.*, 63:117, 1993.
- [85] E.R.I. Abraham and E.A. Cornell. Teflon feedthrough for coupling optical fibers into ultrahigh vacuum systems. *Applied Optics*, 37(10):1762–1763, 1998.
- [86] S. Kitamura and M. Iwatsuki. High-resolution imaging of contact potential difference with ultrahigh vacuum non-contact atomic force microscope. *Appl. Phys. Lett.*, 72(24):3154–3156, 1998.
- [87] A. Kikukawa, S. Hosaka, and R. Imura. Silicon pn junction imaging and characterizations using sensitivity enhanced kelvin probe force microscopy. *Appl. Phys. Lett.*, 66(25):3510–3512, 1995.
- [88] Ch. Sommerhalter, Th. Matthes, Th. Glatzel, A. Jäger-Waldau, and M. Ch. Lux-Steiner. High-sensitivity quantitative kelvin probe microscopy by non-contact ultrahigh vacuum atomic force microscopy. *Appl. Phys. Lett.*, 75:286, 1999.
- [89] Christian Loppacher. *Nichtkontakt-Rasterkraftmikroskopie mit digitalem Phasenregelkreis*. PhD Thesis, Universität Basel, 2000.
- [90] E. Meyer, R.M. Overney, K. Dransfeld, and T. Gyalog. *Nanoscience: Friction and Rheology on the nanometer scale*. World Scientific, Singapore, 1998.
- [91] J.P. Cleveland, S. Manne, D. Bocek, and P.K. Hansma. A nondestructive method for determining the spring constant of cantilevers for scanning force microscopy. *Rev. Sci. Instr.*, 64(2):403–405, 1993.
- [92] J.E. Sader. Calibration of rectangular atomic force microscope cantilevers. *Rev. Sci. Instr.*, 70:3967, 1999.
- [93] D.F. Ogletree, R.W. Carpick, and M. Salmeron. Calibration of frictional forces in atomic force microscopy. *Rev. Sci. Instr.*, 67(9):3298, 1996.
- [94] M. Varenberg, I. Etsion, and G. Halperin. An improved wedge calibration method for lateral force in atomic force microscopy. *Rev. Sci. Instr.*, 74(7):3362–3367, 2003.
- [95] E. Meyer, H.J. Hug, and R. Bennewitz. *Scanning Probe Microscopy: The Lab on a Tip*. Springer-Verlag, Berlin, 2004.
- [96] D. Sarid. *Scanning Force Microscopy*. Oxford University Press, 1991.
- [97] W.C.Young and R.G. Budynas. *Roark's formulas of stress and strain*. McGraw-Hill, 7th edition, 2002.
- [98] Martin Guggisberg. *Lokale Messung von atomaren Kräften*. PhD Thesis, Universität Basel, 2000.
- [99] F.J. Giessibl. Forces and frequency shifts in atomic-resolution dynamic-force microscopy. *Phys. Rev. B*, 56(24):16010–16015, 1997.
- [100] F.J. Giessibl and H. Bielefeldt. Physical interpretation of frequency-modulation atomic force microscopy. *Phys. Rev. B*, 61(15):9968, 2000.

- [101] S. Rast, Ch. Waddinger, U. Gysin, and E. Meyer. The noise of cantilevers. *Nanotechnology*, 11:169–172, 2000.
- [102] O. Pfeiffer, C. Loppacher, C. Waddinger, M. Bammerlin, U. Gysin, M. Guggisberg, R. Bennewitz, E. Meyer, and H.-J. Güntherodt. Using higher flexural modes in non-contact force microscopy. *Appl. Surf. Sci.*, 157:337, 2000.
- [103] NANOSENSORS.
<http://www.nanosensors.com>.
- [104] F.J. Giessibl. Advances in atomic force microscopy. *Rev. Mod. Phys.*, 75(3):949–983, 2003.
- [105] T. Eguchi and Y. Hasegawa. High resolution atomic force microscopic imaging of the Si(111)-(7x7) surface: Contribution of short-range force to the images. *Phys. Rev. Lett.*, 89(26):266105, 2002.
- [106] M. Tomitori and T. Arai. Tip cleaning and sharpening processes for non-contact atomic force microscope in ultrahigh vacuum. *Appl. Surf. Sci.*, 140:432–438, 1999.
- [107] H. Lüth. *Solid surfaces, Interfaces and Thin Films*. Springer-Verlag, Berlin, Heidelberg, NY, Barcelona, Hong Kong, London, Milan, Paris, Tokyo, 2001.
- [108] C. Barth, Ch. Claeys, and C.R. Henry. Surface preparation of hard ionic crystals by ultrahigh vacuum cleavage. *Rev. Sci. Instr.*, 76:83907, 2005.
- [109] K. Yamamoto, T. Iijima, T. Kunishi, K. Fuwa, and T. Osaka. The growth forms of small Au particles grown on KBr and NaCl substrates having monatomic steps. *Journal of Crystal Growth*, 94(3):629, 1989.
- [110] R. Bennewitz. Structured surfaces of wide band gap insulators as templates for overgrowth of adsorbates. *J. Phys. Condens. Matt.*, 18:R417–, 2006.
- [111] L. Pham Van, J. Cousty, and Ch. Lubin. Step heights and terrace terminations of a vicinal (0001) α -alumina surface annealed in UHV. *Surface Science*, 549:157–164, 2004.
- [112] C. Barth and M. Reichling. Imaging the atomic arrangements on the high temperature reconstructed α -Al₂O₃-surface. *Nature*, 414:54, 2001.
- [113] J. Toofan and P.R. Watson. The termination of the α -Al₂O₃(0001) surface: A leed crystallography determination. *Surface Science*, 401:162–172, 1998.
- [114] G. Renaud, B. Villette, I. Vilfan, and A. Bourret. Atomic structure of the α -Al₂O₃(0001)($\sqrt{31} \times \sqrt{31}$)R $\pm 9^\circ$ reconstruction. *Phys. Rev. Lett.*, 73(13):1825–1828, 1994.
- [115] J. Wang, A. Howard, R.G. Egdell, J.B. Pethica, and J.S. Foord. Arrangement of rotational domains of the ($\sqrt{31} \times \sqrt{31}$)R $\pm 9^\circ$ reconstruction of Al₂O₃ revealed by non-contact afm. *Surface Science*, 515:337–343, 2002.
- [116] S.L. Tait, L.T. Ngo, Qiuming Yu, S.C. Fain, and C.T. Campbell. Growth and sintering of Pd clusters on α -Al₂O₃(0001). *Journal of Chemical Physics*, 122(6):64712 – 1, 2005.
- [117] T.M. French and G.A. Somorjai. Composition and surface structure of the (0001) face of the α -alumina by low-energy electron diffraction. *J. Phys. Chem.*, 74(12):2489–2495, 1970.
- [118] J.L. Hutter and J. Bechhoefer. Calibration of atomic force microscope tips. *Rev. Sci. Instr.*, 64(7):1868–1878, 1993.

- [119] J.P. Cleveland, T.E. Schäffer, and P.K. Hansma. Probing oscillatory hydration potentials using thermal-mechanical noise in an atomic force microscope. *Phys. Rev. B*, 52:R8692, 1995.
- [120] D.O. Koralek, W.F. Heinz, M.D. Antonik, A. Baik, and J.H. Hoh. Probing deep interaction potentials with white-noise-driven atomic force microscope cantilevers. *Appl. Phys. Lett.*, 76(20):2952, 2000.
- [121] W.F. Heinz, M.D. Antonik, and J.H. Hoh. Reconstructing local interaction potentials from perturbations to the thermally driven motion of an atomic force microscope cantilever. *J. Phys. Chem. B*, 104:622–626, 2000.
- [122] A. Roters and D. Johannsmann. Distance-dependent noise measurements in scanning force microscopy. *J. Phys. Condens. Matt.*, 8:7561–7577, 1996.
- [123] T. Drobek, R.W. Stark, and W.M. Heckl. Determination of shear stiffness based on thermal noise analysis in atomic force microscopy: Passive overtone microscopy. *Phys. Rev. B*, 64:045401, 2001.
- [124] H.J. Butt and M. Jaschke. Calculation of thermal noise in atomic force microscopy. *Nanotechnology*, 6(1):1, 1995.
- [125] T.E. Schäffer. Calculation of thermal noise in an atomic force microscope with a finite optical spot size. *Nanotechnology*, 16:664–670, 2005.
- [126] S. Maier. Thermisches Rauschen von AFM Cantilevern. Semesterarbeit, University of Basel, 2002.
- [127] U. Rabe, K. Janser, and W. Arnold. Vibrations of free and surface-coupled atomic force microscope cantilevers: Theory and experiment. *Rev. Sci. Instr.*, 67(9):3281, 1996.
- [128] E. Dupas. *Cartographie et spectroscopie des propriétés mécaniques à l'échelle du nanomètre par spectrométrie acoustique locale à fréquence variable*. PhD thesis, École polytechnique fédérale de Lausanne, 2000.
- [129] M.A. Lantz, S.J. O'Shea, A.C.F. Hoole, and M.E. Welland. Lateral stiffness of the tip and tip-sample contact in frictional force microscopy. *Appl. Phys. Lett.*, 70:970, 1997.
- [130] R.W. Carpick, D.F. Ogletree, and M. Salmeron. Lateral stiffness: A new nanomechanical measurement for the determination of shear strengths with friction force microscopy. *Appl. Phys. Lett.*, 70:1548, 1997.
- [131] M. Reinstädler, U. Rabe, A. Goldade, B. Bushan, and W. Arnold. Investigating ultra-thin lubricant layers using resonant friction force microscopy. *Tribology International*, 38:533–541, 2005.
- [132] M. Reinstädler, T. Kasai, U. Rabe, A. Goldade, B. Bushan, and W. Arnold. Imaging and measurement of elasticity and friction using the TR-mode. *J. Phys. D: Appl. Phys.*, 38:R269–R282, 2005.
- [133] V. Scherer, W. Arnold, and B. Bushan. Lateral force microscopy using acoustic friction force microscopy. *Surf. Interface Anal.*, 27:578–587, 1999.
- [134] P. Markiewicz and M.C. Goh. Atomic force microscope tip deconvolution using calibration arrays. *Rev. Sci. Instr.*, 66(5):3186–3190, 1995.
- [135] F.J. Giessibl, S. Hembacher, H. Bielefeldt, and J. Mannhart. Subatomic features on the silicon (111)-(7×7) surface

- observed by atomic force microscopy. *Science*, 289:422, 2000.
- [136] S. Hembacher and J. Mannhart F.J. Giessibl. Force microscopy with light-atom probes. *Science*, 305(5682): 380–383, 2004.
- [137] U. Wyder. Simulation der Wechselwirkung zwischen Spitze und Probe im Atomic Force Microscope (AFM) mittels SCIFI. Diploma Thesis, University of Basel, 2004.
- [138] U. Wyder et. al. Interpretation of atomic friction experiments using atomistic simulations. In preparation.
- [139] T. Kawagishi, A. Kato, Y. Hoshi, and H. Kawakatsu. Mapping of lateral vibration of the tip in atomic force microscopy at the torsional resonance of the cantilever. *Ultramicroscopy*, 91:37, 2002.
- [140] A. Garg. Escape-field distribution for escape from a metastable potential well subject to a steadily increasing bias field. *Phys. Rev. B*, 51(21):15592, 1995.
- [141] M.P. Allen and D.J. Tildesley. *Computer Simulations of Liquids*. Clarendon, Oxford, 1990.
- [142] S. Yu. Krylov, J.A. Dijksman, W.A. van Loo, and J.W.M. Frenken. Stick-slip motion in spite of slippery contact: Do we get what we see in atomic friction? *Phys. Rev. Lett.*, 97:166103, 2006.
- [143] A.I. Livshits and A.L. Shluger. Self-lubrication in scanning-force-microscope image formation on ionic surfaces. *Phys. Rev. B*, 56:12482, 1997.
- [144] O.K. Dudko, A.E. Filippov, J. Klafter, and M. Urbakh. Beyond the conventional description of dynamic force spectroscopy of adhesion bonds. *PNAS*, 100(20):11378–11381, 2003.
- [145] H. Hölscher, U.D. Schwarz, and R. Wiesendanger. Simulation of a scanned tip on a NaF(001) surface in friction force microscopy. *Europhys. Lett.*, 36(1):19–24, 1996.
- [146] M. Evstigneev, A. Schirmeisen, L. Jansen, H. Fuchs, and P. Reimann. Force dependence of transition rates in atomic friction. *Accepted in Phys. Rev. Lett.*, 2006.
- [147] W.H. Press, S.A. Teukolsky, W.T. Vetterling, and B.P. Flannery. *Numerical Recipes in C: The art of scientific computing*. Cambridge University Press, 1992.
- [148] M. Urbakh, J. Klafter, D. Gourdon, and J. Israelachvili. The nonlinear nature of friction. *Nature*, 430:525, 2004.
- [149] S. Aubry. The twist map, the extended Frenkel-Kontorova model and the devil’s staircase. *Physica*, 7D:240–258, 1983.
- [150] A. Socoliuc. *Control of friction on the atomic scale*. PhD thesis, University of Basel, 2005.
- [151] D. Godfrey. Vibration reduces metal to metal contact and causes an apparent reduction in friction. *ASLE TRANS.*, 10(2):183–192, 1967.
- [152] F. Dinelli, S.K. Biswas, G.A.D. Briggs, and O.V. Kolosov. Ultrasound induced lubricity in microscopic contacts. *Appl. Phys. Lett.*, 71(9):1177–1179, 1997.
- [153] M. Heuberger, C. Drummond, and J. Israelachvili. Coupling of normal and transverse motions during frictional sliding. *J. Phys. Chem. B*, 102:5038–5041, 1998.

- [154] O. Zwörner, H. Hölscher, U.D.Schwarz, and R. Wiesendanger. The velocity dependence of frictional forces in point-contact friction. *Appl. Phys. A*, 66:263, 1998.
- [155] H. Brune. *Single molecules at surfaces*, chapter Supperlattices of Atoms, Molecules, and Islands. Springer, New York, 2006.
- [156] L. G. Schultz. Growth of alkali halides from the vapor on single-crystal substrates of alkali halides. *Acta Cryst.*, 5: 130–132, 1952.
- [157] M. H. Yang and C.P. Flynn. Growth of alkali halides from molecular beams: Global growth characteristics. *Phys. Rev. Lett.*, 62(21):2476–2479, 1989.
- [158] M. H. Yang and C.P. Flynn. Growth of alkali halides by molecular-beam epitaxy. *Phys. Rev. B*, 41(12):8500–8508, 1990.
- [159] K. Saiki. Fabrication and characterization of epitaxial films of ionic materials. *Appl. Surf. Sci.*, 133/114:9–17, 1997.
- [160] K. Gloeckler, M. Sokolowski, A. Soukopp, and E. Umbach. Initial growth of insulating overlayers of NaCl on Ge(100) observed by scanning tunneling microscopy with atomic resolution. *Phys. Rev. B*, 54:7705, 1996.
- [161] W. Hebenstreit, J. Redinger, Z. Horozova, M. Schmid, R. Podloucky, and P. Varga. Atomic resolution by STM on ultra-thin films of alkali halides: experiment and local density calculations. *Surface Science*, 424:L321, 1999.
- [162] R. Bennewitz, M. Bammerlin, M. Guggisberg, C. Loppacher, A. Baratoff, E. Meyer, and H.-J. Güntherodt. Aspects of Dynamic Force Microscopy on NaCl/Cu(111): Resolution, Tip-Sample Interactions and Cantilever Oscillation Characteristics. *Surf. Interface Anal.*, 27:462, 1999.
- [163] J. Repp, G. Meyer, and K.-H. Rieder. Snells law for surface electrons: Refraction of an electron gas imaged in real space. *Phys. Rev. Lett.*, 92(3):036803, 2004.
- [164] J. Repp, S. Fölsch, G. Meyer, and K.-H. Rieder. Ionic films on vicinal metal surfaces: enhanced binding due to charge modulation. *Phys. Rev. Lett.*, 86(2):252, 2001.
- [165] S. Fölsch, A. Riemann, J. Repp, G. Meyer, and K.-H. Rieder. From atomic kinks to mesoscopic surface patterns: Ionic layers on vicinal metal surfaces. *Phys. Rev. B*, 66(16):161409, 2002.
- [166] J.J. Kolodziej, B. Such, P. Czuba, F. Krok, P. Piatkowski, and M. Szymon-ski. Scanning-tunneling/atomic-force microscopy study of the growth of KBr films on InSb(001). *Surface Science*, 506 (1-2):12, 2002.
- [167] P. Mazur and F. Golek. Morphology of LiBr/LiF system studied by C-AFM. *Phys. Stat. Sol. A*, 202(14):R155–R157, 2005.
- [168] M. Henzler, C. Homann, U. Malaske, and J. Wollschläger. Misfit accommodation in heteroepitaxy by inclining stacking faults. *Phys. Rev. B*, 52(24):R17060–R17062, 1994.
- [169] J. Baker and P.A. Lindgard. Monte Carlo determination of heteroepitaxial misfit structures. *Phys. Rev. B*, 54(16): R11137, 1996.
- [170] J. Baker and P.A. Lindgard. Heteroepitaxial strain in alkali halide thin films:

- KCl on NaCl. *Phys. Rev. B*, 60(24):16941–16949, 1999.
- [171] A. Natori, A. Tanaka, and H. Yasunaga. Heteroepitaxy of KCl on KBr substrate. *Thin Solid Films*, 281-282:39–42, 1996.
- [172] A. Natori, K. Toda, A. Tanaka, and H. Yasunaga. Interface atomic structures in alkali halides heteroepitaxy. *Appl. Surf. Sci.*, 130-132:616–622, 1998.
- [173] M. Kiguchi, K. Saiki, and A. Koma. Effects of anharmonicity of ionic bonds on the lattice distortion at the interface of alkali halide heterostructures. *Surface Science*, 470:81–88, 2000.
- [174] J. Duan, G.G. Bishop, E.S. Gillman, G. Chern, S.A. Safron, and J.G. Skofronick. Epitaxial growth of KBr onto NaCl(001) by high-resolution He atom scattering. *Surface Science*, 272(1-3):220 – 228, 1992.
- [175] V. Celli and G. Urzua. Interionic potentials and epitaxy on NaCl(001) and KBr(001). *J. Phys.: Condens. Matter*, 5:B91–B98, 1993.
- [176] R. Bennewitz, S. Schaer, E. Gnecco, O. Pfeiffer, M. Bammerlin, and E. Meyer. Atomic structure of alkali halide surfaces. *Appl. Phys. A*, 78:837, 2004.
- [177] J. Repp, G. Meyer, F.E. Olsson, and M. Persson. Controlling the charge state of individual gold adatoms. *Science*, 305(5683):493 – 5, 2004.
- [178] M. Pivetta, F. Patthey, M. Stengel, A. Baldereschi, and W.-D. Schneider. Local work function Moiré pattern on ultrathin ionic films: NaCl on Ag(100). *Phys. Rev. B*, 72:115404, 2005.
- [179] U. Hessinger, M. Leskovar, and M.A. Olmstead. Role of step and terrace nucleation in heteroepitaxial growth morphology: Growth kinetics of CaF₂/Si(111). *Phys. Rev. Lett.*, 75(12):2380–2383, 1995.
- [180] Z. Rong and P. Kuiper. Electronic effects in scanning tunneling microscopy: Moiré pattern on a graphite surface. *Phys. Rev. B*, 48(23):17427–17431, 1993.
- [181] K. Kobayashi. Moiré pattern in scanning tunneling microscopy: Mechanism in observation of subsurface nanostructures. *Phys. Rev. B*, 53(16):11091–11099, 1996.
- [182] A.L. Shluger, A.L. Rohl, and D.H. Gay. Properties of small clusters at ionic surfaces: NaCl_n clusters ($n = 148$) at the (100) MgO surface. *Phys. Rev. B*, 51(19):13631–13644, 1995.
- [183] J. Duan, G.G. Bishop, E.S. Gillman, G. Chern, S.A. Safron, and J.G. Skofronick. Homoepitaxial growth investigated by high-resolution He atom scattering: NaCl onto NaCl(001). *J. Vac. Sci. Technol. A*, 10(4):1999 – 2005, 1992.
- [184] R. Bennewitz, O. Pfeiffer, S. Schär, V. Barwich, and E. Meyer. Atomic corrugation in nc-AFM of alkali halides. *Appl. Surf. Sci.*, 188:232, 2002.
- [185] G. Chern, J.G. Skofronick, W.P. Brug, and S.A. Safron. Surface-phonon dispersion curves of KBr(001) via helium-atom scattering: Comparison with calculations. *Phys. Rev. B*, 39(17):12828–12837, 1989.
- [186] F. Goleck, P. Mazur, Z. Ryska, and S. Zuber. Morphology of alkali halide thin films studied by AFM. *Surface Science*, 600:1689–1696, 2006.
- [187] S. Maier, Y. Sang, T. Filleter, M. Grant, R. Bennewitz, E. Gnecco, and E. Meyer. Fluctuations and jump dynamics in

- atomic friction experiments. *Phys. Rev. B*, 72:245418, 2005.
- [188] A. Schirmeisen, D. Weiner, and H. Fuchs. Single-atom contact mechanics: From atomic scale energy barrier to mechanical relaxation hysteresis. *Phys. Rev. Lett.*, 97:136101, 2006.
- [189] S.A. Burke, J.M. Mativetsky, R. Hoffmann, and P. Grütter. Nucleation and submonolayer growth of C₆₀ on KBr. *Phys. Rev. Lett.*, 94(9):096102 – 1, 2005.
- [190] H. Brune. Microscopic view of epitaxial metal growth: Nucleation and aggregation. *Surf. Sci. Rep.*, 31:121–229, 1998.
- [191] H.Y. Lin, Y. P. Chiu, L.W. Huang, Y.W. Chen, T.Y. Fu, C. S. Chang, and T.T. Tsong. Self-organized growth of nanopucks on Pb quantum islands. *Phys. Rev. Lett.*, 94:136101, 2005.

List of Publications

Papers

1. A. Socoliuc, E. Gnecco, **S. Maier**, O. Pfeiffer, A. Baratoff, R. Bennewitz, E. Meyer.
Atomic-scale control of friction by actuation of nanometer-sized contacts.
Science 313 (2006) 207-210.
2. T. Filleter, **S. Maier**, R. Bennewitz.
Atomic-scale yield and dislocation nucleation in KBr.
Phys. Rev. B 73 (2006) 155433.
3. **S. Maier**, Yi Sang, T. Filleter, M. Grant, R. Bennewitz, E. Gnecco, E. Meyer.
Fluctuations and jump dynamics in atomic friction experiments.
Phys. Rev. B 72 (2005) 245418.
4. O. Pfeiffer, E. Gnecco, L. Zimmerli, **S. Maier**, E. Meyer, L. Nony, R. Bennewitz, F. Diederich, H. Fang, D. Bonifazi.
Force microscopy on insulators: Imaging of organic molecules.
Journal of Physics: Conference Series 19 (2005) 166-174.
5. L. Nony, E. Gnecco, A. Baratoff, A. Alkauskas, R. Bennewitz, O. Pfeiffer, **S. Maier**, A. Wetzel, E. Meyer, Ch. Gerber.
Observation of Individual Molecules Trapped on a Nanostructured Insulator.
Nano Letters, Vol. 4, No. 11 (2004) 2185-2189.
6. L. Zimmerli, **S. Maier**, Th. Glatzel, E. Gnecco, O. Pfeiffer, F. Diederich, L. Fendt, E. Meyer.
Formation of molecular wires on nanostructured KBr.
Accepted in Journal of Physics: Conference Series.
7. **S. Maier**, O. Pfeiffer, Th. Glatzel, E. Meyer, T. Filleter, R. Bennewitz.
Asymmetry in the reciprocal epitaxy of NaCl and KBr.
Submitted to Phys. Rev. B.
8. **S. Maier**, E. Gnecco, A. Baratoff, R. Bennewitz, E. Meyer.
Atomic-scale friction on crystal superlattices.
In preparation.
9. U. Wyder, A. Baratoff, E. Meyer, L.N. Kantorovich, J. David, **S. Maier**, T. Filleter, R. Bennewitz.
Interpretation of atomic friction experiments based on atomistic simulations.
In preparation.

Talks

1. S. Maier, R. Bennewitz, T. Filleter, Th. Glatzel, E. Gnecco, E. Meyer
Heteroepitaxial Growth of NaCl/KBr and KBr/NaCl Investigated by NC-AFM.
International Conference on Nanoscience and Technology.
30.7.-4.8.2006. Basel, Switzerland.
2. S. Maier, R. Bennewitz, T. Filleter, Th. Glatzel, E. Gnecco, E. Meyer
Heteroepitaxial growth of NaCl and KBr.
9th International Conference on Non-contact Atomic Force Microscopy.
16.-20.7.2006. Kobe, Japan.
3. S. Maier, Y. Sang, T. Filleter, M. Grant, R. Bennewitz, E. Gnecco, E. Meyer.
Thermal fluctuations and jump dynamics in atomic friction.
FRONTIERS Workshop "Understanding processes at the molecular level".
19.-23.3.2006. Lenzerheide, Switzerland.
4. S. Maier, T. Filleter, R. Bennewitz, E. Meyer.
Time-resolved measurements of atomic stick-slip in friction.
4th ESF Nanotribology Workshop.
18.-22.6.2005. Porquerolles, France.
5. S. Maier, L. Nony, E. Gnecco, R. Bennewitz, O. Pfeiffer, A. Wetzels, E. Meyer.
Ordered molecular assemblies confined on a nano-structured insulator investigated by UHV-AFM.
SPS Annual Meeting.
3./4.3.2004. Neuchatel, Switzerland.

Posters

1. S. Maier, E. Gnecco, A. Baratoff, Th. Glatzel, R. Bennewitz, E. Meyer.
Atomic friction study of heteroepitaxial thin films on alkali halides.
5th ESF Nanotribology Workshop, 23.-27.9.2006, Antalya, Turkey.
2. S. Maier, Y. Sang, T. Filleter, M. Grant, R. Bennewitz, E. Gnecco, E. Meyer.
Fluctuations and jump dynamics in atomic friction.
DPG Meeting, 27.-31.3.2006, Dresden, Germany.
3. S. Maier, T. Filleter, R. Bennewitz, E. Meyer.
Time-resolved measurements of atomic stick-slip in friction.
Nano Forum Canada 15.-17.6.2005, Montreal, Canada.
4. S. Maier, T. Filleter, R. Bennewitz, E. Meyer.
Time-resolved measurements of atomic stick-slip in friction.
RQMP Poster Meeting, 16.5.2005, Montreal, Canada.
5. S. Maier, R. Bennewitz, E. Gnecco, L. Nony, A. Socoliuc, O. Pfeiffer, A. Wetzels, E. Meyer.
High-bandwidth analysis of force signals in ultra-high vacuum atomic force microscopy.
APS March Meeting, 22.-26.3.2004, Montreal, Canada.

Curriculum Vitae

Name: Sabine Maier
Date of Birth: 18th May 1979
Place of Birth: Basel, Switzerland

-
- 2003-2007 PhD student and teaching assistant in the research group of Prof. E. Meyer
University of Basel, Switzerland
- 2004-2005 Visiting scientist in the research group of Prof. R. Bennowitz,
McGill University, Montreal, Canada
- June 2003 Master of Science, University of Basel
Master thesis: Nitridation of aluminium oxide
Thesis supervisor: Prof. E. Meyer
- 1998-2003 Study of physics at the University of Basel, Switzerland
(major: physics, minor: mathematics, elective: computer science)
- June 1998 Matura type B (Latin, French, English and Science)
Gymnasium Bäumlhof in Basel, Switzerland
-

List of Professors and Lecturers during my studies at the University of Basel

Prof. E. Meyer, Prof. R. Bennowitz, Prof. Ch. Schönenberger, Prof. I. Sick, Prof. L. Tauscher, Prof. D. Loss, Prof. Ch. Bruder, Prof. D. Trautmann, Prof. F. Thielemann, Prof. G.R. Plattner, Dr. J. Jourdan, Dr. H. Mühry, Prof. C. Bandle, Prof. D.W. Masser, Prof. H. Kraft, Prof. M. Grote, Dr. H. Walser, Prof. H. Burkhart, Dr. R. Zimak, Prof. G. Tammann, Prof. R. Buser.